Optimization Strategies for Respiratory Motion Management in Stereotactic Body Radiation Therapy

Philipp Freislederer

München 2020

Aus der
Strahlentherapie und Radioonkologie
Klinik der Ludwig–Maximilians–Universität München
Direktor: Prof. Dr. med. Claus Belka

Optimization Strategies for Respiratory Motion Management in Stereotactic Body Radiation Therapy

Philipp Freislederer

Dissertation
zum Erwerb des Doktorgrades der Naturwissenschaften
an der Medizinischen Fakultät der
Ludwig–Maximilians–Universität zu München

vorgelegt von

Philipp Freislederer

aus

Deggendorf

2020

Mit Genehmigung der Medizinischen Fakultät
der Universität München

Erstgutachter: **Prof. Dr. rer. nat. Katia Parodi**
Zweitgutachter: **Prof. Dr. rer. nat. Sibylle Ziegler**
Dekan: **Prof. Dr. med. dent. Reinhard Hickel**
Tag der mündlichen Prüfung: **07.10.2020**

Für Emmi Noemi

Affidavit

Eidesstattliche Versicherung

Ich, Philipp Freislederer, erkläre hiermit an Eides statt, dass ich die vorliegende Dissertation mit dem Titel

Optimization Strategies for Respiratory Motion Management in Stereotactic Body Radiation Therapy

selbstständig verfasst, mich außer der angegebenden keiner weiteren Hilfsmittlel bedient und alle Erkenntnisse, die aus dem Schrifttum ganz oder annähernd übernommen sind, als solche kenntlich gemacht und nach ihrer Herkunft unter Bezeichnung der Fundstelle einzeln nachgewiesen habe.

Ich erkläre des Weiteren, dass die hier vorgelegte Dissertation nicht in gleicher oder in ähnlicher Form bei einer anderen Stelle zur Erlangung eines akademischen Grades eingereicht wurde.

München, 15.10.2020   **Philipp Freislederer**

Table of content

Summary

Various challenges arise during the treatment of lung tumors with stereotactic body radiation therapy (SBRT), which is a form of hypofractionated high precision conformal radiation therapy delivered to small targets. The dose is applied in only a few fractions and respiratory organ and tumor motion is a source of uncertainty additional to interfractional set-up errors. Respiratory organ and tumor motion is highly patient-specific and it affects the whole radiotherapy treatment chain. In this thesis, motion management techniques for SBRT are evaluated and improved in a clinical setting. A clinical need for improvement has been present at the LMU university hospital for each issue addressed in this thesis: Initially, the usage of respiratory correlated computed tomography (4DCT), which is vital for SBRT treatment, was seen as impractical and prone to uncertainties in the data reconstruction in its current form. Therefore, the 4DCT reconstruction workflow has been improved to minimize these potential error sources. Secondly, treatment planning for tumors affected by respiratory motion was evaluated and subsequently improved. Finally, the treatment technique of respiratory gating was implemented at the clinic, which led to the need of evaluating the respiratory gating characteristics of the novel system configuration.

At first, the 4DCT reconstruction workflow used in clinical practice was investigated, as in the presence of respiratory motion the knowledge of tumor position over time is essential in SBRT treatments. Using 4DCT, the full motion range of the individual tumor can be determined. However, certain 4DCT reconstruction methods can under- or overestimate tumor motion due to limitations in the data acquisition scheme and due to the incorrect sorting of certain X-ray computed tomography (CT) image slices into different respiratory phases. As the regular clinical workflow of cycle-based sorting (CBS) without maximum inspiration detection (and therefore no clear starting point for the individual breathing cycles) seemed to be affected by these potential errors, the usage of CBS with correct maximum detection and another sorting algorithm of the respiration states, so-called local amplitude-based sorting (LAS), both have been implemented for a reduction of image artifacts and improved 4DCT quality. The three phase binning algorithms have been investigated in a phantom study (using 10 different breathing waveforms) and in a patient study (with 10 different patients). The mis-representation of the tumor volume was reduced in both implemented sorting algorithms compared to the previously used CBS approach (without correct maximum detection) in the phantom and the patient study. The

clinical recommendation was the use of CBS with improved maximum detection, as too many manual interventions would be needed for the LAS workflow.

Secondly, a combination of the actual patient breathing trace during treatment, the log files generated by the linear accelerator (LINAC), and Monte Carlo (MC) four-dimensional (4D) dose calculations for each individual fraction was implemented as a 4D dose evaluation tool. This workflow was tested in a clinical environment for SBRT treatment planning on multiple CT datasets featuring: a native free-breathing 3DCT, an average intensity projection (AIP) as well as a maximum intensity projection (MIP), both obtained from the patient's 4DCT, and density overrides (DOs) in a 3DCT. This study has been carried out for 5 SBRT patients for three-dimensional conformal radiation therapy (3D-CRT) and volumetric modulated arc therapy (VMAT) treatment plans. The dose has been recalculated on each 4DCT breathing phase according the the patient's breathing waveform and accumulated to the gross tumor volume (GTV) at the end-of-exhale (EOE) breathing phase using deformable image registration. Even though the least differences in planned and recalculated dose were found for AIP and MIP treatment planning, the results indicate a strong dependency on individual tumor motion due to the variability of breathing motion in general, and on tumor size. The combination of the patient's individual breathing trace during each SBRT fraction with 4D MC dose calculation based on the LINAC log file information leads to a good approximation of actual dose delivery.

Finally, in order to ensure precise and accurate treatment for respiratory gating techniques, the technical characteristics of the LINAC in combination with a breathing motion monitoring system as s surrogate for tumor motion have to be identified. The dose delivery accuracy and the latency of a surface imaging system in connection with a modern medical LINAC were investigated using a dynamic breathing motion phantom. The dosimetric evaluation has been carried out using a static 2D-diode array. The measurement of the dose difference between gated and ungated radiation delivery was found to be below 1% (for clinical relevant gating levels of about 30%). The beam-on latency, or time delay, determined using radiographic films was found to be up to $851\,\mathrm{ms} \pm 100\,\mathrm{ms}$. With these known parameters, an adjustment of the pre-selected gating level or the internal target volume (ITV) margins could be made.

With the highly patient-specific character of respiratory motion, lung SBRT faces many additional challenges besides the specific issues addressed in this thesis. However, the findings of this thesis have improved clinical workflows at the Department of Radiation Oncology of the LMU University hospital. In a future perspective, a workflow using evaluation of the actual 4D dose in combination with accurate 4DCT image acquisition and specialized treatment delivery (such as respiratory gating) has the potential for a safe further reduction of treatment margins and increased sparing of organs-at-risk (OARs) in SBRT without compromising tumor dose targeting accuracy.

Zusammenfassung

Die stereotaktische Radiotherapie (Englisch: stereotactic body radiation therapy (SBRT)) zur Behandlung von Tumoren in der Lunge ist eine hypofraktionierte Hochpräzisionsbestrahlungstechnik für kleine Läsionen. Die Herausforderungen dabei beschränken sich nicht nur auf die Applikation einer hohen Dosis in nur wenigen Fraktionen (was wenig Spielraum für Unsicherheiten zulässt), sondern beinhalten zusätzlich zu den normalen interfraktionellen Lagerungsunsicherheiten auch die Atembeweglichkeit der Organe und dementsprechend auch die Beweglichkeit der zu behandelnden Läsion. Die stark patienten-spezifische Atembeweglichkeit beeinflusst den gesamten Vorgang der Bestrahlungsplanung bis hin zur eigentlichen Behandlung. Diese Dissertation befasst sich mit der Evaluierung und Verbesserung von speziellen Techniken zur Kompensation der Atembeweglichkeit bei SBRT in einem klinischen Umfeld. In den klinischen Abläufen am Klinikum der Universität München waren zu Beginn der Arbeiten dieser Dissertation Verbesserungen nötig: Der damalige Einsatz des sogenannten 4DCTs (Englisch: respiratory correlated computed tomography), welches für die Behandlung mit SBRT dringend erforderlich ist, wurde als unpraktisch und anfällig für Fehler in der Datenrekonstruktion betrachtet. Zum zweiten musste die damalige Methodik der Bestrahlungsplanung bei atembeweglichen Tumoren evaluiert und verbessert werden. Außerdem sollte eine Atemtriggerungstechnik in der Klinik implementiert werden, weshalb das neuartige System auf seine Eigenschaften bezüglich getriggerter Bestrahlung hin untersucht werden musste.

Zuerst wurde das damalige 4DCT Rekonstruktionsschema untersucht, da die exakte Kenntnis des zeitlichen Verlaufs der Tumorposition vor der eigentlichen Behandlung bei stereotaktischen Bestrahlungskonzepten im Lungenbereich essentiell ist. Mit Hilfe des 4DCTs kann patienten-individuell die gesamte Tumorbeweglichkeit erfasst werden. Jedoch können einige 4DCT Rekonstruktionsalgorithmen die Tumorbeweglichkeit über- oder auch unterschätzen: Entweder durch Ungenauigkeiten in der Datenakquise oder durch falsche Zuordnung der CT Schichten zu den verschiedenen Atemphasen. Der bisherige klinische Arbeitsablauf, eine zyklusbasierte Sortierung der Atemkurve ohne zuverlässige Detektion der maximalen Inspiration (dem Startpunkt von jedem Zyklus) war von derartigen Fehlerquellen beeinflussbar. Deshalb wurde sowohl eine zyklusbasierte Sortierungsmethode mit akkurater Detektion der Maxima als auch die sogenannte lokal amplitudenbasierte Sortierung (LAS) zur Reduktion von Bildartefakten und Verbesserung der 4DCT Qualität implementiert. Sowohl in einer Phantomstudie mit 10 verschiedenen Atemkurven, als

auch in einer Patientenstudie (10 Patienten) sind die drei verschiedenen 4DCT Phasen-Zuordnungsalgorithmen verglichen worden. Beide neu implementierten Verfahren reduzierten den Fehler in der Rekonstruktion des Tumorvolumens im Vergleich zur bisherigen, zyklusbasierten Methode (ohne korrekte Detektion der Maxima) am Phantom sowie bei der Patientenstudie. Wegen der geringeren Praktikabilität des LAS Ansatzes auf Grund verschiedener manueller Eingriffe in klinische Systeme war die LAS Methode trotz verbesserter 4DCT Rekonstruktion nicht empfehlenswert. Jedoch wurde der zyklusbasierte Ansatz mit optimaler Detektion der Maxima der Atemkurve wegen seiner geringeren Fehlerabhängigkeit für den klinischen Einsatz empfohlen.

Im zweiten Teil der Arbeit war festzustellen, welcher CT Datensatz die genaueste Grundlage für die klinische Bestrahlungsplanung bei SBRT Behandlungen darstellt. Deshalb wurde ein 4D Dosisevaluierungs-Tool implementiert, welches die tatsächliche Atmung des Patienten während der Bestrahlung mit dem Log Datensatz des Linearbeschleuingers (LINAC) kombiniert, um 4D Monte Carlo Dosisberechnungen auszuführen. Die Grundlage hierbei ist die Dosisberechnung auf vier verschiedenen CT Datensätzen: einem nativen 3DCT Datensatz in freier Atmung, ein aus dem 4DCT erstelltem AIP (Englisch: average intensity projection, ein CT Datensatz mit der mittleren Elektronendichte aller 4DCT Phasen) und einem MIP Datensatz (Englisch: maximum intensity projection, ein CT Datensatz mit der maximalen Elektronendichte aller 4DCT Phasen), sowie Dichteüberschreibungen (DO) in einem 3DCT. Die 4D Dosis wurde auf den einzelnen 4DCT Atemphasen gemäß der Atemkurve der Patienten nachgerechnet und mittels deformierbarer Registrierung auf das GTV (Englisch: Gross Tumor Volume) in maximaler Expiration akkumuliert. Obwohl die geringsten Unterschiede zwischen geplanter und 4D-nachgerechneter Dosis bei AIP- und MIP-basierter Bestrahlungsplanung ermittelt wurden, weisen die Resultate auf eine starke Abhängigkeit mit der individuellen Tumorbeweglichkeit, der Variabilität der Atmungsbewegung im Allgemeinen und der Tumorgröße hin. Durch die erstmalige Kombination von patientenindividueller Atembeweglichkeit während jeder Fraktion einer SBRT Behandlung und 4D Monte Carlo Dosisberechnung auf Basis der Log Datensätze des LINACs lässt sich eine gute Approximation der tatsächlich applizierten Dosis gewährleisten.

Zuletzt mussten die technischen Charakteristika bei der Kombination eines LINACs mit einem Surrogat zur Messung der Atembeweglichkeit bekannt sein, um eine präzise und akkurate Behandlung mit Atemtriggerungstechniken (dem sogenannten "Gating") zu garantieren. Die Genauigkeit der Dosisapplikation und die Latenz eines Oberflächenscanners, welcher zur Triggerung eines LINACs benutzt wird wurden mit Hilfe eines dynamischen Atemphantoms untersucht. Messungen mit einem statischen 2D-Dioden Array ergaben einen Dosisunterschied zwischen getriggerter und ungetriggerter Bestrahlung von weniger als 1 % für klinisch relevante Gatingfenster von ca. 30 %. Bei der radiographischen Filmmessung der Latenz beim Einschaltvorgang des Systems wurden Zeitverzögerungen bis zu 851 ms ± 100 ms ermittelt. Sobald diese Parameter bekannt sind, könnte ein vorher definiertes Gatingfenster oder auch die Erweiterung des Sicherheitssaums des sog. Internal Target Volume (ITV) angepasst werden.

Die Herausforderungen bei Bestrahlung von Lungentumoren mit SBRT beschränken sich nicht ausschließlich auf die in dieser Arbeit behandelten Themen, besonders wegen des hoch patienten-spezifischen Charakters respiratorischer Tumorbewegungen. Nichtsdestotrotz konnten die Ergebnisse dieser Dissertation die klinischen Arbeitsabläufe bei der Behandlung von Läsionen in der Lunge mit den Mitteln der Strahlentherapie optimieren. Das Ziel bei weiteren Studien ist die Evaluierung der tatsächlichen 4D Dosis mit akkurater, verbesserter 4D Bildgebung und hoch spezialisierten Dosisapplikationsverfahren (wie z.B. Atemtriggerung), was ein Potential zur weiteren (sicheren) Reduktion des zu bestrahlenden Volumens bei einer gleichzeitig verbesserten Schonung von gesunden Risikoorganen bei SBRT Behandlungen zur Folge hat, ohne dass die Zielvolumensdosis verringert wird.

Acknowledgments

First of all, I would like to thank my thesis supervisor Prof. Katia Parodi for taking the time to correct the various versions of this thesis and all my manuscripts. Additionally, for giving this thesis a clear scope and advising me during last years.

Secondly, this thesis would not have been possible without the thorough and kind supervision of Dr. Matthias Söhn. Most certainly, it would have looked different without him and his scientific standards, tremendous analytical talent, vision, and overall guidance.

Obviously, this work could not have been accomplished without the employment at the Department of Radiation Oncology at the LMU University hospital, for which mainly Dr. Michael Reiner as the head physicist and Prof. Claus Belka as the head of the Department of Radiation Oncology are responsible for. Thank you for supporting the work in this thesis financially and for giving the thesis it's direction and scope.

I would like to thank current and former colleagues at the Department of Radiation Oncology, who guided me through the past years, many of which becoming close friends. Specifically I want to thank Dr. Helmut Weingandt, Dr. Christoph Losert, Christian Heinz, Dr. Katrin Straub, Sebastian Neppl, and Roel Shpani for their support and friendship and for keeping the extraordinary work atmosphere. Additionally, Winfried Hoischen, Tobi Winderl, Robert Kießling, and Toni Quantz (who also helped in building my phantoms) for their assistance and support and the remaining medical physics team, all physicians, therapists and other co-workers, especially Prof. Maximilian Niyazi and Dr. Stefanie Corradini.

Apart from work, my closest friends have always encouraged me in pursuing my goals and made sure that the "work-life-balance" was always kept in an appropriate proportion. Special thanks to Markus Glitzner, Wilhelm Wimmer and Moritz Eigel!

The continuous motivation from my parents Christiane and Rupert had a huge effect on my life and I want to thank them both for their love, support and generosity. Also, my brother Peter and my aunt Inge in addition to my family in-law Manuela, Jacques, Selma and Hellmuth, had a major impact throughout my life before and during this thesis and I am very sure, that I would not be at this point in life without any of them.

I cannot express, how grateful I am to my wife and the love of my life, Nastassja. You have made every day in the last 16 years a special one and your belief in me has always encouraged me to continue in times of struggle. And to you, my little daughter Emmi, whom I would like to dedicate this thesis: thank you being a such a wonderful part of my life and never stop being as crazy and happy as you are now!

List of Figures

List of Abbreviations

2D two-dimensional

3D three-dimensional

3D-CRT three-dimensional conformal radiation therapy

3DCT three-dimensional computed tomography

4D four-dimensional

4DCT respiratory correlated computed tomography

AIP average intensity projection

AP anterior-posterior

BED biologically effective dose

CBCT cone-beam computed tomography

CBS cycle-based sorting

CC collapsed cone

CLD central lung distance

CT X-ray computed tomography

CTV clinical target volume

DIBH deep-inspiration breath-hold

DMLC dynamic multileaf collimator

DNA desoxyribonucleic acid

DO density override

DRR digitally reconstructed radiograph

DVH dose-volume histogram

EBRT external beam radiotherapy

EOE end-of-exhale

EOI end-of-inhale

EPID electronic portal imaging device

FFF flattening filter free

FSB forced shallow breathing

GTV gross tumor volume

HU Houndsfield units

ICRU International Commission on Radiation Units and Measurement

IGRT image guided radiation therapy

IMRT intensity modulated radiation therapy

ITV internal target volume

KERMA kinetic energy released per unit mass

LAS local amplitude-based sorting

LINAC linear accelerator

LQ linear quadratic

MC Monte Carlo

MeV mega electron volt

MIP maximum intensity projection

MLC multi-leaf collimator

MRI magnetic resonance imaging

MV megavolt

NSCLC non-small cell lung cancer

OAR organ-at-risk

PB pencil beam

PET positron-emission tomography

PTV planning target volume

QA quality assurance

RF radio frequency

RL right-left

ROI region of interest

SBRT stereotactic body radiation therapy

SGRT surface-guided radiation therapy

SI superior-inferior

SPECT single-photon emission computed tomography

SRS stereotactic radiosurgery

TERMA total energy released per unit mass

TPS treatment planning system

VMAT volumetric modulated arc therapy

WBRT whole brain radiation therapy

Chapter 1

Own Contributions

1.1 Paper 1: Comparison of Different Image Binning Algorithms for 4DCT Reconstruction for Radiation Therapy

For this study, the first author (=author of this thesis) is responsible for the manuscript draft, the concept of the study, and literature revision. The first author (=author of this thesis) had the original idea of implementing the workflow, implemented two workflows by designing and programming the software (together with 2nd author C.Heinz). The first author (=author of this thesis) prepared, evaluated and interpreted all data together with 2nd author H. von Zimmermann. The first author (=author of this thesis) wrote the final manuscript.

1.2 Paper 2: Comparison of Planned Dose on Different CT Image Sets to Four-dimensional Monte Carlo Dose Recalculation Using the Patient's Actual Breathing Trace for Lung Stereotactic Body Radiation Therapy

For this study, the first author (=author of this thesis) had the original idea of the manuscript and was responsible for the manuscript draft, the concept of the study, and literature revision. The first author (=author of this thesis)implemented the full workflow, which in part has been prepared by 2nd author A. von Münchow. The first author (=author of this thesis) carried out all treatment planning, data preparation, 4D dose and plan calculation, data evaluation and statistical interpretation. The first author (=author of this thesis) wrote the final manuscript.

1.3   Paper 3: Characteristics of Gated Treatment Using an Optical Surface Imaging and Gating System on an Elekta Linac

For this study, the first author (=author of this thesis) had the original idea of the manuscript and was responsible for the manuscript draft, the concept of the study, and literature revision. The first author (=author of this thesis) had the idea of the phantom used for all dose and latency evaluations, prepared, performed, and evaluated all measurements. The first author (=author of this thesis) wrote the final manuscript.

Chapter 2

Introduction

With an estimated number of 18.1 million new cases worldwide and 9.6 million deaths in 2018 [11], cancer is among the leading causes of death in the 21st century. With rapidly growing incidence and mortality rates, the struggle against cancer is a worldwide challenge in modern medicine. As the most common cancer in men and the third most common in women, lung cancer remains the most frequent cancer worldwide with around 2.1 million new cases and around 1.8 million predicted deaths in 2018 [1, 11]. Four major histological types of lung cancer exist: small cell carcinoma and three types of non-small cell lung cancer (NSCLC) (adenocarcinoma, squamous cell carcinoma, and large cell carcinoma). The best overall survival rate for NSCLC patients is achieved by surgical lobectomy and systematic mediastinal lymph node dissection, but for about 20 % of all patients diagnosed with NSCLC surgery is not an option [23].

Best supportive care or conventionally fractionated radiotherapy were the remaining choices until the introduction of stereotactic body radiation therapy (SBRT). In general, radiation therapy uses high radiation doses to kill malignant tumor cells while trying to spare radiosensitive organs in the proximity of the tumor (so-called organs-at-risk (OARs)). SBRT can be considered as hypofractionated (meaning that the dose is delivered in less fractions than in conventional radiation therapy with a higher dose per fraction in order to achieve the same biological effect) high precision conformal radiation therapy to small targets [9]. For medically inoperable NSCLC (stage I) patients, SBRT has been reported to have local tumor control rates of 84-98 % [23].

In general, SBRT faces a multitude of problems and challenges in addition to the uncertainties and possible pitfalls of conventionally fractionated radiotherapy. One of the main challenges in SBRT is the presence of respiratory motion. Considerable uncertainties in SBRT treatments of thoracic and upper abdominal sites remain due to respiratory motion [69]. Lung tumors move intra- and interfractionally according to the highly patient-specific breathing motion. Increasing the treatment margins could account for these motions on the one hand, but would also increase the dose to normal, healthy tissue on the other [31]. These problems affect the whole radiation therapy treatment chain, from image ac-

quisition over the course of treatment planning up to radiation delivery itself. Several techniques are already applied for the management of respiratory motion in radiation therapy, in order to reduce the dose to critical OARs. These include motion encompassing methods, respiratory gated or breath-hold techniques, forced shallow breathing methods, or respiration-synchronized delivery ("tumor tracking").

The main goal of this thesis was to optimize the present workflows for SBRT at the Department of Radiation Oncology of the LMU University hospital. The clinical need for improvement led to the optimization of three different, clinically relevant tasks. Specifically, three key issues are addressed in this thesis:

1. **4DCT reconstruction:** Respiratory motion of anatomical structures deteriorates the image quality of X-ray computed tomography (CT) of thoracic and upper abdominal sites [22]. For SBRT treatment planning, the acquisition of 4DCT datasets reduces artifacts which can occur in regular 3DCT datasets due to respiratory motion and allows for an investigation of the full tumor breathing motion trace [18, 22, 30, 36, 39]. Yet, there are differences between the methods of 4DCT acquisition, with some being prone to artifacts and others influencing the depicted tumor volume. With the regular, clinically used workflow for 4DCT acquisition and reconstruction, the full tumor motion range could have been over- or underestimated. This would influence the whole treatment planning process from target delineation to valid dose calculation at the available treatment planning CT scanner (Toshiba Aquilion 16 Large Bore, Toshiba Medical Systems Corporation, Otawara, Japan). Therefore, the task was to establish and optimize different workflows using an optical surface scanner as a motion monitoring system. In addition, the influence of different image sorting algorithms for 4DCT image reconstruction is evaluated in a phantom and a patient study to devise recommendations for clinical use.

2. **4D treatment planning:** The dose applied to the patient is usually calculated based on 3DCT dataset. As tumors in thoracic and abdominal treatment sites move due to respiratory motion, dose differences between planned and actually delivered dose in the target region and additionally in the surrounding OAR structures are present in most clinical settings. In order to get a close approximation of the "ground truth" delivered dose to the moving tumor, the dose calculation has to be carried out time-resolved. The goal was to develop a workflow for 4D MC dose calculation with the actual patient breathing trace for 3D-CRT and VMAT treatment plans for each individual treatment fraction. In addition, the question on which CT dataset treatment planning has to be carried out, in order to minimize possible dose differences between planned and delivered dose, is evaluated and discussed.

3. **Respiratory Gating:** Advanced techniques, such as respiratory gating or breathing control, can increase the accuracy of dose delivery in anatomical sites affected by respiratory motion [69]. As gated treatment (in which the dose is only delivered during specific motion phases) has been introduced in radiation therapy, the dose

to surrounding OARs structures can potentially be reduced to a minimum while still guaranteeing optimal tumor coverage [34, 42]. A technique with such a high potential in dose sparing has to be carried out with maximal accuracy and precision. Therefore, the capability of modern medical LINACs for respiratory gating needs to be assessed prior to clinical implementation. A novel surface imaging system has been installed at the LMU university hospital in combination with a LINAC which has not been designed specifically for the use in gated radiotherapy. For this specific clinical setting, thorough validation tests regarding dosimetric accuracy and overall system latency were designed and carried out.

.

Chapter 3 gives an overview of the technological and physical background of photon radiation therapy, including high energy photon beam generation with modern medical LINACs and the interaction of X-ray photon with matter. Chapter 4 describes the treatment planning process from CT (and 4DCT) acquisition to target delineation, radiation therapy treatment techniques (including dose calculation algorithms), and special requirements for SBRT treatment delivery. Chapter 5 summarizes the uncertainties in lung radiation therapy and describes methods for uncertainty mitigation. The novel contributions of this thesis are thereafter discussed in chapters 6, 7, and 8: In chapter 6, different phase sorting algorithms for 4DCT reconstruction are compared and validated clinically, and a novel phase sorting algorithm is introduced. In chapter 7, a workflow for the combination of the actual patient breathing trace during each individual treatment fraction with the Linac's log file information for Monte Carlo 4D dose calculations has been established. This has been tested on multiple CT datasets for lung SBRT treatment planning. In chapter 8, the capabilities of a medical LINAC to perform gated treatments are characterized in terms of system latency and dosimetric accuracy. In chapter 9, the conclusions of this thesis and future perspectives are discussed.

Chapter 3

Technological and Physical Background of Photon Radiation Therapy

Radiation therapy uses ionizing radiation to damage the desoxyribonucleic acid (DNA) of malignant cancer cells, leading to tumor cell death or inactivation. Photons and charged species such as electrons, protons, or heavier ions (to name the most widespread applied species) can be utilized for radiation therapy. Cell damage occurs mainly direct for charged particles and mainly indirect for photons through ionization of water, creating free radicals such as H_20^+ (water ion) or $OH\bullet$ (hydroxyl radical) which subsequently damage the cancerous cell DNA, as the most radiation sensitive cell component.

The following chapter focuses on selected technical and physical aspects of radiation therapy, specifically high energy photon beams generated with a medical linear accelerator (LINAC) (so called photon external beam radiotherapy (EBRT)) and the interaction of X-ray photons with matter. Other important branches of radiation therapy such as brachytherapy or EBRT with charged particles or EBRT using gamma rays from radioactive isotopes such as ^{60}Co have not been adressed in this thesis and will therefore not be described in the following chapter. Additional information on the physics of radiation therapy can be found in [32, 33, 49, 56].

3.1   The Medical Linear Accelerator

Modern medical LINACs are sophisticated machines featuring different operational systems, mainly consisting of a 360° rotating gantry, the gantry stand, a modulator cabinet, the patient support assembly (e.g. the treatment table or patient positioning devices), and a control console. Figure 3.1 shows an example of a modern LINAC used in radiation therapy.
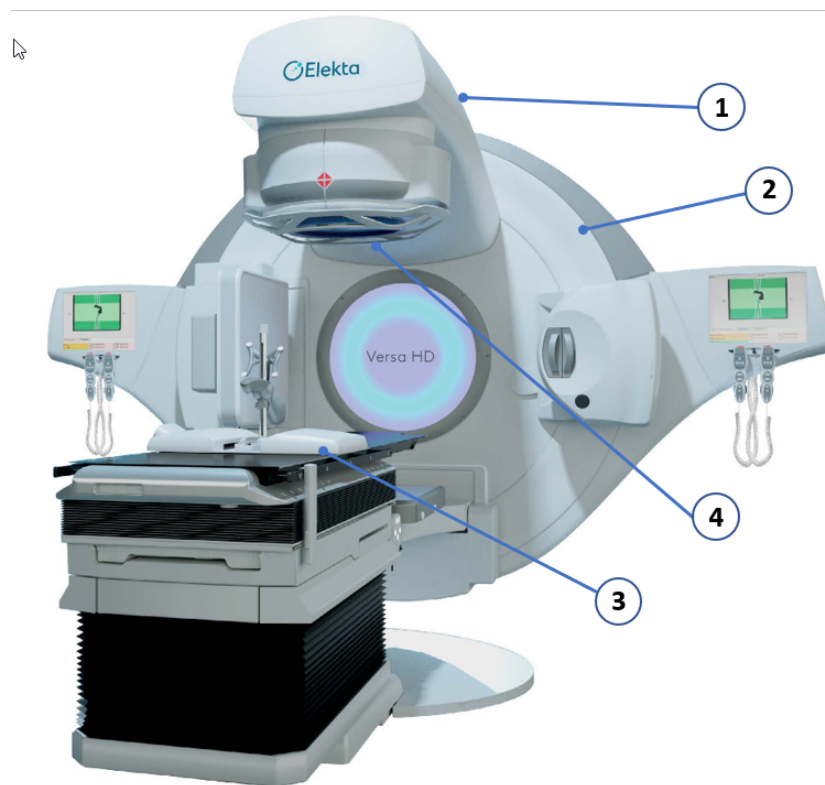
Figure 3.1: A modern medical linear accelerator (LINAC) [17] with the main components: (1) rotating gantry, (2) gantry stand, (3) patient support assembly, and (4) collimator.

Medical LINACs accelerate electrons (produced in the injection system, the so-called "electron gun") in microwave radio frequency (RF) fields in a frequency range between $1 - 10$ GHz. The acceleration of these low energy electrons is carried out in the so-called "waveguide" accelerator. The RF field in the waveguide is produced by the RF power generation system (either a magnetron or a klystron). After acceleration, the electrons are directed onto a high Z material target for Bremsstrahlung conversion in the treatment head using bending magnets. This produces a photon beam in the direction of the LINAC isocenter (the point in space where the LINAC gantry and collimator rotate around). Figure 3.2 shows a schematic diagram of a typical modern medical LINAC with the essential components described in the following sections.
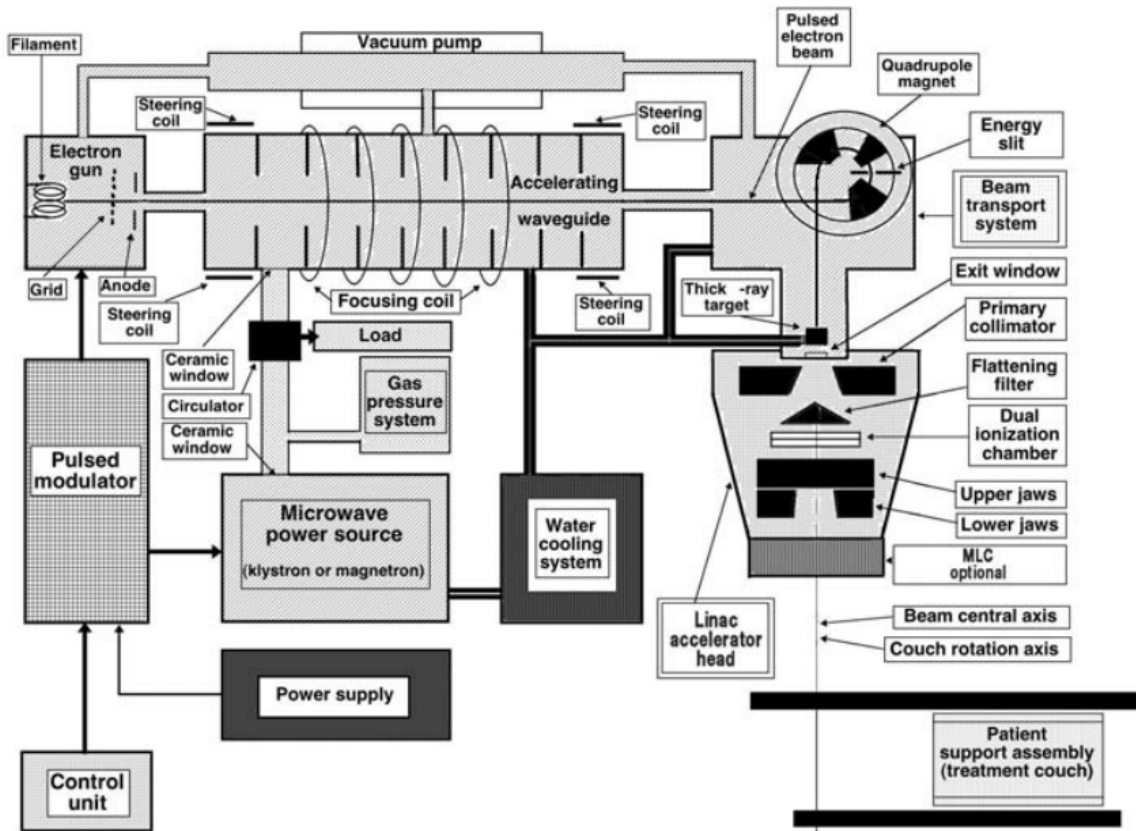
Figure 3.2: Scheme of a LINAC [49].

3.1.1 Injection System or "Electron Gun"

An electrostatic accelerator, called "electron gun", serves as the source for low speed electrons. It contains a heated filament cathode and a grounded anode. Heating of the cathode to temperatures over 1000° C leads to thermionic electron emission. These electrons are accelerated towards the perforated or gridded anode, through which they are inserted into the LINAC waveguide.

3.1.2 Radiofrequency Power Generation System

The RF field in which the electrons are accelerated in the waveguide is produced in the RF power generation system. The RF power source can either be a magnetron or a klystron, which both use electron acceleration and deceleration in vacuum for the RF field generation. The main difference between the two types is that a magnetron is a high power RF field source, while a klystron is rather a power amplifier for microwaves generated by an RF oscillator. A pulsed modulator produces the high voltage, high current and short duration pulses required by the RF power source and the electron gun.

3.1.3   Waveguide

The RF field is transmitted into the waveguide for acceleration of the electrons which enter from the electron gun. Waveguides are evacuated metallic structures containing rectangular or circular cross-sections. Modern waveguides can be divided into two types: *Traveling wave structure* waveguides, in which microwaves enter on the side of the electron gun and propagate towards the high energy end. The microwaves are either absorbed without reflection, absorbed into a resistive load, or fed beck into the waveguide input end. With *standing wave structure* types, a conducting disk is placed at the ends of the waveguide, where the RF power is reflected, leading to a standing wave. Standing waveguides usually are more efficient, because every second cavity carries an electric field, while in a traveling wave configuration, only every fourth cavity is suitable for electron acceleration. Therefore the length of a LINAC waveguide with standing wave structure can be reduced by 50 % while maintaining the same energy.
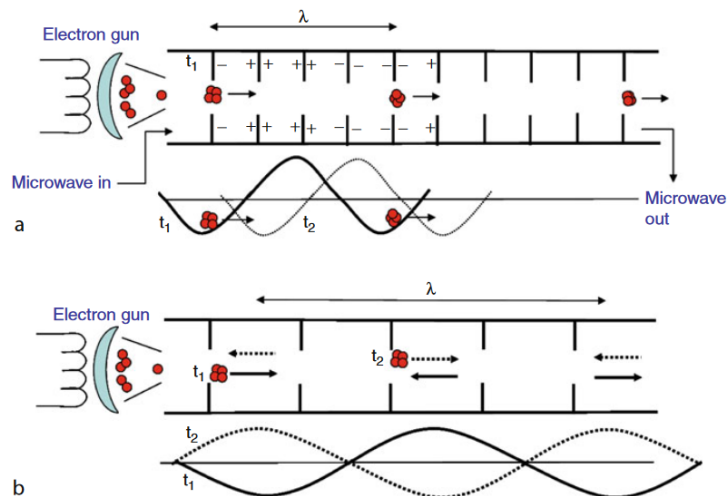
Figure 3.3: Simplified layouts of a traveling waveguide (a) and a standing waveguide (b), adapted from Zhu and Wang [73]. The red spots show electron bunches and the electric field distributions along the waveguide are displayed underneath the layout. In the traveling wave structure (a), the arrow shows the direction of the electric field on the electron bunches with the polarity on the cavity walls. The arrows in the standing wave structure layout (b) show the negative electric field direction at timepoints t_1 and t_2.

3.1.4 Electron Beam Transport

After the accelerated electron beam exits the waveguide, a bending magnet is needed to direct the beam towards the isocenter (for conventional LINACs). There are three different electron bending systems: 90° bending, achromatic 270° bending, or slalom 112.5° bending. Usage of the 90° bending system has become obsolete for medical LINACs as electrons of different energies will be bended in various ways using this type of configuration, so either achromatic or slalom bending systems along with steering and focusing coils are used for the generation of a focused electron beam.
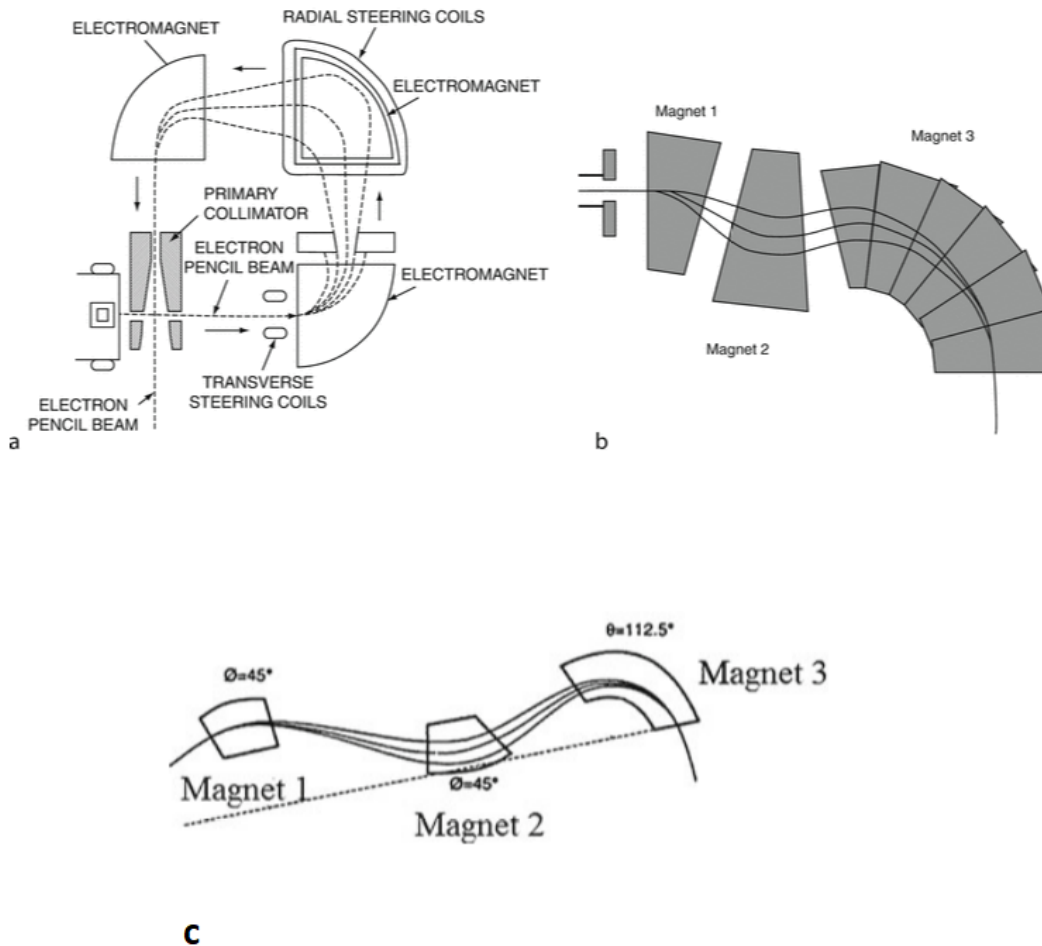
Figure 3.4: Three different types of achromatic focusing bending magnets: a) 270°, b) 90° [73], and c) slalom 112.5° [20]

3.1.5 Treatment Head

The focused and aligned electron beam is then brought into the treatment head, which mainly consists of one or more retractable X-ray targets, flattening and scattering filters, a fixed primary and an adjustable collimator, and ionization chambers. When the electrons collide with the *X-ray target* of high-Z material (e.g. tungsten), Bremsstrahlung and characteristic X-rays are produced. The resulting maximum energy of the X-ray energy spectrum equals the incident electron energy due to Bremsstrahlung interactions.

A *primary collimator* assembly is located directly below the target and confines the photon beam into a cone-shaped beam and defines the maximum field size of the LINAC. It is followed by a scattering foil and a *flattening filter*, which create a uniform flat beam profile with reduced scattering. For higher dose rates and therefore faster treatment times, the flattening filter can be removed (in combination with modern fluence modulating techniques). The dose rate, beam symmetry, and beam homogeneity are continuously monitored during dose delivery in the treatment head using segmented *ionization chambers*. Below these chambers are two or four *secondary (movable) beam defining collimators*, often referred to as "jaws".

Figure 3.5: The process of photon beam generation from an electron beam in the treatment head [28].

A schematic overview of the components in the LINAC treatment head and the process of photon beam generation from an electron beam can be found in figure 3.5. In modern medical LINACs, the second pair of jaws is usually replaced by a *MLC* (see an example in figure 3.6), with up to 160 leaves (80 leaf pairs) and field sizes of up to $40x40\,cm^2$ to spatially vary the beam shape.
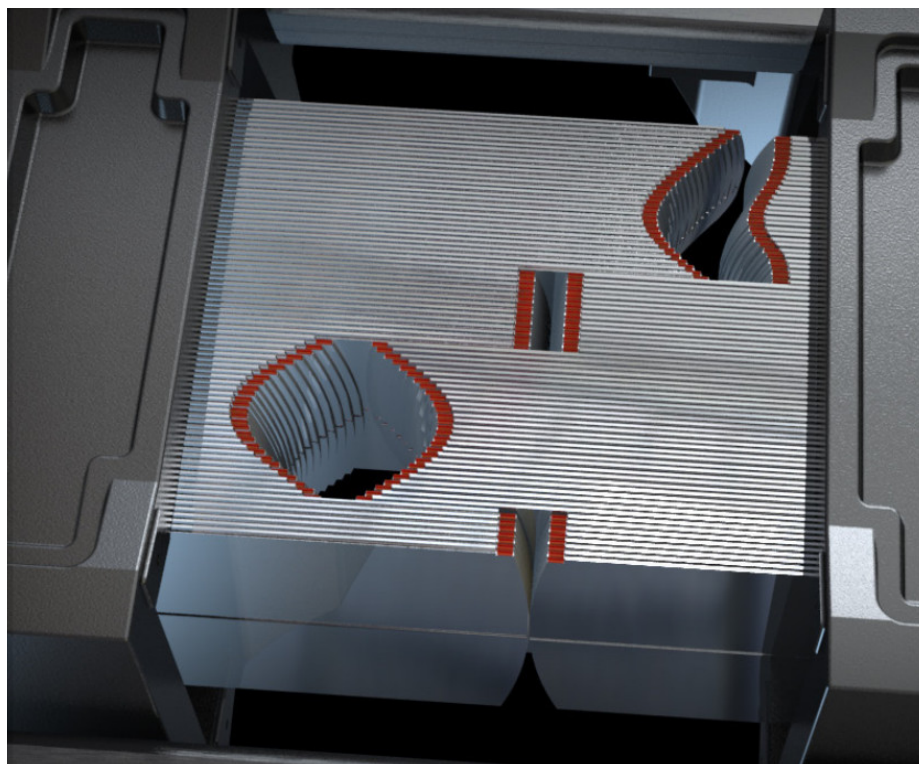
Figure 3.6: Image of a modern MLC with 80 leaf pairs for the creation of various field shapes and sizes [16].

3.2 Interaction of X-ray Photons with Matter

The photon beam produced by the LINAC is characterized in terms of photon fluence and energy fluence. The photon fluence Φ (which may also be used to describe charged particle beams as particle fluence) is defined as the quotient dN by dA, with dN as the number of photons entering an imaginary sphere of a cross-sectional unit area dA.

$$\Phi = \frac{dN}{dA} \tag{3.1}$$

Energy fluence Ψ is defined as the quotient of dE by dA, where dE is the radiant energy on a sphere of cross-sectional unit area dA.

$$\Psi = \frac{dE}{dA} \tag{3.2}$$

Energy fluence can be calculated from photon fluence (assuming a monoenergetic beam) using:

$$\Psi = \frac{dN}{dA}E = \Phi E \tag{3.3}$$

The photon fluence is inversely proportional to the square of the distance from the photon beam point source, which describes the photon beam propagating through vacuum (inverse square law), neglecting attenuation in air. When the photon beam enters any medium, it is not only affected by the inverse square law. Absorption and scattering inside the medium (e.g. the patient or a phantom) also affect the photon beam. The number of photons dN reduced by an absorber medium is proportional to the number of incident photons N and the thickness of the absorbing material dx. This can be described as:

$$dN = -\mu N dX \tag{3.4}$$

with μ being the *attenuation coefficient*. This differential equation for attenuation can be solved in terms of intensity, where $I(x)$ is the intensity transmitted through a thickness x and I_0 is the initial intensity impinging onto the absorber medium.

$$I(x) = I_0 e^{-\mu x} \tag{3.5}$$

In general, the attenuation coefficient μ depends on the photon energy and characteristics of the medium. The number of photons decreases with the absorber thickness. With μ depending on the density of the material, an independence of density can be achieved by division of μ with the density ρ, resulting in the *mass attenuation coefficient* $\frac{\mu}{\rho}$ which is now only dependent on the atomic composition of the medium, specifically the attenuator atomic number Z. Figure 3.7 shows the dominance of the three major photon interaction forms (photoelectric effect, Compton effect, and pair production) relative to the atomic number Z in a wide energy range of relevance for diagnostics and therapy.
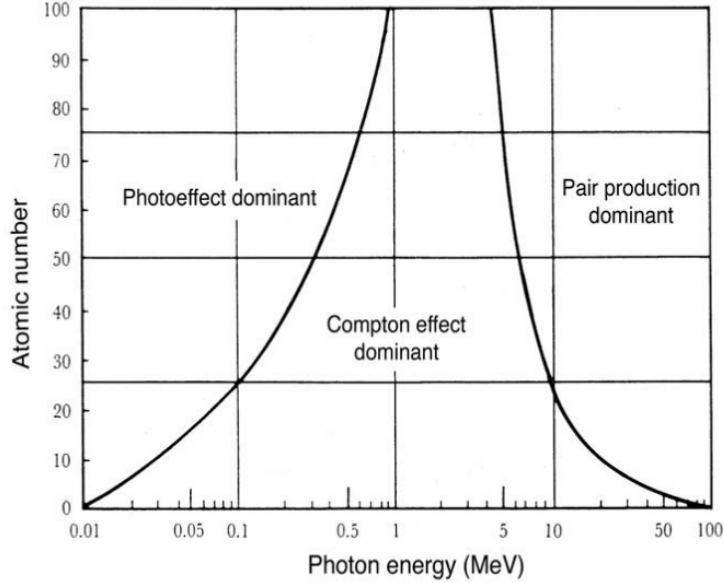
Figure 3.7: Relative predominance of the three major types of photon interaction with matter: Photoelectric effect at low photon energies, Compton effect at intermediate energies, and pair production at high energies. Both curves indicate regions of atomic number and photon energy, where the neighboring effects are equally probable [49].

The photon beam produced by medical LINACs can be attenuated by five major types of interactions with matter: *Photonuclear reactions* (1), the reactions between the photons and the nucleus, are important only for photon energies approximately > 10 MeV. In three processes, photons interact with the atomic shell: *coherent (Rayleigh) scattering* (2), *photoelectric effect* (3), and *Compton effect (incoherent scattering)* (4). In the Coulomb field of the nucleus *pair production* can occur for for energies > 1.022 MeV, as well as *triplet production* in the Coulomb field of the atomic electrons for energies > 2.044 MeV (5). The resulting *total mass attenuation coefficient* as the sum of all individual coefficients for the above-mentioned processes neglecting photonuclear reactions can be denoted as:
or *triplet production*

$$\mu/\rho = \sigma_{coh}/\rho + \tau/\rho + \sigma_c/\rho + \kappa/\rho \tag{3.6}$$

with attenuation coefficients σ_{coh}, τ, σ_c, and κ for coherent scattering, photoelectric effect, Compton scattering, and pair production, respectively. Figure 3.8 shows the total mass attenuation coefficients and the individual coefficients for monoenergetic photons in water and lead.
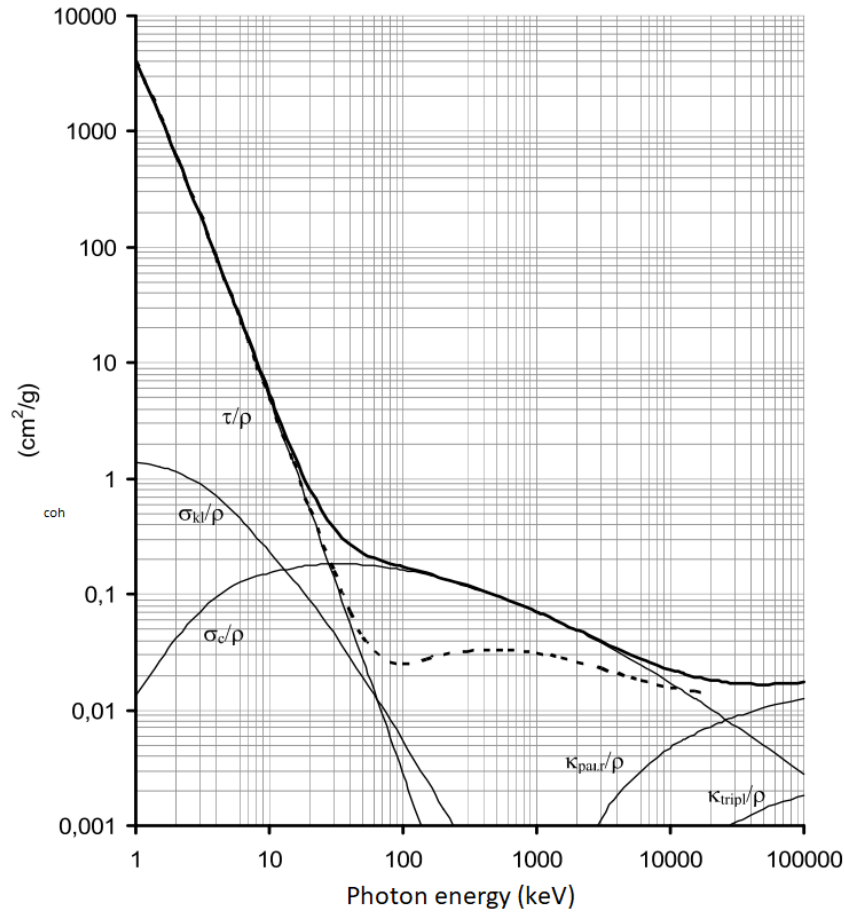
Figure 3.8: Total and partial mass attenuation coefficients for monoenergetic photons in water (left) and lead (right) [54].

3.2.1   Photonuclear Reactions (Photodisintegration)

A photon can directly interact with the atomic nucleus through its electromagnetic characteristics, which is called *photonuclear reactions* or *photodisintegration* (for a schematic representation see figure 3.9). The energy of the incident photon is absorbed by the nucleus, leading to an excitation. Above a certain threshold energy the excitation energy can lead to an emission of one or more nucleons. For most elements, this threshold energy is in the range between 6 MeV and about 20 MeV. In radiation protection, this effect has to be accounted for, because activation of air, certain materials, or the patient can occur when using photon beam energies above 10 MeV. In addition, a not negligible neutron flux can result at high radiation intensities.
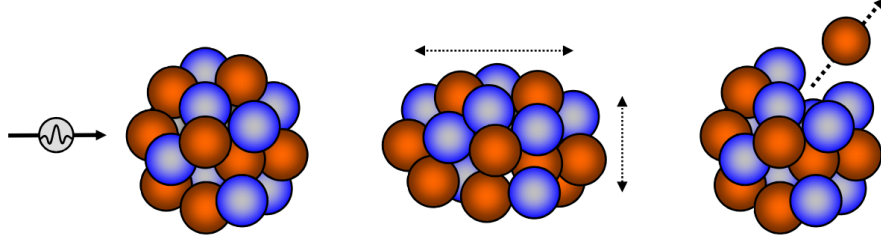
Figure 3.9: Schematic representation of a photonuclear reaction. Through photon absorption the atomic nucleus is excited, which leads to an emission of one or more nucleons (right side) [33].

3.2.2 Coherent (Rayleigh) Scattering

Coherent scattering, which is also known as classical or Rayleigh scattering, is the process of an electromagnetic wave passing near a strongly bound electron causing the electron to oscillate. Energy with the same frequency as the incident wave is radiated from the oscillating electron, without any changes in energy or absorption by the medium. The wavelength of the emitted electromagnetic wave is equal to the wavelength of the incident wave. The attenuation coefficient for coherent scattering σ_{coh} above 10 keV is proportional to the atomic number of the absorber atomic number Z and the absorber material density ρ:

$$\sigma_{coh} \propto \rho \cdot \frac{Z^{2.5}}{A \cdot E_\gamma^2} \approx \rho \cdot \frac{Z^{1.5}}{E_\gamma^2} \qquad (3.7)$$

Figure 3.10: Schematic representation of coherent or Rayleigh scattering. The incident photon excites the electron hull to oscillations. The scattered photon has the same energy as the incident photon, but usually a different direction [33].

For clinical photon radiation therapy, coherent scattering can be neglected as no energy transfer is involved, the scattering effect is negligible, and it is only probable in materials with high atomic numbers and for low energy photons (< 100 keV) [32, 33].

3.2.3 Photoelectric Effect

A photon can also interact with a tightly bound orbital electron of an inner shell (preferentially the K or L shell), where the energy of the incident photon $h\nu$ is absorbed by the atom and transferred to an electron of the atom. This phenomenon is called the *photoelectric effect*. The emitted electron ("photoelectron") has a kinetic energy $E_{kin} = h\nu - E_B$, with E_B as the binding energy of the electron. As the electron is emitted, the vacancy in the atomic shell has to be filled by an electron in one of the outer shells under the emission of characteristic X-rays. Another alternative is the emission of monoenergetic so-called Auger electrons or secondary emitted electrons to which the energy has been transferred. Figure 3.11 shows a schematic representation of the photoelectric effect with characteristic X-ray emission.
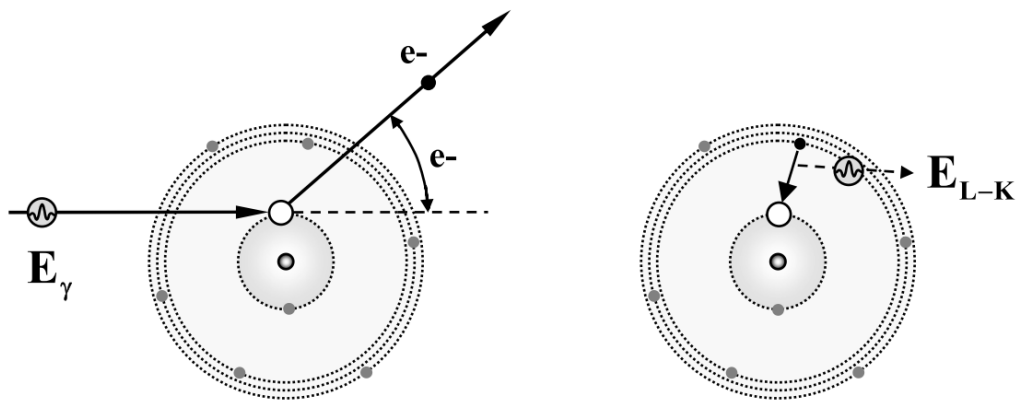
Figure 3.11: Schematic representation the photoelectric effect (occuring on an electron of the K shell). The atomic shell is ionized through absorption of the incident photon (left) and the vacancy in the atomic shell is filled with an electron from an outer shell (right). The remaining energy is emitted as a characteristic photon (or a cascade of Auger electrons) [33].

The photoelectric attenuation coefficient τ describes the probability per unit path length for photoelectric absorption and is directly proportional to the density ρ and increases with the atomic number ($\propto Z^n$). The exponent of the atomic number n has a value of $n \approx 4$ for high atomic numbers and $n \approx 4.5$ for low atomic values [33].

$$\tau \propto \rho \cdot \frac{Z^n}{A} \approx \rho \cdot \frac{Z^{4\text{-}4.5}}{A} \qquad (n = 4\text{-}4.5) \tag{3.8}$$

The angular distribution of photoelectrons is dependent on the the photon energy. For higher energies, more photons are emitted forward [32, 33].

3.2.4 Compton Effect (Incoherent Scattering)

The *Compton effect* describes an inelastic interaction of a photon with an electron in the outer shell, which is bound weakly ("free"). An electron is considered "free" or "quasi-free", when the energy of the incident photon $E_{\gamma 0}$ is much higher than the binding energy of the electron. The photon energy and its momentum $\vec{p}_{\gamma 0}$ are partially transferred to the electron. When the photon and the electron collide, the photon is scattered under an angle φ while the electron is ejected from the atomic shell under an angle θ, which leaves the shell ionized.
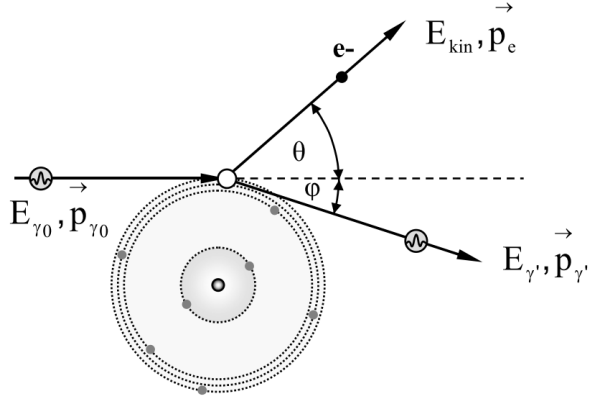
Figure 3.12: Schematic representation of the Compton effect as an inelastic interaction between an incident photon and a weakly bound hull electron [33].

The remaining energy of the scattered photon E'_{γ} is calculated applying the laws of conservation of energy and momentum as a function of the incident photon energy $E_{\gamma 0}$ and the photon scattering angle φ, with $E_0 = m_0 c^2 = 511 \, \text{keV}$:

$$E'_{\gamma} = \frac{E_{\gamma}}{1 + \frac{E_{\gamma}}{m_0 c^2} \cdot (1 - cos\varphi)} \tag{3.9}$$

The change in photon wavelength $\Delta\lambda$ can be derived using the Compton wavelength $\lambda_C = \frac{h}{m_e c}$ as:

$$\Delta\lambda = \lambda_C (1 - cos\varphi) \tag{3.10}$$

The energy transferred to the electron E_{kin} is calculated from the difference of the remaining photon energy after scattering E'_{γ} and the incident photon energy $E_{\gamma 0}$, with a negligible binding energy E_B as the electron is considered "free" :

$$E_{kin} = E_{\gamma 0} - E'_{\gamma} - E_B \approx E_{\gamma 0} - E'_{\gamma} \tag{3.11}$$

The energy dependence of the attenuation coefficient for the Compton effect σ_c for energies between $0.2 \, \text{MeV}$ and $10 \, \text{MeV}$ (which is the energy range the Compton effect occurs in most materials) can be described as:

$$\sigma_c \propto \rho \cdot \frac{Z}{A} \cdot \frac{1}{E_{\gamma}} \tag{3.12}$$

The Compton effect is the dominant photon interaction process in human soft tissue and other materials with low atomic number Z for photon beam energies between $30 \, \text{keV}$

and 30 MeV and therefore the main effect of beam attenuation in external beam radiation therapy using photons [32, 33].

3.2.5   Pair Production

Photons can also interact with the electrical field of charged particles, such as the atomic nucleus or electrons. If the photon energy exceeds the energy-mass-equivalent for electrons $(2m_0c^2 = 2 \cdot 511\,\text{keV} = 1.022\,\text{MeV})$ the photon can disappear completely in the strong Coulomb field of atomic nuclei and an electron-positron pair with a maximum energy of $E_{kin} = E_\gamma - 1.022\,\text{MeV}$ is produced. This process is referred to as *pair production*. The probability of pair production per unit path length κ increases logarithmically with the photon energy E_γ and proportionally with Z for light and medium-weight elements [33]:

$$\kappa_{pairproduction} \propto Z \cdot \rho \cdot logE_\gamma \qquad | \; E_\gamma > 1.022\,MeV \qquad (3.13)$$

The incident photon kinetic energy is divided between between the rest mass energy and the kinetic energy of the electron–positron pair. It can be distributed in any available way to electron and positron for large photon energy, although the most probable distribution is half the available kinetic energy on each particle. Positron and electron move throughout the absorber medium and deposit energy in small portions in Coulomb excitation and ionization with the atomic electrons of the absorber. Once the positron comes to rest, it recombines with a shell electron of the absorber under emission of two annihilation photons (each having 511 keV energy).

If pair production occurs in the field of an orbital electron, three particles share the incident photon energy with a threshold of $4m_0c^2 = 2.044\,\text{MeV}$. This process is know as *triplet production* [32, 33].
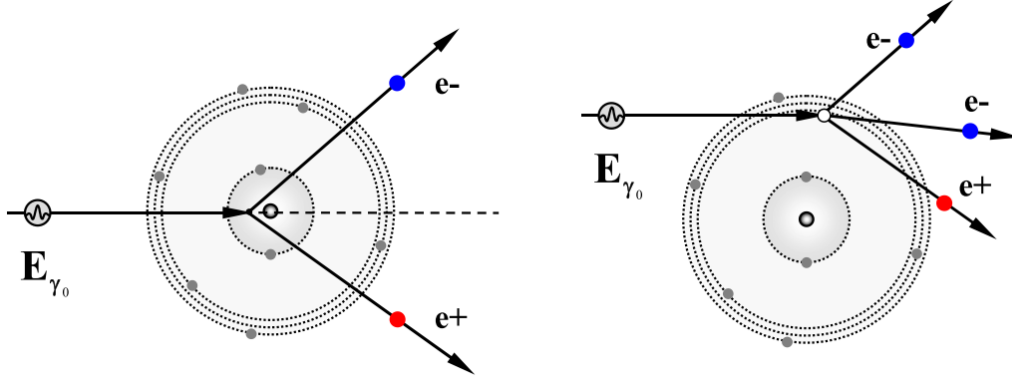
Figure 3.13: Schematic representation of pair (left) and triple production (right). The resulting pair consists of an electron and a positron [33].

3.2.6 Energy Transfer and Absorbed Dose

Compton effect, pair production, and photoelectric effect all lead to an energy transfer (complete or partial) from photons to secondary charged particles (electrons). This energy transfer for ionizing uncharged particles is described by the term <u>k</u>inetic <u>e</u>nergy <u>r</u>eleased per unit <u>mass</u> (KERMA), K, as the quotient of $d\epsilon_{tr}$, the mean sum of all initial kinetic energies of the charged ionizing particles liberated in a mass dm of a medium by the uncharged particles incident on dm [2]:

$$K = \frac{d\epsilon_{tr}}{dm} \tag{3.14}$$

For a photon beam, KERMA is directly proportional to the photon energy fluence Ψ:

$$K = \Psi(\frac{\overline{\mu_{tr}}}{\rho}) \tag{3.15}$$

$\frac{\overline{\mu_{tr}}}{\rho}$ denotes the spectrum averaged mass energy transfer coefficient of the medium, which is less dependent on the density of the absorber. The mass energy transfer coefficient is defined as:

$$\frac{\mu_{tr}}{\rho} = \sum_{j} f_j \frac{\mu_j}{\rho} = f \frac{\mu}{\rho} \tag{3.16}$$

f_j denotes the average fraction of photon energy that is transferred to kinetic energy of charged particles in interactions of type j, f being the average of f_j, and $\frac{\mu}{\rho}$ the mass attenuation coefficient [59].

A measure for the quantification of deposed energy is *absorbed dose D* as the expectation value of imparted energy $d\epsilon$ per mass unit dm.

$$D = \frac{d\epsilon}{dm} = \frac{1}{\rho}\frac{d\epsilon}{dV} \tag{3.17}$$

The unit of measure for absorbed dose is gray ($Gy = J \cdot kg^{-1}$). Energy is imparted in matter for indirectly ionizing radiation by energy transfer to secondary charged particles, which results in KERMA. Secondly, the kinetic energy from these charged particles is partially transferred to the medium, which results in the absorbed dose, while some energy is lost in the form of bremsstrahlung and annihilation in flight. The amount of KERMA (energy transferred) from the photon beam to charged particles at a particular location does not imply that the energy absorbed by the medium occurs at this same location, due to the finite range of secondary electrons resulting from photon interactions besides radiation losses.

When it comes to the irradiation of tumors or lesions in the lung region, the mass dm of the surrounding tissue (which can be approximated as air) is relatively low. With the same amount of energy transferred, KERMA increases, but the absorbed dose is decreased.

Chapter 4

Modern Photon Therapy and Treatment Planning

The complete process of modern radiation therapy can be described using the so-called "chain of radiotherapy"[10, 55]. At first, the patient needs to be immobilized reliably and exactly before initial imaging to guarantee a precise dose delivery over the course of the whole treatment chain. Immobilization is mostly established using casts and moulds and the degree of patient immobilization is always relative to the treatment type (e.g. the highest need for correct and firm patient immobilization arises when using single-fraction high-precision stereotactic irradiation). Subsequently, the imaging and tumor localization process begins: using 3D imaging, the tumor (or lesion) and surrounding organs-at-risk (OARs) can be determined for treatment planning. After delineation of the treatment target(s) and the OARs, the dose is calculated and optimized and the resulting treatment plans are visualized and evaluated using a treatment planning system (TPS). There are two standard procedures available in modern radiation therapy clinics. In three-dimensional conformal radiation therapy (3D-CRT) the treatment machine parameters (geometric and dosimetric) are evaluated in a trial and error process, in search of the most adequate beam directions, field shapes and resulting dose from each individual field. In contrast to this manual forward planning approach, inverse planning for intensity modulated radiation therapy (IMRT) techniques uses predefined treatment goals for the determination of treatment machine parameters. The TPS uses these treatment goals as an input for an automated optimization of a certain treatment plan. The final treatment plan is evaluated by medical physicists physicians in terms of target volume dose coverage and dose to OARs. In addition, the 3D dose distributions among relevant regions of interest (ROIs) are reduced to the form of a dose-volume histogram (DVH), where the plan quality can be evaluated using simplified measures in a graphical 2D format.

Patient positioning during treatment includes the same set-up devices used for immobilization during imaging, as all characteristics of these device must be known throughout the treatment planning process. In addition, the correct patient position at the LINAC is nowadays ensured using image guided radiation therapy (IGRT), where the current

position is assessed with respect to planned position to perform corrections using two-dimensional (2D), 3D, or even 4D imaging techniques. In the past years, surface guidance was also established as a possible way of patient positioning during initial imaging and treatment. The actual dose delivery with modern medical LINACs using photons or electrons has been described in the previous chapter. Quality assurance and quality management in radiation therapy is a crucial step in the treatment process chain as all steps and all links are subject to various inaccuracies and possible errors. Minimization of these potential errors can only be ensured with a full quality management system including dosimetry checks, hardware and software test, and full documentation and standardization of all processes. More details on the "chain of radiotherapy" can be found in Brady et al. [10].
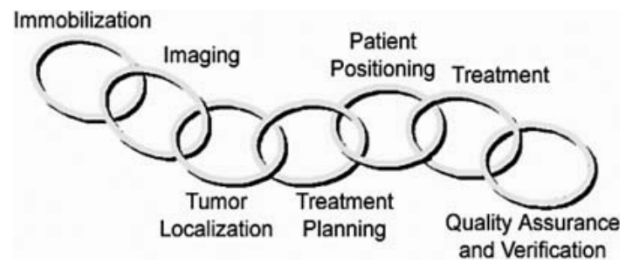
Figure 4.1: The chain of radiotherapy [10]

The following chapter describes the processes of medical image acquisition for radiation therapy. For the studies performed in this thesis, X-ray computed tomography (CT) was the main source of medical images.

Other image acquisition methods that are already in use in radiation therapy help to gain further information on tumor type and localization, e.g. positron-emission tomography (PET) and magnetic resonance imaging (MRI). As these modalities have little influence on the studies performed, they will not be described in detail in this thesis. As surface imaging was one of the key features for all investigations, one section will give a brief overview of modern systems for surface-guided radiation therapy (SGRT).

Secondly, an overview of radiation therapy treatment techniques (including the process of target definition) from simple 2D to 3D intensity-modulated techniques and so-called stereotactic body radiation therapy (SBRT) will be given.

4.1 Medical Image Acquisition for Radiation Therapy

4.1.1 X-ray Computed Tomography

For radiation therapy, the acquisition of X-ray computed tomography (CT) images does not only play a fundamental role in tumor identification, localization, and delineation. The second major part is the use of CT in treatment planning, especially for a quantitative characterization of the physical properties of heterogeneous tissue in terms of electron densities for dose calculation [10]. X-ray computed tomography (CT) imaging results in the production of several axial slices representing the X-ray attenuation characteristics of tissue, providing 3D information of the patient's anatomy with high contrast and resolution, based on the tissue electron density for tissues with considerable differences in their individual attenuation properties. The 3D information is acquired by translating the couch through the CT gantry. Simplified, an X-ray source (tube) is rotating around the patient, in which the X-rays are attenuated and then measured by an X-ray detector, which consists of about 10^5 channels per slice. Modern CT detectors consist of a scintillator crystal in combination with a photodiode [56]. The detector measures the beam intensity I according to:

$$I = I_0 e^{-\int_S \mu(x)dx} \tag{4.1}$$

with I_0 being the beam intensity before entering the medium for a beam of single-energy photons traveling through a inhomogeneous medium along a straight line S, with a linear attenuation coefficient $\mu(x)$. As in reality X-rays are polychromatic, equation 4.1 can be used as an approximation for a monochromatic beam. For a set of measured projection values $p(L)$, the negative logarithm of each intensity measurement along a line corresponds to the line integral along the line L of an object's linear attenuation coefficient distribution $\mu(x, y, z)$:

$$p(L) = -ln\frac{I(L)}{I_0} = \int_L dL\mu(x,y,z) \tag{4.2}$$
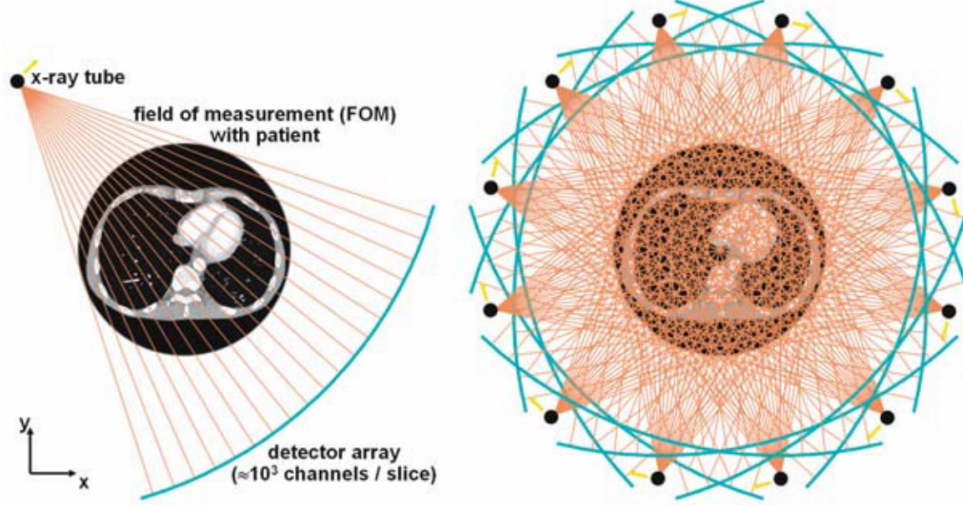
Figure 4.2: Schematic representation of a clinical CT acquisition. Left: The X-ray photon attenuation is measured in the detector array along straight lines. Right: In order to gain enough information for 3D image reconstruction, a large number of line integrals are measured during the CT gantry rotation[10].

With enough information gathered from multiple measurement angles, the projection values $p(L)$ can be used for image reconstruction. For single slice CT scanners (at a fixed table position) this would just be the convolution of all projection data with a reconstruction kernel and the backprojection into the image domain, which is called *filtered backprojection* [10]. Image reconstruction for spiral CT scanners (with a continuously rotating gantry and the patient moving through the gantry with constant speed), requires z-interpolation as an additional reconstruction step. Virtual scan data corresponding to a circular scan at the desired reconstruction plane is synthesized before obtaining the final image via filtered backprojection. The result is a reconstructed image $f(x, y, z)$ and is represented by the individual tissue attenuation values normalized to the Houndsfield scale: Air with zero attenuation is given a value of -1000 HU and water with an attenuation of μ_{water} as 0 HU. The CT attenuation value μ for the individual tissue electron density can therefore be represented by CT values:
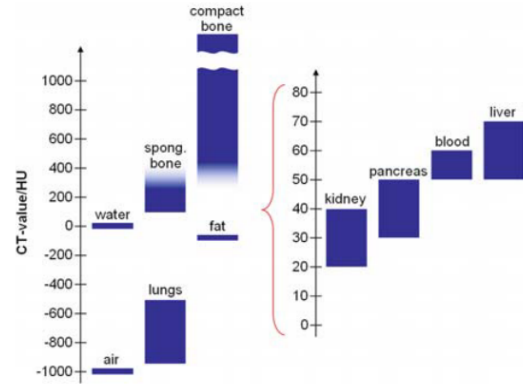
Figure 4.3: Ranges of CT HU for certain organs[10].

$$CT = \frac{\mu - \mu_{water}}{\mu_{water}} \cdot 1000 \, HU \qquad (4.3)$$

A CT value of any voxel in the reconstructed 3D image dataset is directly related to

the attenuation values (which are proportional to the material density), therefore one can interpret the CT value as the density of the object at this certain location. The main difference between a standard, radiological CT and a CT used for radiation therapy treatment planning is the correct relationship between CT values and the electron densities, as tissue heterogeneities have to be considered precisely [57]. This results in a so-called *planning CT* for the treatment process.

CT volume datasets can be acquired in two different scanning modes: *circular* scanning, also known as *axial* CT scanning, where a number of consecutive slices are scanned using circular tube-detector rotations with small table shifts. More widely used nowadays is *helical* or *spiral* scanning, where the X-ray tube is in constant rotation around the patient translated continuously through the CT gantry. For increased acquisition speed, modern CT scanners use multiple detector rows in the detector array for the acquisition of multiple slices per rotation, which presents new challenges in image reconstruction. This is called *multi-slice CT*.

4.1.2 Four-dimensional Computed Tomography

In radiation therapy of tumors or lesions in the thoracic and upper abdominal region, the knowledge of tumor motion with respect to the patient's natural breathing motion becomes inevitable and considerable uncertainties still remain due to respiratory motion [69]. Image quality in 3DCT scanning can be deteriorated due to respiratory motion [22] and correct treatment delivery can be challenging. Respiratory-correlated computed tomography (4DCT) is a method, where time-resolution is introduced as a fourth dimension. 4DCTs reduce breathing induced motion artifacts or distortions - which can occur in "static" 3DCT scans - and allow for detailed investigation of tumor movement with regards to time [18, 22, 30, 36, 39]. Although motion could be deducted from the raw CT data, a certain type of surrogate signal helps in sorting the acquired oversampled CT raw dataset into multiple datasets, so-called 4DCT phases to depict the maximum motion amplitude. The 4DCT dataset is usually split into phases of 10% or 5% of the breathing cycle, with the 0% being the maximum inspiration or end-of-inhale (EOI) breathing phase by convention.

4DCT Acquisition Methods: Spiral and helical

4DCT scans are collected over multiple breathing cycles either in *spiral* mode, where the patient breathing curve is recorded and each reconstructed slice is assigned to a certain breathing phase [18, 67], or an oversampled dataset of the raw CT data is acquired while simultaneously recording the breathing curve using a surrogate breathing signal [30, 36, 39]. Using the patient breathing curve, the 4DCT breathing phases can be reconstructed from the raw dataset. This is called the *helical* 4DCT acquisition mode.
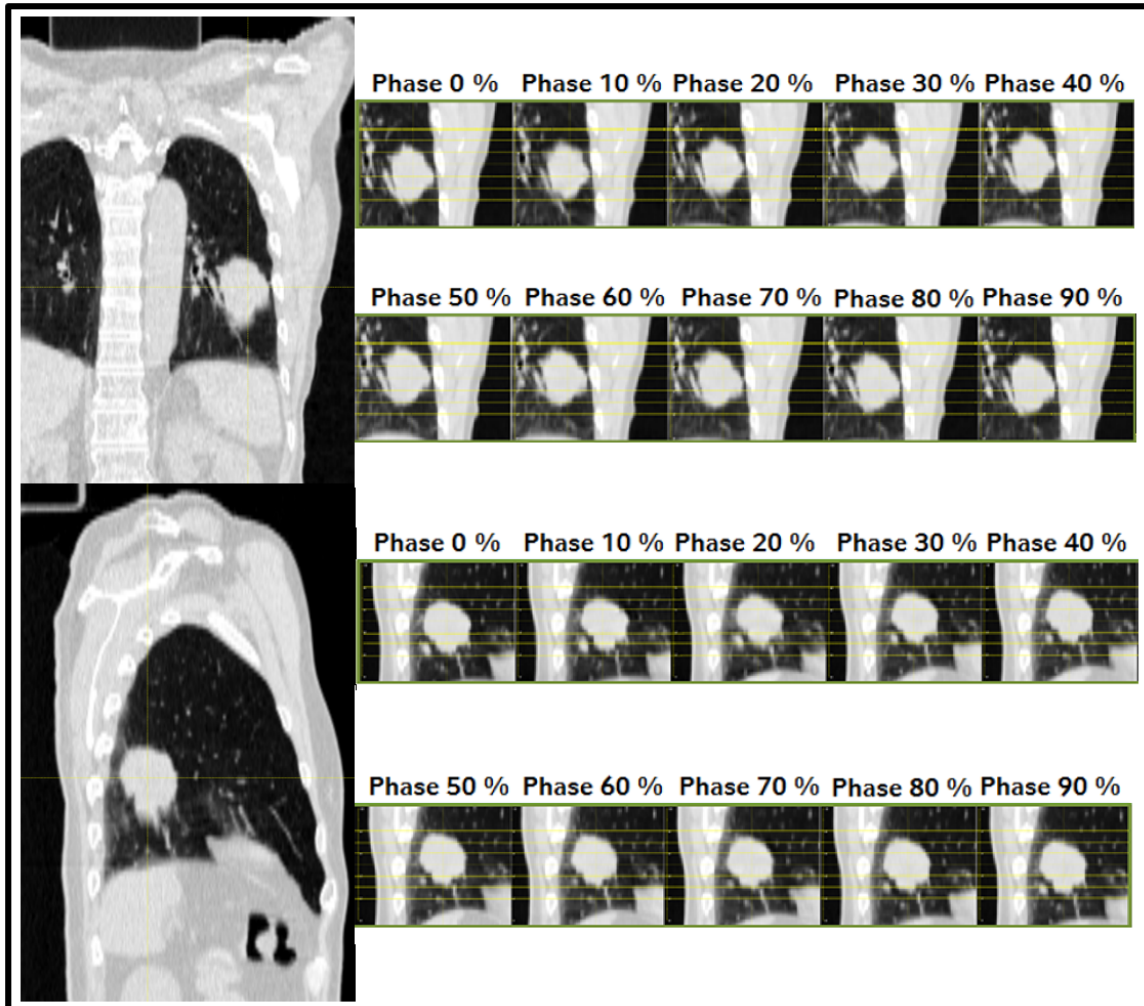
Figure 4.4: Coronal (top) and sagittal (bottom) slices as represented in a 3DCT (left side) and the corresponding 4DCT phases (0 % to 90 % in 10 % steps).

Phase Sorting Algorithms

There is a difference in the way the breathing curve is sampled for 4DCT reconstruction: One can either user *phase-based* or *amplitude-based* sorting. In *phase-based* (or time-based) sorting, a distinct point on the breathing curve (such as maximum inspiration or expiration) is determined and the breathing curve is divided into equidistant sectors in between two maxima or minima. The phased-based 4DCT technique has been used quite commonly [18, 30, 36, 48] as it has been originally derived from 4D cardiac imaging [46]. More recently, *amplitude-based* reconstruction methods, where the breathing phase is determined by the amplitude of the breathing curve, were reported to have better image quality and less motion artifacts [37, 71]. The importance of phase-based approaches have been reported and discussed widely in current literature [3, 22, 35]. In chapter 6, we discuss a

rather novel method of 4DCT sorting, the local amplitude-based sorting (LAS) approach, that was developed and implemented as part of this thesis.

4.1.3   Surface Imaging

Surface imaging for radiation therapy, sometimes referred to as surface-guided radiation therapy (SGRT), has been introduced into multiple clinics in the last decade. SGRT in general is contactless and fast and can be used for patient positioning and intrafractional motion monitoring. One of the obvious applications in the "chain of radiotherapy" [55] is patient positioning. Conventionally, the patient is positioned inside the treatment room according to an in-room laser system with skin marks drawn directly on the patient to ensure to same patient position as during CT acquisition. Using surface guidance the potential advantages for daily patient positioning are increased accuracy within body regions, where no skin marks are drawn on. The advantages of SGRT for patient positioning, especially for tumors with superficial location, were evaluated in [8, 12, 47].

Intrafractional motion monitoring has been proven to be the second successful application of SGRT. When monitoring the patient surface throughout the entire treatment fraction, one can determine intrafractional shifts and account for them in a quick and reproducible way by registering the "live" patient surface to the planned surface. As the patient is not immobilized on the treatment table in a traditional way and interfractional motion could therefore increase, an interconnection between the optical surface scanner and the LINAC can interrupt the treatment beam once patient movements outside of a certain pre-determined threshold tolerance are detected. Additional information on surface guidance for intrafractional motion monitoring can be found for example in Reitz et al. [51].

In addition, several special techniques, such as deep-inspiration breath-hold (DIBH) or whole brain radiation therapy (WBRT) using open masks or even stereotactic radiosurgery (SRS) can be performed with the help of surface imaging. Optical surface scanners can also be used for the previously described 4DCT imaging technique (see section 4.1.2) to measure the chest or abdominal movement as a surrogate for breathing motion. For DIBH techniques, where the patient is treated in deep inspiration in order to either separate OARs geometrically from the irradiated volume (e.g. the heart from the patient breast in breast radiation therapy) or to minimize target motion, SGRT is nowadays widely used in daily clinical routine [13, 58].
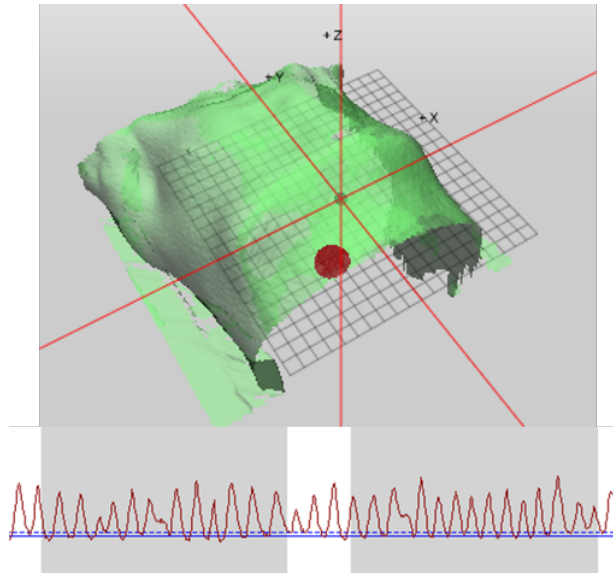
Figure 4.5: A surface image of a patient upper body (green) and the corresponding breathing curve measured at the location of the red spot in the surface image.

4.2 Radiation Therapy Treatment Techniques

The following section gives an overview of the treatment planning process after the medical image acquisition. Using the information from the *planning CT*, certain ROI structures are defined: the tumor or lesion and the possible microscopic spread of malignant cells to be irradiated in addition to all OARs near the tumor location. In addition to the planning CT, MRI and PET images also help in the tumor delineation process and are used for *target definition*. As uncertainties are always present in radiotherapy (e.g. isocentric deviations due to rotation of the LINAC gantry, collimator, table, or in-room imaging devices), margins are added to the previously defined target(s) to ensure sufficient dose delivery or to OAR structures to meet certain dose criteria. The treatment plan is afterwards generated in a treatment planning system (TPS) and dose distributions are evaluated by physicians and medical physicists. The dose of a typical treatment plan is not irradiated on the patient in one delivery, but rather distributed in *fractions* of the desired dose.

4.2.1 Target Definition

Target definition is a complex and broadly discussed subject. In general, a radiation oncologist outlines the volume to be irradiated in addition to all relevant OARs on the underlying CT dataset. Information from multiple sources has to be taken into account for correct target volume delineation, such as the results of radiological and clinical investigations, tumor staging, surgical, histological, and pathological information, the patient's history, or the patient compliance for treatment. MRI also aids tumor delineation through the high accuracy in visualization of anatomical structures with high soft tissue contrast. Using radioactive tracers, functional imaging techniques such as PET and single-photon emission computed tomography (SPECT) can visualize the tumor, because selected tracers have a higher affinity for tumorous tissue with respect to normal tissue. Not only target definition, but also OAR delineation needs to be carried out with high precision as a treatment plan is evaluated not only by the target dose coverage, but also with respect to the dose sparing to OARs [10].

Standard concepts and a standard nomenclature for target definition and delineation have been specified in ICRU reports 50 [24] and 62 [25]: The gross tumor volume (GTV) is the macroscopic (or gross) extent of the tumor and is determined using the CT and/or MRI data in addition to other clinical or radiological investigations. Because of possible surrounding microscopic tumor infiltration, the GTV has to be extended to a second volume, the clinical target volume (CTV) using an adjustable margin. Later on, the internal target volume (ITV) can be applied to account for possible intrafractional physiological organ or tumor movements (e.g. respiratory motion, pulsation, variable volume of rectum or bladder, variations in tumor size or shape over the course of the treatment) [25]. An ITV is difficult to define, if several GTV structures (e.g. delineated in all 4DCT phases) are not available. Finally, another margin is added to the CTV or the ITV to account for systematic and random errors and uncertainties in patient setup and beam adjustment
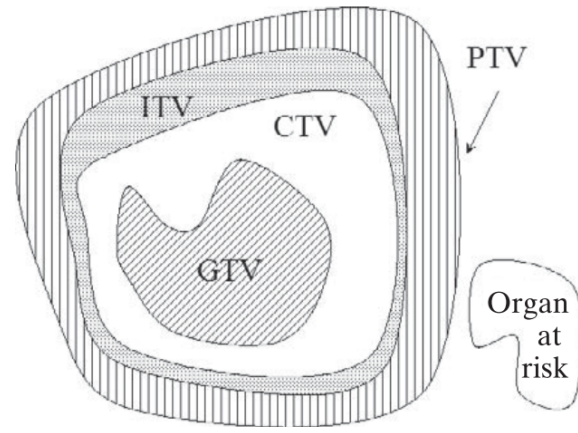
Figure 4.6: Graphical representation [49] of the nomenclature for volumes of interest as defined in ICRU reports 50 [24] and 62 [25].

to form the planning target volume (PTV). The dose is usually prescribed to the PTV structure to ensure that the irradiated dose is delivered to GTV and CTV structures inside the PTV [10].

4.2.2   From Two Dimensional to Three Dimensional Conformal Radiation Therapy

After the announcement of the discovery of X-rays by Röntgen in 1895 [52], little time passed for the first patient suffering from stomach cancer to be treated using X-rays in 1896 [15]. The development of reliable therapeutic equipment which can operate at 250-400 kV for the treatment of superficial tumors took roughly 40 years after the discovery of X-rays. Later on, Cobalt-60 radiation sources and betatrons were used for irradiation and as a milestone in radiation therapy history replaced by the medical LINAC between 1960 and 1980. With operation at energies between 6-20 MV, tumors deep inside the patient could be gradually treated with higher precision and higher doses. CT based planning (2D on one single CT slice) has been introduced at the end of the 1970s and replaced the traditional way of 2D treatment planning with radiographic images and custom-made blocks for blocking out parts of the rectangular-shaped beam. 3D computerized CT-based treatment planning that uses LINACs is nowadays a standard procedure in every modern radiation therapy department. Using the MLC, the rotating gantry, collimator, and table as additional degrees of freedom, 3D treatment plans can be applied to the PTV with high precision. 3D-CRT is the process of *forward planning*, meaning that beam directions, field shapes and individual dose are designed manually and adjusted if clinical goals are not fulfilled.

4.2.3 Intensity Modulated Radiation Therapy Techniques

In contrast to forward planning approaches such as 3D-CRT, *inverse planning* is used widely nowadays. Here, the machine parameters like beam shape and the desired fluence (or *intensity*) per beam or field is not determined beforehand, but predefined treatment plan goals, or so-called *objectives* are used as an input for a TPS in order for the TPS to automatically optimize a treatment plan fulfilling the given objectives. The goal of radiation therapy plan optimization is the calculation of the LINAC parameters (e.g. beam angles, shapes, or intensities) that fulfill the most criteria given as an input by the TPS, which can be defined as the combination of the objective function and "constraints". While a constraint requires certain criteria to stay within predefined limits, if the criteria are defined as an objective function (or parts of it), the maximization or minimization is desired [10]. The fluence modulation can be achieved in various ways in terms of dynamics: A static approach is the pre-definition of certain gantry angles and a fluence modulation from each gantry angle using the LINAC's MLC. Each beam is decomposed into small segments and the configuration of the MLC is changed after the irradiation of each segment. Therefore, this technique is called "step-and-shoot" IMRT. In addition, the pause (or step) between each segment can be left out, leading to a dynamic technique with still pre-defined gantry angles but a dynamical movement of the MLC with constant or variable dose rate (*dynamic multileaf collimator (DMLC)*). The next step for dynamic (and therefore faster) dose delivery was the implementation of a moving gantry, rotating with variable gantry speed, variable dose rate, and a dynamically moving MLC, called volumetric modulated arc therapy (VMAT). In general, intensity modulated techniques have the advantage of similar or better dose coverage and better conformality for various PTV forms, with less dose applied to the OARs in contrast to 3D-CRT. This can be seen in an example in figure 4.7.

4.2.4 Biological Effects of Dose and Fractionation

The ionizing radiation applied during radiation therapy leads to cell DNA damage (as briefly described in chapter 3). The relationship of absorbed dose and the fraction of surviving cells can be described using models for cell survival. The often used linear quadratic (LQ) model for the description of cell survival assumes two parameters as components of cell kill: α, the parameter describing the initial cell survival curve slope (linked to single interactions, such as mutations of genes vital to cell survival) and β describing the quadratic component of cell killing (caused by two double strand breaks in one DNA strand). $S(D)$ as the fraction of cells surviving a dose D (applied in one single exposure) can be described as:

$$S(D) = e^{-\alpha D - \beta D^2} \tag{4.4}$$

The ratio α/β describes the dose at which both linear and quadratic components of cell killing are equal. Each cell type is affected by the same absorbed dose differently, which
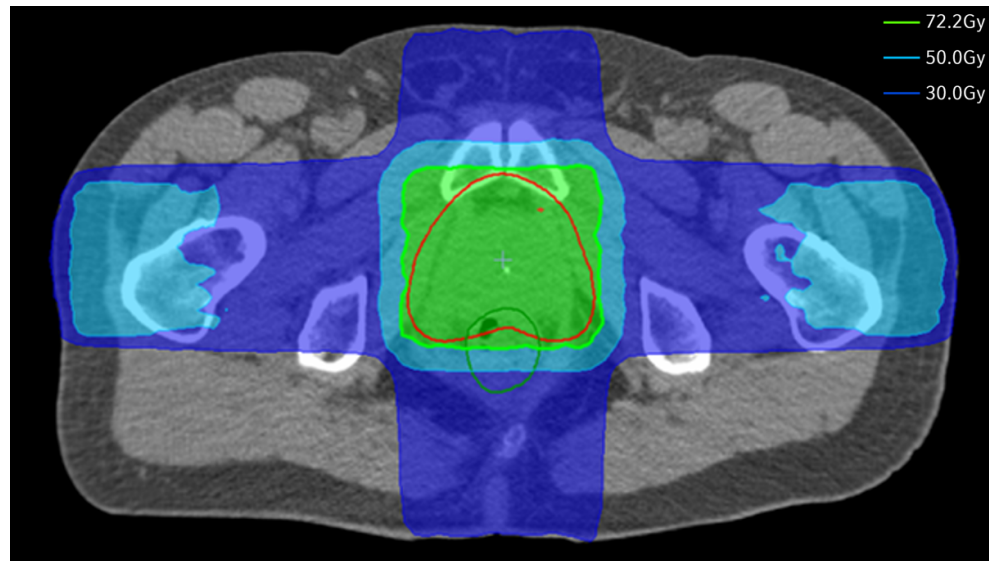
(a) 3D-CRT
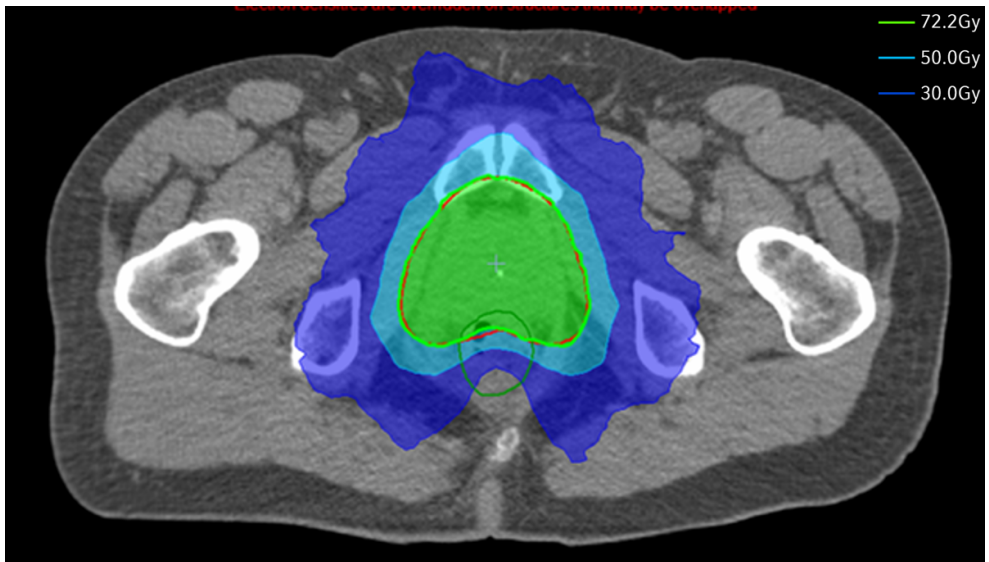
(b) VMAT

Figure 4.7: Comparison of a 3D-CRT (a) and a VMAT (b) treatment plan for the same target volume (red contour). The 95 % isodose line (green) is covering the PTV (red) in both cases, but with much higher conformality and lower dose applied to surrounding tissue when using intensity modulated techniques.

can be referred to as the *radiosensitivity* of cells and tissue [49, 55].

The concept of applying dose in two or more parts over a period of days or weeks rather than in one single session is called *fractionation*. A larger amount of dose must be applied

to the patient to achieve the same biological effect, as sub-lethal radiation damages are repaired during the breaks between the fractions. Cells with a low α/β ratio need more total dose in a fractionated scheme to result in the same cell survival rate [10, 55]. The biologically effective dose (BED) for the fractionation scheme can be defined using the equal dose d of n fractions:

$$BED = nd(1 + \frac{d}{\alpha/\beta}) \tag{4.5}$$

Different schemes of fractionation with the same BED are considered *isoeffective*. The effectiveness of fractionated radiation therapy is dependent of the α/β ratio. The main goal of fractionation is a maximization of cell kill in the tumor in combination with maximal sparing of dose to normal tissue [10, 55].

Hypofractionation

Standard fractionation is based on one daily treatment five times a week with doses of $1.8\,Gy$ to $2.0\,Gy$. For fraction doses above $2.0\,Gy$, the number of fractions has to be reduced in order to achieve the same BED. This is called *hypofractionation*. If the α/β ratio for the tumor is smaller than for late reactions in normal tissue, a higher fraction dose leads to less repair in the tumor compared to normal tissue. With increased tissue sparing due to modern treatment techniques like IMRT or VMAT (see section 4.2.3) or with the introduction of image guided radiation therapy (IGRT) (see section 4.4), hypofractionated concepts gain attractiveness for more possible treatment sites even with slightly higher α/β ratios [10, 55].

4.3   Dose Calculation Algorithms

For both forward and inverse planning different algorithms for dose calculation are available in commercial TPS. Accurate and fast 3D dose calculations link the chosen treatment parameters and the clinical outcome of the treatment technique. The calculated distribution of the absorbed dose is the primary physical quantity for analyzing the clinical effects of the treatment strategy. Speed and sufficient accuracy are the mutually conflicting goals of dose calculation algorithms [10]. Dose calculation algorithms can be divided into two different groups: *kernel based superposition* or *convolution* methods, such as *pencil beam (PB)* or *collapsed cone (CC)*, which use a specific model for dose calculation, and direct approaches, such as *Monte Carlo (MC)* solvers.

4.3.1   Kernel-Based Superposition/Convolution Methods

Certain approximations or *models* have to be implemented in order to increase the speed a of dose calculation algorithm. All model-based algorithms describe the physical process of energy deposition by the radiation field only to some extent. At first, the treatment machine has to be modeled, which is typically accomplished using a model for photon *primary energy fluence* with the energy spectrum and the measured beam properties of the LINAC. This model can be used as an input for all calculations of energy absorption and transport in the patient tissue. The absorption of primary photons is expressed by the term <u>t</u>otal <u>e</u>nergy <u>r</u>eleased per unit <u>ma</u>ss (TERMA) $T(\vec{r})$ released by a radiation field interacting with a medium (of density ρ) at a certain point $\vec{r}$, with μ denoting the linear photon absorption coefficient [7, 10]:

$$T(\vec{r}) = \frac{\mu}{\rho}(\vec{r})\Psi(\vec{r}) \tag{4.6}$$

Specific *dose kernels* model the energy transport via secondary photons and electrons [10]:

- **Pencil Beam (PB)** The PB algorithm is the simplest and therefore the fastest method of dose calculation. The PB kernel is the integration of all point-spread functions (the energy spread around a single primary unscattered photon interaction) along an infinite ray of photons [43]. The accuracy of PB algorithms is limited in inhomogeneous tissue with large density variation such as in the lung [66]. Also, secondary photon and electron interactions which occur in any other direction than the incident beam angle are discarded by the PB algorithm, because all matter in the lateral direction of the beam is assumed to be water.

- **Collapsed Cone (CC)** A more accurate and sophisticated algorithm, especially for inhomogeneous media, is the CC algorithm, where single process lateral scattering and backscattering are accounted for to some extent. Here, angular discretization of the kernel into cones increases the efficiency of the calculation of energy transport and deposition [5, 6]. The angular discretized kernel is convolved with the TERMA

distribution, which leads to an energy deposition into the voxels in the cone direction of the central cone axis. The accuracy can be increased using a finer angular discretization.

4.3.2 Monte Carlo (MC) Approach

A direct method without the usage of model approximations is the MC algorithm widely established as a statistical method for performing numerical integrations. Before absorption, photons have a limited number of possible interactions, which can be simulated directly. MC methods are older than 200 years and can be used to solve mathematical problems, for example the numerical integration of functions using random numbers. The function value for a random number multiplied by the length of an integral provides a first and rough estimate of the real integral. If a large number of random numbers is sampled, the area of the corresponding rectangles and the mean of the areas is calculated. In the limit of infinite random number samples, this mean values converges to the real integral. The importance for this algorithm, which is less efficient than other algorithms for one dimensional algorithms, becomes imminent in high-dimensional problems like the dose distribution in a patient caused by ionizing radiation [10]. MC is considered the primary benchmark method for faster dose calculation algorithms [6] and is also nowadays widely used in clinical routine because of reduced processing times due to adapted algorithms for radiation therapy and much faster and more affordable computer processors. The MC dose calculation algorithm simulates the stochastic processes of primary and secondary photon and secondary electron interaction until the particle and all secondary particles are absorbed. Some approximations (e.g. "condensed history" techniques) simplify the number of interactions for secondary electrons along the path through the patient using the assumption, that medium is locally homogenous [6, 10].

Dose-to-water vs. Dose-to-medium

Kernel-based dose calculation methods report the absorbed dose-to-water with different electron densities, as the machine parameters used as input data for a standard conventional TPS are generally measured in water phantoms. The assumption of the human body consisting solely of water is obviously not correct, although it is a good approximation. The conversion between dose-to-medium and dose-to-water can be carried out by applying Bragg-Gray cavity theory. With the introduction of the MC approach, the energy deposition is directly calculated in the medium and the dose-to-medium is reported directly. Differences up to 11% can be found when converting doses-to-water from doses-to-media, depending on the type of medium and especially for voxels containing mixed types such as air, bone, and soft tissue [38].

4.4   Image Guided Radiation Therapy

Patient positioning is nowadays accomplished using imaging data acquired at the LINAC, shortly before or even during treatment, in order to ensure either a well-positioned patient or the correct position of the PTV (the so-called target centered approach). The process of patient surveillance using 2D, 3D, or even 4D imaging techniques is called *IGRT* [27, 68] and leads to significant reductions in PTV treatment margins and therefore to a reduction of the dose to nearby OARs [21]. The simplest method is the usage of an electronic portal imaging device (EPID), where the 2D projection of the LINAC beam is recorded using digital imaging devices, such as amorphous silicon flat panel detectors and (less frequently used) liquid ion chambers. The rather bone-based image with low soft tissue contrast due to the dominant Compton effect (see 3.2.4) in the MV range is compared to a digitally reconstructed radiograph (DRR), which is a 2D X-ray simulated by the TPS. As in some cases the patient's bony structures or the central lung distance (CLD) provide enough information for positioning, this technique is still in use clinically nowadays.
When the 2D and low contrast EPID imaging is not sufficient, multiple 3D options remain: The most widely used one is the so-called cone-beam computed tomography (CBCT). The usage of CBCT in radiation therapy was first described in 2000 as an adaption from its applications in dentistry [26]. An in-room independent X-ray source and an opposing corresponding 2D digital detector panel are mounted to the LINAC. From a set of several 2D projections obtained through rotation of source and detector around the patient, a 3D reconstruction of the patient's anatomy can be obtained with higher, but not identical properties as a fan-beam CT, such as high spatial resolution and better soft tissue contrast than megavolt (MV) images, but with less reliable HU values than the planning CT. The 3D reconstruction can be registered to the patient's planning CT, allowing for precise patient positioning according to the daily anatomy.

In addition, the usage of MRI, tracking of implanted fiducial radiopaque markers, tumor tracking with implanted transponders (Calypso®, [70]), stereoscopic in-room X-ray imaging, or ultrasound tracking devices are already implemented clinically for IGRT in multiple dimensions and also with regards to time and should be therefore mentioned.

4.4.1   Stereotactic Body Radiation Therapy

Stereotactic Body Radiation Therapy (SBRT) is defined as a method of radiation therapy, which accurately delivers a high radiation dose in only one or few fractions (*hypofractionated*, see section 4.2.4) to an extracranial target volume. SBRT can be performed with a traditional LINAC with IGRT technology, a LINAC specifically adapted for the usage of SBRT, or also dedicated delivery systems. A systematically optimized SBRT workflow has to be established and specialized quality assurance (QA) methods have to be developed for an adequate irradiation delivery. One important procedure in the workflow is the possibility of accurate tumor localization with site specific imaging modalities. For early

stage medically inoperable stage I NSCLC, SBRT is shown to perform superior compared to conventional radiation therapy and is nowadays considered the standard of care for medically inoperable patients [23]. The dose to the PTV is usually prescribed to the 65 % or 80 % isodose line for a steep dose gradient outside of the PTV without the necessity of homogeneous dose distributions inside the PTV. An example of a dose distribution for SBRT can be found in figure 4.8(b).

(a) An axial (left), coronal (middle), and sagittal CT slice of a patient treated with SBRT with the target volumes delineated (red: PTV; purple: ITV, dark red: GTV in maximum inhale and maximum exhale, yellow: GTV delineated from the 3D planning CT.
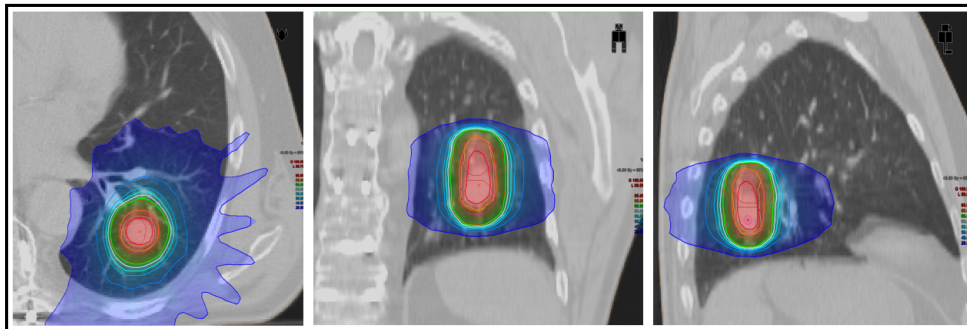
(b) The corresponding dose gradients to the PTV. The dose to the PTV was 40.5 Gy prescribed to the 65 % isodose line (bright green).

Figure 4.8: An exemplary SBRT treatment plan in all three CT imaging planes.

Chapter 5

Uncertainties in Lung Radiation Therapy and Advanced Methods for Uncertainty Mitigation

In lung radiation therapy, various sources of uncertainties exist and have to be accounted for, especially when treating the patient with only few fractions using the SBRT treatment technique. The first section of the following chapter gives an overview of geometrical uncertainties in the treatment planning process, and errors and uncertainties, which arise during treatment within one fraction (*intrafractional*) or between multiple fractions (*interfractional*). When treating sites in the upper abdomen or thorax, tumor breathing motion is one of the major challenges. The second section of the chapter describes different strategies for breathing motion management, including the process of *four-dimensional (4D) treatment planning*.

5.1 Geometrical Uncertainties

Geometric uncertainties arise from multiple sources: patient set-up variation, organ motion and deformation, and machine related errors [25]. Machine-related geometrical errors, such as isocentric deviations between gantry, collimator, LINAC table and the imaging system, or deviations in beam shapes and sizes due to MLC uncertainties, are considered relatively small in comparison to daily set-up variations or organ motion [63]. With adequate QA procedures, the magnitude of machine-related geometrical errors can be reduced to a minimum. The safety margin from the GTV to the PTV accounts for geometrical errors. The GTV delineation process itself is also prone to uncertainties, for example the limited resolution of imaging modalities leading to a partial volume effect, intraobserver variations, interpretation differences between observers or imaging modalities, or unclear delineation guidelines [65].

5.1.1   Intrafractional & Stationary Interfractional Patient Set-Up Variations

The positioning of the patient and far more importantly the positioning of the PTV in modern SBRT treatments using IGRT methods were described in section 4.4. IGRT methods account for interfractional setup errors by using for example daily CBCT corrections for lung SBRT, careful immobilization, or well-designed setup protocols [65]. These setup errors have random and systematic components. *Intrafractional* variations in lung radiotherapy are target uncertainties, which are due to breathing motion (on a timescale of seconds) or the variability in the breathing pattern, or a baseline drift in breathing motion (on a timescale of minutes). Breathing motion will be discussed in the next section. Baseline drifts or breathing pattern variability can be accounted for using additional margins or image guidance and direct tumor motion monitoring during the radiotherapy fraction, as it is already in practice using the CyberKnife® system (Accuray Inc., Sunnyvale, United States) [4, 45, 50, 61]. A reduction of treatment time also reduces the variability using techniques like VMAT or the so-called flattening filter free (FFF) technique, where the flattening filter in the LINAC treatment head is retained from the beam for higher dose rates.

Interfractional uncertainties include the rigid patient setup accuracy and inter-day baseline variability with respect to the bony structures on a timescale of days. Daily patient positioning with target based IGRT can account for most of these potential errors. If the target-based IGRT is conduced rigorously well in clinical practice, the interfractional component of the safety margin can be reduced to almost zero. Anatomical deviations, such as tumor shrinkage or atelectasis, also bear the risk of increased errors and the treatment plan should be adapted accordingly.

5.1.2   Respiratory Organ Motion

Respiration-induced organ motion is considered the largest intrafractional organ motion compared to intrafractional motion caused by the skeletal muscular, cardiac, and gastrointestinal systems. Respiratory motion is highly patient-specific and not rhythmic, unlike cardiac motion. The amount of lung tumor motion during breathing varies widely, mostly in the superior-inferior (SI) direction with typical amplitudes of $\sim 10\,\mathrm{mm}$ (for some patients up to over $\sim 30\,\mathrm{mm}$) and also with (smaller) possible components anterior-posterior (AP) and right-left (RL) [40, 60, 62]. An example of possible lung tumor motion is depicted in figure 5.1. No general patterns nor assumptions on the patient-specific respiratory motion can be assessed prior to CT acquisition and treatment. Breathing motion has many individual characteristics such as quiet versus deep, chest versus abdominal, or healthy versus compromised [31].

The problems of respiratory organ and tumor motion during radiation therapy arise during image acquisition, treatment planning, and radiation delivery: motion artefacts compromise the acquisition of all imaging modalities such as the static CT used for tumor
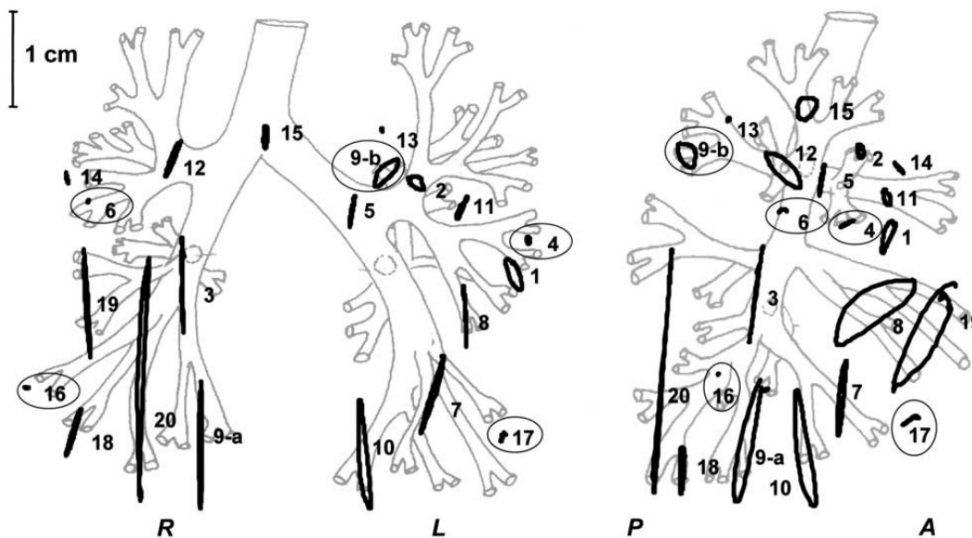
Figure 5.1: Orthogonal projections of the trajectories of lung tumors in the coronal (left) and sagittal (right) plane [60].

delineation and dose calculation. Typical for thoracic 3DCT images is a blurring or arte-facts in the region of the diaphragm. Using 4DCT datasets, respiratory motion artefacts are largely reduced but the image quality of the reconstructed 4DCT dataset also has an influence on the delineated GTV structures in each breathing phase and on dose calcu-lation on the dataset due to differences in the medium density and therefore also in the resulting dose. A method of improving 4DCT reconstructions with respect to the quality of delineation is introduced in chapter 6. During treatment planning, tumor respiratory motion is accounted for using the ITV delineation approach, as discussed in section 4.2.1. During the radiation delivery itself, intrafractional respiratory tumor motion can cause averaging or blurring of the static dose distribution along the path of motion, leading to anatomical deviations in intended and actually delivered dose distributions [31]. Figure 5.2 shows possible deviations between two respiratory phases for an exemplary patient.

Additional challenges for high-dose lung radiation therapy is the handling of low density tissue inside the PTV surrounding the higher density tumor to be irradiated: the higher density tissue absorbs more dose than low density lung tissue or air surrounding the tumor. The PTV is simply a virtual, non-anatomical planning volume according to the ICRU def-inition [24, 25]. The low density of lung tissue surrounding the tumor is an issue in the comparison of planned PTV dose and the actual dose to the tumor.

For modulated treatments such as IMRT and VMAT, the interplay effect is also a possible source of uncertainties caused by dynamic respiratory motion in addition with moving el-ements of the LINAC. The LINAC components also "move" intrafractionally, for example the leaf movement in DMLC or VMAT techniques for small segments of the treatment plan, or even the movement of the leafs with a static gantry in step-and-shoot IMRT treat-ment plans. If the irradiation segment does cover the tumor at that time, because of some

segments applying dose to only parts of the PTV or the ITV at some timepoints due to tumor motion out of the irradiation field, less dose is irradiated on the tumor and the desired planned dose distribution is compromised.
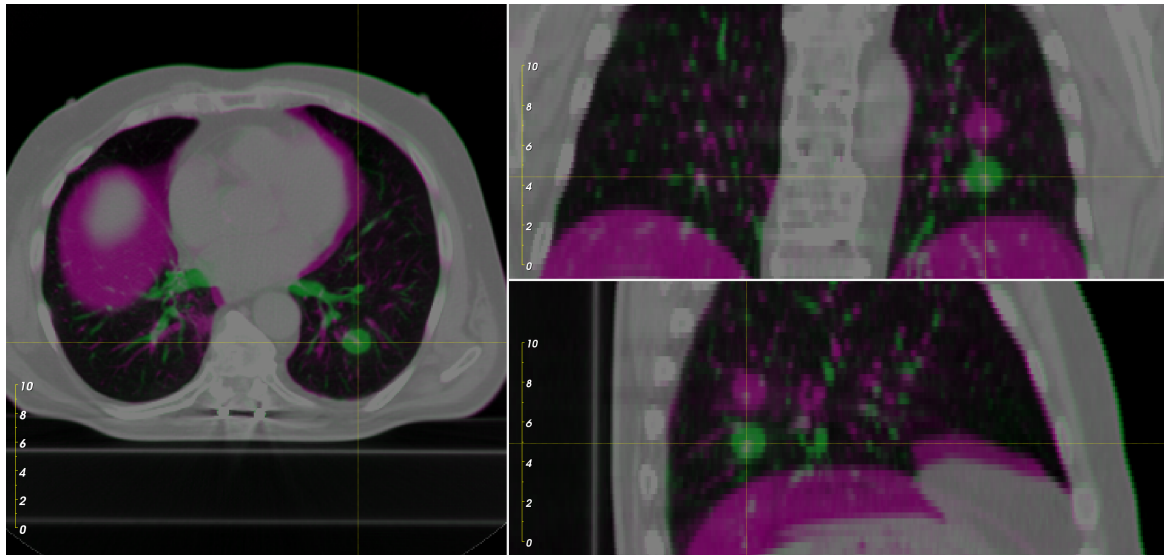
Figure 5.2: Example of possible deviations in tumor position between different respiratory phases: maximum inhalation (green) and maximum exhalation (purple) breathing phase. A tumor motion of about 27 mm in CC direction has been measured for this patient.

5.2 Advanced Methods for Uncertainty Mitigation in the Presence of Respiratory Motion

In radiation therapy, all known possible uncertainties have to be accounted for. The easiest way for the compensation of respiratory motion would be the increase of the treatment margin, but this approach would also increase the volume of healthy tissue exposed to high doses. As more healthy tissue is irradiated, the probability of treatment-related complications increases. An expanded PTV also limits the possibilities of delivering a high and adequate dose to the target itself [29]. If the treatment margin is not increased, respiratory motion can be accounted for using different techniques described in the following section: motion-encompassing methods, respiratory gated techniques, breath-hold techniques, forced shallow-breathing methods, and the respiration-synchronized technique [31].

5.2.1 Management of Breathing Motion in Radiation Therapy

Motion-Encompassing Methods

For treatment planning, tumor respiratory motion can be encompassed using different CT imaging techniques to include the full tumor motion range at the time of CT acquisition. One method is slow CT scanning, where the CT couch is moving very slowly through the CT gantry with or without an averaging of multiple CT scans during the acquisition time. This results in a tumor-encompassing volume in high contrast areas with the full extent of respiratory motion, but leads to motion blurring which could induce large observer errors in tumor and normal tissue delineation. Also, two gated or breath-hold CT datasets can be recorded, one at maximum inhalation and another at maximum exhalation. The blurring effect is reduced significantly, but the exhalation scan tends to underestimate lung volume and therefore overestimates the percentage of irradiated lung tissue with high doses. As mentioned in chapter 4.1.2, the acquisition of 4DCT scans is considered the standard for obtaining high quality CT datasets in the presence of respiratory motion. The multiple 4DCT phases (or also the maximum exhalation and inhalation CT scans) can be used for the creation of average intensity projection (AIP) (a CT dataset with the average CT number found in a given voxel in the dataset [19], see figure 5.3(a)) and maximum intensity projection (MIP) (a CT dataset with the maximum CT number found in a given voxel in the dataset [64], see figure 5.3(b)) reconstructions. In addition, a mid-ventilation scan [72] can be derived from a 4DCT scan, with the time-averaged tumor position.
All of the above mentioned techniques help to improve the delineation process of the GTV in multiple respiratory phases and increase the quality of the target volumes. The treatment margin is now encompassing the full tumor motion range using the ITV approach. However, different strategies for PTV margin reduction exist and the previously described methods do not account for the inter- and intrafractional tumor motion variability. More details on respiratory motion management in radiation therapy can be found in [31].
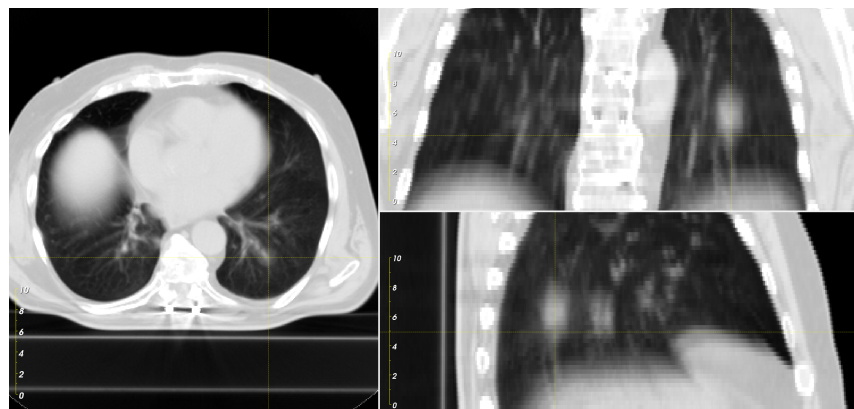
(a) AIP
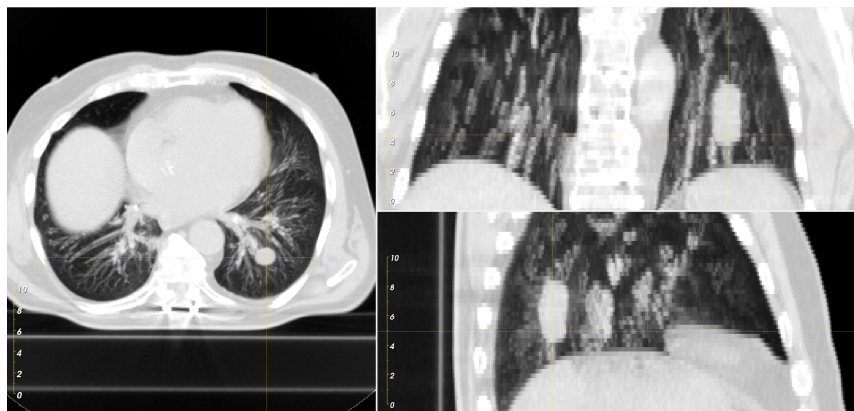
(b) MIP

Figure 5.3: Example of AIP (a) and MIP (b) dataset derived from a 4DCT dataset (left: axial; right top: coronal; right bottom: sagittal). The motion range is encompassed in both methods with the average CT number for AIP reconstructions and the maximum CT number for MIP reconstructions.

Free-Breathing Respiratory Gated Techniques

One technique for the reduction of the PTV size is the application of dose only during a specific portion of the patient's respiratory cycle. This can include multiple breathing phases and is referred to as **gate**. The size and therefore the duration of the specific gate can be determined and monitored using external (or internal) respiratory motion surrogate signals or implanted radiopaque fiducial markers. Gating can be delivered using either the displacement of the breathing curve (*displacement gating*) or the respiratory phase information (*phase gating*), similar to amplitude-based and phase-based 4DCT acquisition, respectively (see section 4.1.2). External respiratory motion surrogates include optical surface scanning (see section 4.1.3) or optical tracking of infrared markers placed on the patient surface. Using spirometry, the lung volume can also be used as an "internal"

motion surrogate. The limitations of surrogates are obvious: relying on an external motion surrogate does not necessarily give adequate information on the internal actual tumor movement due to various factors, such as baseline drifts and the patient-specific breathing variability [31].

Ideally, either real time tracking of implanted fiducial markers or the tumor itself using image guidance for a synchronization of the tumor location with a specifically prepared 4D treatment plan would be necessary also for gated delivery, with or without the use of online predictive respiratory motion monitoring. The dose from the 4D plan intended for a certain breathing phase could be delivered based on the actual motion state [53]. The LINAC beam-on and beam-off latency is one of the most crucial factors in implementing gated treatment methods. In chapter 8, the possibilities and drawbacks of gated delivery are assessed in terms of latency and dosimetrical aspects, as part of this thesis.

Breath-Hold Techniques

The patient breath-hold reduces the dynamic component of breathing motion. Again, a respiratory motion surrogate is used to determine the tumor location and the LINAC is gated to that exact point. The same limitations as for standard gated treatments in free-breathing apply, but keeping a stable breath-hold condition over a longer period of irradiation time makes a reduction of potential risks possible. The technique is used in lung cancer radiotherapy with motion surrogates, such as spirometry, infrared markers placed on the patient's surface, or optical surface scanning. The method is nowadays also more widely used in breast radiotherapy, where the deep breath-hold increases lung volume. With the caudal movement of the diaphragm, the heart as a crucial OAR is moved out of the radiation field [58]. The level of inspiration differs in different techniques: reproducible breath-hold states can be accomplished in DIBH (the maximum possible inspiration), a pre-defined respiration state, which is not the absolute maximum, or voluntary breath-hold [31].
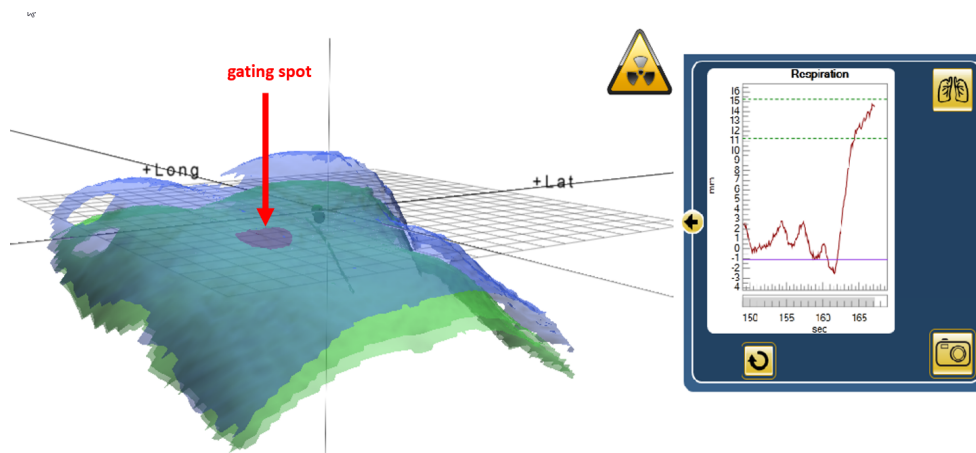
Figure 5.4: An example of the DIBH gating technique for breast patients. Green: patient surface during free-breathing; blue: patient surface during DIBH. The red spot on the surface indicates the measured gating spot. On the right side, the patient breathing curve is displayed in red and the gating window can be seen in green (dashed).

Forced Shallow-Breathing Methods

Another possibility of reducing the PTV margin is forced shallow breathing (FSB) using abdominal compression. A plate attached to a stereotactic body frame is used to apply pressure to the patient's abdomen, reducing diaphragmatic excursions. This technique is mostly used in the treatment of liver, kidney, pancreatic or early stage lung tumors. Tumor motion amplitude reductions from 8-20 mm (12.3 mm mean) to 2-11 mm (7.0 mm mean) have been reported using abdominal compression [44]. Figure 5.5 shows an exemplary sagittal CT slice of a patient treated with abdominal compression.

Respiration-Synchronized Technique

The *respiration-synchronized technique*, more commonly known as *real time tumor tracking*, is a method where the radiation beam follows the exact tumor path during the whole treatment fraction. Ideally, respiratory motion margins can be eliminated using this technique, but several technical difficulties are still present. The position of the tumor has to be monitored constantly and in real time, the tumor position has to be estimated in a predictive manner with high precision, the beam has to be dynamically positioned accordingly, and the dosimetry of the changing lung volume has to be accounted for adaptively [31]. Various algorithms for motion modeling and prediction already exist and are partially used in distinct radiation therapy systems to compensate for tumor motion [41].
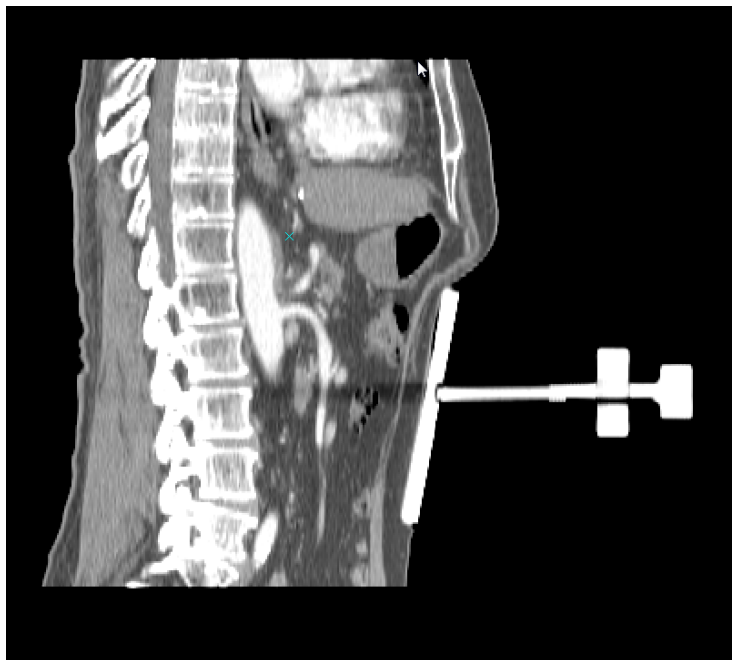
Figure 5.5: Sagittal CT slice of a lung cancer patient treated with abdominal compression for the restriction of the tumor motion amplitude.

5.2.2 Four-dimensional Treatment Planning

4D treatment planning uses more than one 3D image dataset for the evaluation of the dose to moving targets and OAR structures. Either a full 4DCT dataset with typically 8-10 respiratory phases is used for treatment planning, or synthetic datasets generated from the 4DCT (such as AIP, MIP, or mid-ventilation scans, see section 5.2.1) provide the information of the patient anatomy and therefore the CT electron density at a certain timepoint. Including the temporal dimension in the treatment planning process allows to compensate for the high patient-specific breathing variability. Each dataset is used for planning, similar to the 3D treatment planning approach, which leads to an optimal plan for the breathing-induced changes in the anatomy. The individual doses in each sampled timepoint are subsequently merged to result in a dynamic patient model. This is referred to as *4D dose accumulation, dose mapping*, or *dose reconstruction*. Deformable image registration [14] methods provide a non-rigid body voxel congruity between all volumetric CT datasets and is used for dose mapping. The dose distribution on each secondary dataset is accumulated and scored back on a reference dataset for evaluation. The whole workflow of dose accumulation to a single dataset is potentially prone to multiple error sources, such as artifacts in the 4DCT datasets, errors in the deformable registration process which could induce errors in dose mapping, or certain limitations of the dose mapping algorithms in regions with strong density variation. Different methodologies for 4D treatment planning can be found in Rosu et al. [53]. As part of this thesis, an approach for 4D Monte Carlo dose calculation on different image dataset has been implemented in chapter 7.

Chapter 6

Paper 1: Comparison of Different Image Binning Algorithms for 4DCT Reconstruction for Radiation Therapy

Publication: **Comparison of different image binning algorithms for 4DCT reconstruction for radiation therapy** [1]

ORIGINAL PAPER

Clinical workflow optimization to improve 4DCT reconstruction for Toshiba Aquilion CT scanners

Philipp Freislederer [1,*], **Christian Heinz** [1], **Henrike von Zimmermann** [1], **Sabine Gerum** [1], **Falk Roeder** [1], **Michael Reiner** [1], **Matthias Söhn** [1], **Claus Belka** [1,3,4], **Katia Parodi** [2]

[1] Department of Radiation Oncology, University Hospital, LMU Munich, D-81377 Munich, Germany
[2] Department of Experimental Physics – Medical Physics, LMU Munich, D-85748 Munich, Germany
[3] German Cancer Consortium (DKTK), Munich, Germany
[4] Comprehensive Pneumology Center Munich (CPC-M), Member of the German Center for Lung Research (DZL), Germany

Abstract

Respiratory motion remains a source of major uncertainties in radiotherapy. Respiratory correlated computed tomography (referred to as 4DCT) serves as one way of reducing breathing artifacts in 3D-CTs and allows the investigation of tumor motion over time. The quality of the 4DCT images depends on the data acquisition scheme, which in turn is dependent on the vendor. Specifically, the only way Toshiba Aquilion LB CT scanners can reconstruct 4DCTs is a cycle-based reconstruction using triggers provided by an external surrogate signal. The accuracy is strongly dependent on the method of trigger generation. Two consecutive triggers are used to define a breathing cycle which is divided into respiratory phases of equal duration. The goal of this study is to identify if there are advantages in the usage of local-amplitude based sorting (LAS) of the respiration motion states, in order to reduce image artifacts and improve 4DCT quality. Furthermore, this study addresses the generation and optimization of a clinical workflow using as surrogate motion monitoring system the Sentinel[TM] (C-RAD AB, Sweden) optical surface scanner in combination with a Toshiba Aquilion LB CT scanner. For that purpose, a phantom study using 10 different breathing waveforms and a retrospective patient study using the 4DCT reconstructions of 10 different patients has been conducted. The error in tumor volume has been reduced from $2.9 \pm 3.7\%$ to $2.7 \pm 2.6\%$ using optimal cycle-based triggers (manipulated CBS) and to $2.7 \pm 2.2\%$ using LAS in the phantom study. Moreover, it was possible to decrease the tumor volume variability from $5.0 \pm 3.6\%$ using the original cycle-based triggers (original CBS) to $3.5 \pm 2.5\%$ using the optimal triggers and to $3.7 \pm 2.7\%$ using LAS in the patient data analysis. We therefore propose the usage of the manipulated CBS, also with regard to an accurate and safe clinical workflow.

Keywords: 4DCT, Local amplitude-based sorting, Radiotherapy, Optical laser surface scanner, Respiratory motion monitoring

1 Introduction

In radiation therapy considerable uncertainties in treatment planning of thoracic and upper abdominal sites still remain due to respiratory motion [1]. An increase in treatment margins does account for these motions, but increases the dose to normal tissue [2]. Besides challenging correct treatment delivery, motion of anatomical structures also often deteriorates the image quality of computed tomography (CT) in these treatment regions [3], which later on are being used for treatment planning. Four-dimensional computed tomography (4DCT), also referred to as respiratory-correlated

---

computed tomography (RCCT), can be used to reduce breathing induced motion artifacts which can occur in a "static" CT and allows the detailed investigation of tumor movement with regards to time [4,3,5–7]. Concerning the time-resolution, a certain type of surrogate signal is always needed to sort the acquired oversampled CT raw dataset into multiple datasets, so-called 4DCT phases. Respiratory monitoring systems are required to provide accurate surrogate breathing signals in order to acquire any 4DCT. For Toshiba Aquilion CT scanners, these signals need to be provided as cycle based *online* trigger pulses, each indicating a new breathing cycle. A major problem in providing these prospective trigger pulses is that one has to be certain that each trigger represents the same breathing phase, for example the so-called 0% phase at maximum inhalation. Also, if the CT reconstruction algorithm equally divides the phases in between two trigger pulses, errors in reconstruction cannot be neglected as respiratory motion suffers from irregularities [2,8].

The goal of this study was to generate and optimize a clinical workflow using the Sentinel^{TM} (C-RAD AB, Stockholm, Sweden) optical surface scanner as a surrogate motion monitoring system in combination with a Toshiba Aquilion CT scanner. Also, we investigated the variations of image quality in two different image sorting algorithms: Cycle-based sorting (CBS) and local amplitude-based sorting (LAS) based on a phantom study using 10 different breathing waveforms and a patient study using the 4DCT reconstructions of 10 different subjects.

2 Methods and materials

For the phantom evaluation, 4DCT datasets of a Dynamic Thorax Phantom (CIRS Inc., Norfolk, VA, USA), each with a different breathing curve, were acquired using a Toshiba Aquilion 16 Large Bore CT scanner with the AquilionLB Software Ver3.38ER005 (Toshiba Medical Systems Corporation, Otawara, Japan). The motion signal was recorded using the Sentinel^{TM} optical laser-based surface scanner [9]. As the Sentinel^{TM} is recording the breathing signal via laser on a certain, user-defined spot on the patient's surface, the phantom had to be extended using thermoplastic mask material to simulate a patient's upper body visible to the scanner. This thermoplastic mask is attached to the surrogate motion motor of the CIRS phantom and is used to simulate a breathing motion of a phantom thorax. All 4DCTs for the phantom measurements were acquired and reconstructed with following parameters: slice collimation of 16×1.0 mm, helical pitch of 1.2, rotation time of 0.5 s, matrix of 512×512, tube voltage of 120 kV and tube current of 150 mA. Images were finally reconstructed in 1 mm slices and a pixel size of 1.074 mm. For the phantom study, an acrylonitrile butadiene styrene (ABS) copolymer sculpture (LEGO®, Billund, Denmark) served as a "tumor" in the lung phantom. This special structure has been

Table 1
Overview of the breathing motion characteristics for the patient data evaluation. Tumor motion has been measured using an in-house developed software tool and is not evaluated specifically here. In patients 4 and 7, two different tumor sites have been investigated.

	Mean respiratory rate/bpm	Surrogate motion range/mm	Baseline drift/%	Tumor movement/mm		
				CC	AP	RL
Pat 1	11.9	17.8	5.0	15	5	1
Pat 2	13.0	3.3	3.3	6	3	2
Pat 3	17.8	9.3	1.3	9	3	3
Pat 4(1)	16.4	8.3	0.4	6	3	3
Pat 4(2)	,,	,,	,,	5	5	3
Pat 5	19.4	9.2	0.1	9	2	1
Pat 6	15.3	9.3	33.7	3	2	2
Pat 7(1)	11.1	19.9	1.6	3	1	1
Pat 7(2)	,,	,,	,,	12	4	1
Pat 8	12.8	5.3	10.9	6	6	3
Pat 9	11.0	6.8	−1.7	6	3	2
Pat 10	19.0	8.8	1.5	15	3	1

used because of its distinct edges and multiple spikes and corners. If the CT image quality is to be determined, these structures serve as a valid measure if they are visible in the reconstruction.

For the patient data evaluation, the 4DCTs of 10 consecutive patients (3 males, 7 females, age between 34 and 84 years (mean age 70.5 years)) treated in clinical routine for pulmonary metastases ($n = 6$) and non-small cell lung cancer (NSCLC) ($n = 4$) were selected for the retrospective analysis. All patients were treated with hypo-fractionated stereotactic body radiotherapy (SBRT) and therefore received 4DCTs as it is standard clinical practice at our institution. Patient breathing waveform characteristics can be found in Table 1. Baseline drift has been calculated according to [3] and is depicted as a percentage of the normalized mean amplitude for each patient. All 4DCTs were reconstructed in 3 mm slices due to the clinical protocol. The respiratory monitoring evaluation point of the laser surface scanner has always been placed in the region of the diaphragm of the patient on the patient's right side. This point on the patient's surface has been chosen according to [10] as it is expected to provide the least interferences with cardiac movement, less phase shift than a spot lower in the abdomen of the patient, and a better signal-to-noise ration (SNR) than any other point on the patient's thorax due to a higher amplitude.

All patients gave written informed consent to data collection prior to treatment. The study was in accordance with the declaration of Helsinki (latest version) and has been approved by the independent ethics committee of the University of Munich (573-15, issued on October 10th, 2015).

2.1 Data acquisition and 4DCT data sorting

RCCTs were acquired in helical mode while the breathing waveform was recorded by the Sentinel[TM] scanner. This surface scanner uses a threshold method to try to determine the maximum of the breathing curve which is then sent to the CT as a trigger pulse. The position of this threshold is crucial for the CT scan quality: To obtain trigger pulses at the maximum inhale phase (and therefore always at the same distinct phase during the course of the CT) the threshold has to be set as high as possible with regards to the breathing waveform. Due to baseline drifts, breathing irregularities, and even bending of the CT couch during the acquisition time of the CT scan [10], there will be a risk of missing triggers when setting the threshold too high. Here, the threshold has been set to about 80% of the breathing curve maximum by monitoring the breathing waveform prior to the 4DCT for a certain amount of time. This results in an early triggering of the CT scan before maximum inhalation, but minimizes the risk of missing triggers. It is important to note that the 80% threshold level can only be chosen before the start of the actual CT acquisition. Therefore, the optimal threshold level would have to vary in relation to the breathing curve throughout CT acquisition. The CT uses these triggers to assign ten equidistant breathing phases to the oversampled raw data acquired during the acquisition time of the CT scan. This reconstruction method is what we later refer to as "original" cycle-based sorting (*Original CBS*).

One major source of error in the assignment of the triggers hereby is the prospective threshold method of the Sentinel[TM]

system: Baseline drifts and variations of the breathing curve, which can occur with every real patient, will not allow this method to generate trigger pulses at the maximum of the curve while securing that no trigger pulse is left out in the acquisition. To overcome these restrictions, an in-house software solution was built using MATLAB[®] (The MathWorks Inc., Natick, MA, USA), in which the real maxima of the previously stored breathing signal during 4DCT acquisition are determined using the zero crossing of the first derivative of the input signal. Retrospective user interaction is needed to control and eventually adjust the calculated maxima which are eventually used as new trigger pulses for the CT reconstruction. Using these new trigger pulses, the CT can reconstruct the ten 4DCT phases in equidistant timepoints between two maxima of the breathing waveform. This method is later on referred to as "manipulated" cycle-based sorting (*Manipulated CBS*),

Additionally, a local amplitude-based sorting (*LAS*) algorithm has been implemented: The real maxima and the minima of the previously acquired breathing curve are determined offline, again according to the zero crossing of the first derivative. Subsequently, the actual phase of each breathing cycle is determined by dividing the amplitude between the decrease from maximum to minimum into 5 equidistant steps and repeating the same procedure for the increase to the next maximum. This way, it can be ensured that the 0% phase of the 4DCT is always at the maximum of the breathing curve while the 50% phase is always at each minimum. A comparison of these three different techniques (original CBS, manipulated CBS, and LAS) is depicted in Fig. 1.
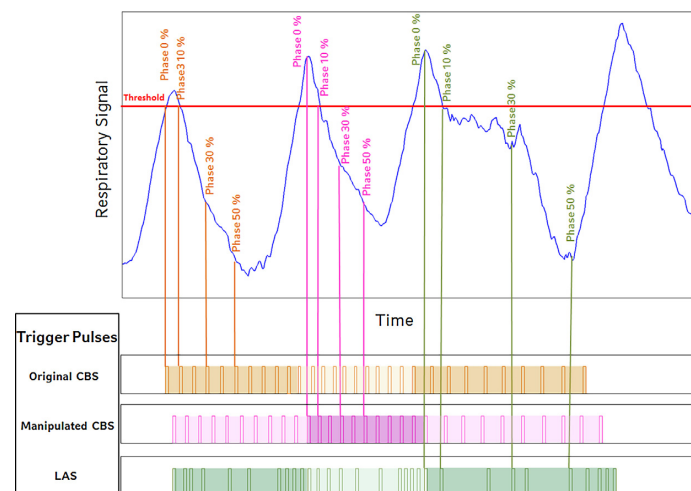
Figure 1. Comparison of the three different image sorting algorithms. One full breathing cycle for each binning method is indicated with the highlighted background of the trigger pulses. The original CBS approach (orange) uses a threshold in order to determine the 0% phase of the breathing waveform and thus generates trigger pulses always ahead of the real maximum. Through correction (manipulated CBS, magenta) this phase shift is eliminated. The influence of LAS (green) becomes obvious at the presence of breathing irregularities.

2.2 Data evaluation

The performance of the three different binning methods (*original CBS*, *manipulated CBS*, and *LAS*) have now been compared by evaluating each "tumor" volume of the corresponding reconstructed 4DCT motion phase. For the phantom study, a MATLAB® script was implemented for an intensity-based automatic segmentation of the "tumor" and volume differences could be evaluated and compared to the "tumor" volume observed in a CT scan in absence of any tumor motion, which is referred to as *reference CT*. The means and standard deviation values for the volume differences between the individual 4DCT phases and the *reference CT* have been calculated over all breathing curves used on the phantom.

For the patient study, the tumor has been delineated in each single breathing phase using Oncentra Ver4.3.0.410 (Nucletron B.V., Netherlands) by an experienced radiation oncologist and controlled by a supervising radiation oncologist. As usually no reference CT without tumor movement is available in real patient data, tumor volume variability (TVV) has been calculated as the relative difference between the tumor volume in each respiratory phase to the mean tumor volume over all 4DCT phases for each reconstruction method. Additionally, the volume of a 3D-CT has been compared to the average of the ten delineated 4DCT phases in each single respiratory phase.

A Wilcoxon signed-ranked test has been performed to compare the TVV results of the different reconstruction methods and Spearman's rank correlation has been used to determine to what extend the baseline drift influences the reconstruction. For statistical significance, $p > 0.05$ has been chosen.

3 Results

3.1 Phantom evaluation

The mean volume of the "tumor" of the moving phantom for all breathing curves can be found in Table 2. The original volume is calculated from the CT dataset of the static tumor as 4.1 cm^3 and serves as a reference. The mean and standard deviation values for each phase binning method and each phantom breathing curve were calculated with respect to the original volume. The tumor volume in a "free-breathing" 3D-CT scan with tumor motion has also been calculated for each phantom motion curve. Due to missing slices in the reconstructions of the 4DCT phases using patient curves 5 & 6 when using the original triggers, the resulting volumes cannot clearly be compared to the other binning algorithms. When rejecting these volumes from the calculations, the mean difference to the actual volume (measured using the reference CT) is the smallest for LAS ($2.7 \pm 2.2\%$) and $2.7 \pm 2.6\%$ using manipulated CBS. When using the original triggers provided by the Sentinel™ system, the difference is found to be as high as

Table 2
The difference in reconstruction volume to the volume measured in the reference CT (ΔV). For each 4DCT reconstruction, 10 breathing phases were used per breathing curve. The percentage values (mean ± standard deviation over all phantom breathing curves) are always compared to the reference volume of the tumor phantom of 4.1 cm^3. As missing slices appear in the reconstructions that used patient breathing curves 5 and 6, a second calculation has been performed to exclude the impact of the artifacts.

	Pat 5 & 6 included		Without patients 5 & 6	
	ΔV/cm^3	ΔV/%	ΔV/cm^3	ΔV/%
Free breathing CT	0.5 ± 0.7	9.7 ± 16.5	0.5 ± 0.7	13.0 ± 18.0
Original CBS	0.3 ± 0.2	7.1 ± 5.0	0.1 ± 0.2	2.9 ± 3.7
Manipulated CBS	0.2 ± 0.1	4.7 ± 2.8	0.1 ± 0.1	2.7 ± 2.6
LAS	0.2 ± 0.1	4.5 ± 2.4	0.1 ± 0.1	2.7 ± 2.2

$2.9 \pm 3.7\%$. The missing slices when using patient curve 6 were due to missed triggers (below the threshold) in the original CBS reconstruction, while missing slices in patient curve 5 occurred within all data sorting methods due to the variations in the breathing rate and the limitations of the Toshiba CT scanner (raw data acquisition is only possible with breathing rates ≥ 10 bpm, see [10]).

On average, LAS provides the least inaccuracies compared to the volume of the reference CT. With a smaller standard deviation, the consistency of the LAS method remains more precise, closely followed by the manipulated cycle-based trigger sorting method. The original trigger sorting scores the lowest of the three methods. An overview of the individual relative deviation to the reference volume of the static CT is depicted in Fig. 2. However, when comparing the results to the measured volumes in a 3D-CT without any 4D information, it turns evident that all 4DCT reconstruction algorithms investigated will generate a better reconstruction of moving volumes. The free breathing CT has a mean difference to the actual volume of $13.0 \pm 18.0\%$ when all breathing curves are taken into account.

3.2 Patient data evaluation

Overall, most patients show reduced TVV when using both the manipulated CBS and the LAS approach. Conversely, TVVs of patient 4 showed no clinically significant differences when comparing the three different 4DCT reconstructions. The relative deviation resulting from manual contouring is high due to the small tumor volumes of $V_{Tumor\_Mean} = 0.79$ cm^3. The second tumor site in patient 7 (7/2) was rather hard to delineate due to the surrounding tissue. As the baseline drift of patient 6 has been estimated to exceed 33%, the superiority of the two new approaches is indicated by a significantly reduced TVV. Over all patients, excluding patient 4 due to the significantly small tumor volume and patient 8 due to artifacts in the 4DCT reconstruction, TVV has been measured highest when using the "original" proposed
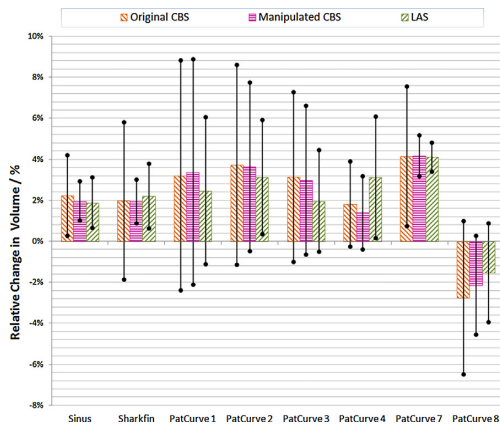
Figure 2. Comparison of the different data sorting methods for the phantom study with 10 different breathing curves as an input for the thorax phantom. The respective relative deviation to the reference volume with the corresponding standard deviation is depicted here. The patient curves 5 and 6 were left out on purpose due to missing slices in the reconstruction.
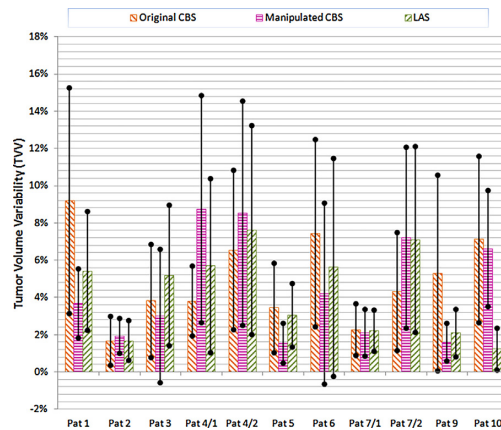
Figure 3. Tumor volume variability (TVV) for all patients, as it has been delineated by an experienced radiation oncologist for the patient study. TVV was calculated as the relative difference to the mean tumor volume over all phases. Patient 8 is left out in the graphic due to artifacts in the 4DCT reconstruction.

workflow of the manufacturers relying on cycle-based triggers ($TVV_{mean} = 5.0 \pm 3.6\%$). A significant reduction ($p < 0.01$) of TVV is observable by using either the manipulated cycle-based method or the LAS approach. No statistical significance between the three methods has been observed when including all patient datasets except patient 8 (excluded for artifacts). TVV in the manipulated cycle-based reconstruction could be reduced from $5.0 \pm 3.6\%$ (original CBS) to $3.5 \pm 2.5\%$ and to $3.7 \pm 2.7\%$ when reconstructing the 4DCT phases according to the LAS approach. Fig. 3 gives an overview of the

patient results excluding patient 8 due to missing slices in the reconstruction in the tumor volume.

When comparing the tumor volume in the free breathing CT scan to the average of delineated volumes in each single respiratory phase using LAS reconstruction, the need of 4DCTs becomes obvious: Tumor volume was overestimated in 2 of the 3D-CT scans by 11.0% and 17.0% and underestimated in 8 tumor sites ranging from 4.4% to 30.4%. The correlation between the baseline drift and the difference in TVV between LAS and original CBS shows that there is a high positive correlation ($r = 0.85$), which indicated that the

Figure 4. Example of the different 4DCT trigger binning methods for the moving tumor of patient 5. The red arrows indicate an observable phase shift (1), artifacts in the reconstruction (2), and missed information in a specific breathing phase (3), all of them appearing in the original CBS 4DCT reconstruction.

higher the baseline drift, the better the reconstruction using the LAS algorithm. The correlation between baseline drift and the difference between the manipulated and the original CBS approach indicates the same with a slightly lower correlation coefficient ($r = 0.70$). Fig. 4 demonstrates the variability of tumor motion in the different respiratory phases when using different 4D data sorting methods: The phase shift in the reconstruction using the original cycle-based approach can be clearly seen in this illustrative case, although all three reconstructions have their origin in the same raw dataset. This phase shift adds up to the reconstruction error made by the original CBS approach.

4 Discussion

We evaluated the imaging workflow using the Sentinel[TM] laser surface scanner and a large bore CT scanner (Toshiba Aquilion LB) specifically acquired for exclusive use in a radiotherapy department, which has to be optimized in order to be clinically applicable: Using the triggers originally provided by the Sentinel[TM] system leads to differences in tumor volume of up to $\Delta V = 2.9 \pm 3.7\%$ even when not taking missing slices in the different 4DCT phases into account ($\Delta V = 7.1 \pm 5.0\%$ when accounting for the missed triggers). Both tested improvements of the workflow showed reduced tumor volume differences ($\Delta V_{Manipulated\ CBS} = 2.7 \pm 2.6\%$ and $\Delta V_{LAS} = 2.7 \pm 2.2\%$).

In the patient data evaluation, TVV was also reduced using the manipulated CBS and LAS data sorting methods for specific patient cases, while some 4DCT reconstructions did not show improvements when using the newly adapted workflow. As illustrated in Fig. 3, the secondary tumor site in patient 4 and 7 show even larger TVVs when using the manipulated CBS and the LAS method, while in patient 2 and the primary tumor site of patient 7, no significant difference in TVV is observed. These cases seem to restrict the robustness of the newly proposed workflows, which was demonstrated in the phantom study. These findings can be attributed to either small motion amplitudes (patient 7(1)), where a measurement such as TVV is limited by the minor differences in the various 4DCT phases, or to very small tumor volume, as in patient 4, where the small absolute volume differences seem to be quite large relative to the small tumor volume itself. The results also illustrate the advantages of 4DCT scans compared to a free breathing CT, which is in good agreement to previous findings [2]. Tumor volume deviations of up to $13.0 \pm 18.0\%$ can lead to larger uncertainties in planning and evaluation of the tumor position.

Although the importance of using phase-based algorithms for image sorting is reported [11,3,12], better image quality and less motion artifacts are described when using amplitude-based approaches [13,14]. Werner et al. also describes an optimized LAS binning approach similar to the one depicted in this work, in order to minimize artifacts in 4DCT reconstruction [15]. Other CT vendors offer the possibility of using different binning algorithms directly, while the simple usage of these algorithms are limited when using Toshiba CT scanners: Here there is no known functionality of changing the reconstruction method in the CT console directly. Unfortunately, due to limitations in accessibility to other systems, we could not perform a thorough comparison of the different CT scanners and surrogate motion detection systems under comparable conditions. Rather, we aimed at closely investigating the performance of the Toshiba scanner to which we have access, and propose a clinically viable solution to overcome limitations of this system, which was obviously not initially designed for 4D imaging applications in radiation therapy.

With the known abnormalities and irregularities of breathing signals, there is no other possibility than using retrospective image sorting, especially for lung cancer patients. Recently, another similar method for the reconstruction of lossy raw data or irregular breathing motions in 4DCT has been introduced and tested on a phantom [16]. A reduced deviation in the measured tumor volume of about 13.4% has been found when using an alternative LAS algorithm compared to a cycle-based approach. Kupper et al. also concluded that a need for retrospective adaption of the breathing signal becomes inevitable at the occurrence of breathing irregularities [16]. Rietzel et al. found improved 4DCT quality due to reduced residual motion artifacts when using manual retrospective manipulation of the trigger signals sent to a CT scanner when using a RPM-system (Varian Medical Systems Inc., USA) [17]. They concluded in congruence with our results that the RPM system (as well as the Sentinel[TM] in our case) has originally been developed as a surrogate for gated treatment and retrospective postprocessing of the trigger motion trace is needed. The influence of baseline drifts could not be thoroughly examined in this study, as only two of the patients evaluated showed drifts of more than 10%, while one patient with a large baseline drift has been excluded from the results of the study due to missing slices in the reconstructed 4DCT phases and is only mentioned for completeness.

Missing CT slices are often a consequence of suboptimal triggering conditions, which apply using the original CBS method. The breathing signal typically does vary in amplitude and respiration period. When only using a single threshold in order to try to determine the maximum inhalation phase, a high risk of failure occurs: Prospectively trying to choose the threshold too high will lead to missing triggers while choosing it on a lower threshold level will not trigger the CT in the desired breathing curve maximum. If the breathing waveform remains always constant over time, this low threshold level would have little impact on the triggering. However, the possibility of accidentally binning slices from one respiration phase to a different one remains. When reconstructing 4DCTs using the original CBS approach, an underestimation of the absolute tumor movement could occur, as slices in the maximum inhalation and exhalation phase could be left out in the reconstruction simply because of the absence of any trigger at the timepoint.

Recently, Thengumpallili et al. evaluated the commercially available amplitude and phase-based reconstruction algorithms in a Toshiba LB CT scanner and did not find any significant differences in the reconstruction quality, but pointed out the importance of adaptive retrospective sorting when variations in the breathing pattern become obvious during the CT scan [18]. In the phantom evaluation, factors as baseline drifts and variability of the breathing signal were simplified in comparison to real patient movements. The baseline drift has two major sources: one is the previously mentioned breathing variability as it occurs with every patient, the second one has its origin in the position and weight dependent couch deflection, which is a specific issue of the Sentinel^{TM} laser surface scanner [10]. A compensation of the baseline drifts as proposed in Guckenberger et al. [3] cannot fully be implemented at our site and others using a Sentinel^{TM} surface scanner, because a part of the baseline drift is coming from the couch deflection itself and is not part of an actual drift in the breathing curve on the patients' surfaces [10]. It has to be mentioned, that for the thorax phantom the external surrogate correlated perfectly with the internal movement. This approximation is no longer valid in realistic patient breathing motion.

The differences in TVV seem to be of minor clinical relevance when using ITV (internal target volume) concepts, as these have only limited impact on the final PTV margin. The real clinical issues are potential phase shifts as they can be observed here, the possibility of missed slices, the error made when it comes to 4D calculations, or treatment planning on a specific breathing phase, including techniques such as gating or tumor tracking. Even small uncertainties in tumor volume will lead to errors in dose calculation while phase shifts and missed slices could lead to significant underestimations of tumor volume and movement range.

An overall improvement of 4DCT quality by accounting for breathing irregularities could be visual and/or audio coaching of the patients [19,20], which also can be an advantage during the course of treatment when using ITV concepts and is essential for more complex methods like gating or tracking. Patient coaching can only be assured with a clinical setting that is able to coach the patient during the CT while ensuring that during treatment, the patient receives the exact same feedback to provide a workflow for efficient and reproducible biofeedback. 4DCT phases could also be used for the planning of gated treatment: Improved binning methods can diminish the error in phase shift in order to gain maximum precision. But the crucial aspect again is accuracy, as for some linacs, the delivery latency can be up to 800 ms [21]. If now the phase shift between the reconstructed CT phase at for example 50% and the breathing signal at the patient's surface could be enlarged due to poor 4DCT reconstruction when using an external surface position as surrogate, errors in gated treatment would become unforeseeable when one has to account not only for this phase shift, but also for the linac latency. The outline and therefore the limit of this study was to focus on geometric uncertainties in 4DCT reconstruction. When it comes to distinguishing certain advantages for treatment techniques such as gating, more measurements have to be performed (i.e. an examination of the phase shift between surrogate and tumor motion).

One major problem with the proposed workflow for the generation of trigger pulses for LAS is the lack in automation: Toshiba Aquilion CT scanners only allow cycle-based approaches, so when it comes to unequal phase distances, one has to manually send trigger pulses at each phase individually to the CT scanner and the resulting reconstruction always has the DICOM tag "RPM 0%" (which represents the 0% phase). So after the reconstructions, one has to be sure that renaming the breathing phases is performed in a reproducible way. Both of the manipulated workflows (manipulated CBS and LAS) require user interventions in a deeper level of the CT IT infrastructure. The resulting 4DCT reconstructions therefore would have to be validated and tested extensively because of this manual interference with the certified workflow designed by the manufacturers. These user interactions, if not carried out properly and without any validation process can lead to significant errors in the assessment of breathing motions and bears the possibility of underestimating the tumor movement. Manual sorting therefore has to be carried out with respect to the complexity and clinical relevance of possible results.

5 Conclusion

This study showed that 4DCT reconstruction using LAS and the manipulated CBS approach both reduce TVV when comparing them to the original CBS approach of the manufacturer for all phantom cases and most of the patient cases. Also, phase accuracy, meaning that the 0% phase will always represent the maximum inhalation phase, can be assured when using both improved methods. Due a shift of the triggers in the original approach, the maximal tumor movement could be underestimated as some CT slices will be assigned to different phases because of the static threshold in combination with breathing variations. It is expected for the LAS approach to show significant reductions of the TVV when using more patient data, which is planned in the future, but the LAS method appears to be quite impractical due to Toshiba restrictions, as every trigger file for each phase has to be manually sent to the CT for a single reconstruction of this motion state. This method would be prone to errors and could lack in consistency when using it clinically if it is not implemented by the manufacturers Toshiba and C-RAD AB.

Therefore, we recommend reconstructing 4DCTs based on equally divided respiration phases over time with the trigger points set to the true maximum of the breathing curve (manipulated CBS), which serves as a valid compromise with minimal extra workload clinically and improved 4DCT image quality, which should be integrated by the manufacturers. The

study will continue with the evaluation of more patient data to validate the clinical concept.

References

[1] Wang W, Li JB, Hu HG, Li FX, Xu M, Sun T, et al. Correlation between target motion and the dosimetric variance of breast and organ at risk during whole breast radiotherapy using 4DCT. Radiat Oncol 2013;8:111.

[2] Keall PJ, Mageras GS, Balter JM, Emery RS, Forster KM, Jiang SB, et al. The management of respiratory motion in radiation oncology report of AAPM task group 76. Med Phys 2006;33(10):3874, http://dx.doi.org/10.1118/1.2349696.

[3] Guckenberger M, Weininger M, Wilbert J, Richter A, Baier K, Krieger T, et al. Influence of retrospective sorting on image quality in respiratory correlated computed tomography. Radiother Oncol 2007;85(2):223–31, http://dx.doi.org/10.1016/j.radonc.2007.08.002.

[4] Ford EC, Mageras GS, Yorke E, Ling CC. Respiration-correlated spiral CT: a method of measuring respiratory-induced anatomic motion for radiation treatment planning. Med Phys 2003;30(1):88, http://dx.doi.org/10.1118/1.1531177.

[5] Keall PJ, Starkschall G, Shukla H, Forster KM, Ortiz V, Stevens CW, et al. Acquiring 4D thoracic CT scans using a multislice helical method. Phys Med Biol 2004;49(10):2053–67, http://dx.doi.org/10.1088/0031-9155/49/10/015.

[6] Low DA, Nystrom M, Kalinin E, Parikh P, Dempsey JF, Bradley JD, et al. A method for the reconstruction of four-dimensional synchronized CT scans acquired during free breathing. Med Phys 2003;30(6):1254, http://dx.doi.org/10.1118/1.1576230.

[7] Mageras GS, Pevsner A, Yorke ED, Rosenzweig KE, Ford EC, Hertanto A, et al. Measurement of lung tumor motion using respiration-correlated CT. Int J Radiat Oncol Biol Phys 2004;60(3):933–41, http://dx.doi.org/10.1016/j.ijrobp.2004.06.021.

[8] Siva S, Pham D, Gill S, Bressel M, Dang K, Devereux T, et al. An analysis of respiratory induced kidney motion on four-dimensional computed tomography and its implications for stereotactic kidney radiotherapy. Radiat Oncol 2013;8:248, http://dx.doi.org/10.1186/1748-717X-8-248.

[9] Brahme A, Nyman P, Skatt B. 4D laser camera for accurate patient positioning, collision avoidance, image fusion and adaptive approaches during diagnostic and therapeutic procedures. Med Phys 2008;35(5):1670, http://dx.doi.org/10.1118/1.2889720.

[10] Heinz C, Reiner M, Belka C, Walter F, Söhn M. Technical evaluation of different respiratory monitoring systems used for 4D CT acquisition under free breathing. J Appl Clin Med Phys 2015;16(2):4917.

[11] Abdelnour AF, Nehmeh SA, Pan T, Humm JL, Vernon P, Schöder H, et al. Phase and amplitude binning for 4D-CT imaging. Phys Med Biol 2007;52(12):3515–29, http://dx.doi.org/10.1118/1.2240236.

[12] Li H, Noel C, Garcia-Ramirez J, Low D, Bradley J, Robinson C, et al. Clinical evaluations of an amplitude-based binning algorithm for 4DCT reconstruction in radiation therapy. Med Phys 2012;39(2):922, http://dx.doi.org/10.1118/1.3679015.

[13] Lu W, Parikh PJ, Hubenschmidt JP, Bradley JD, Low DA. A comparison between amplitude sorting and phase-angle sorting using external respiratory measurement for 4D CT. Med Phys 2006;33(8):2964–74, http://dx.doi.org/10.1118/1.2219772.

[14] Wink NM, Panknin C, Solberg TD. Phase versus amplitude sorting of 4D-CT data. J Appl Clin Med Phys 2006;7(1):77–85, http://dx.doi.org/10.1120/jacmp.2027.25373.

[15] Werner R, Hofmann C, Gauer T. Optimized projection binning for improved helical amplitude- and phase-based 4DCT reconstruction in the presence of breathing irregularity. Prog Biomed Opt Imaging - Proc SPIE 2016;9783:978313, http://dx.doi.org/10.1117/12.2216187.

[16] Kupper M, Sprengel W, Winkler P, Zurl B. A method for improved 4D-computed tomography data acquisition. Z Med Phys 2017;27(1):31–8, http://dx.doi.org/10.1016/j.zemedi.2016.05.001.

[17] Rietzel E, Chen GTY. Improving retrospective sorting of 4D computed tomography data. Med Phys 2006;33(2):377–9, http://dx.doi.org/10.1118/1.2150780.

[18] Thengumpallil S, Germond JF, Bourhis J, Bochud F, Moeckli R. Impact of respiratory-correlated CT sorting algorithms on the choice of margin definition for free-breathing lung radiotherapy treatments. Radiother Oncol 2016;119(3):438–43, http://dx.doi.org/10.1016/j.radonc.2016.03.015.

[19] Kini VR, Vedam SS, Keall PJ, Patil S, Chen C, Mohan R. Patient training in respiratory-gated radiotherapy. Med Dosim 2003;28(1):7–11, http://dx.doi.org/10.1016/S0958-3947(02)00136-X.

[20] George R, Chung TD, Vedam SS, Ramakrishnan V, Mohan R, Weiss E, et al. Audio-visual biofeedback for respiratory-gated radiotherapy: impact of audio instruction and audio-visual biofeedback on respiratory-gated radiotherapy. Int J Radiat Oncol Biol Phys 2006;65(3):924–33, http://dx.doi.org/10.1016/j.ijrobp.2006.02.035.

[21] Freislederer P, Reiner M, Hoischen W, Quanz A, Heinz C, Walter F, et al. Characteristics of gated treatment using an optical surface imaging and gating system on an Elekta linac. Radiat Oncol 2015;10(1):1–6, http://dx.doi.org/10.1186/s13014-015-0376-x.

Chapter 7

Paper 2: Comparison of Planned Dose on Different CT Image Sets to Four-dimensional Monte Carlo Dose Recalculation Using the Patient's Actual Breathing Trace for Lung Stereotactic Body Radiation Therapy

---

Comparison of planned dose on different CT image sets to four-dimensional Monte Carlo dose recalculation using the patient's actual breathing trace for lung stereotactic body radiation therapy

Philipp Freislederer,[a] Asmus von Münchow, Florian Kamp, Christian Heinz, Sabine Gerum,
Stefanie Corradini, Matthias Söhn, and Michael Reiner
Department of Radiation Oncology, University Hospital, LMU Munich, Munich, Germany

Falk Roeder
Department of Radiotherapy and Radiation Oncology, Paracelsus Medical University, Landeskrankenhaus, Salzburg, Austria
CCU Molecular Radiation Oncology, German Cancer Research Center (DKFZ), Heidelberg, Germany

Ralf Floca
Heidelberg Institute of Radiation Oncology (HIRO), National Center for Radiation Research in Oncology (NCRO), Heidelberg, Germany
Division of Medical Image Computing, German Cancer Research Center (DKFZ), Heidelberg, Germany

Markus Alber
Heidelberg Institute of Radiation Oncology (HIRO), National Center for Radiation Research in Oncology (NCRO), Heidelberg, Germany
Department of Radiation Oncology, Heidelberg University Hospital, Heidelberg, Germany

Claus Belka
Department of Radiation Oncology, University Hospital, LMU Munich, Munich, Germany
German Cancer Consortium (DKTK), Munich, Germany
Member of the German Center for Lung Research (DZL), Comprehensive Pneumology Center Munich (CPC-M), Munich, Germany

Katia Parodi
Department of Experimental Physics - Medical Physics, LMU Munich, Munich, Germany

Purpose: The need for four-dimensional (4D) treatment planning becomes indispensable when it comes to radiation therapy for moving tumors in the thoracic and abdominal regions. The primary purpose of this study is to combine the actual breathing trace during each individual treatment fraction with the Linac's log file information and Monte Carlo 4D dose calculations. We investigated this workflow on multiple computed tomography (CT) datasets in a clinical environment for stereotactic body radiation therapy (SBRT) treatment planning.

Methods: We have developed a workflow, which allows us to recalculate absorbed dose to a 4DCT dataset using Monte Carlo calculation methods and accumulate all 4D doses in order to compare them to the planned dose using the Linac's log file, a 4DCT dataset, and the patient's actual breathing curve for each individual fraction. For five lung patients, three-dimensional-conformal radiation therapy (3D-CRT) and volumetric modulated arc treatment (VMAT) treatment plans were generated on four different CT image datasets: a native free-breathing 3DCT, an average intensity projection (AIP) and a maximum intensity projection (MIP) CT both obtained from a 4DCT, and a 3DCT with density overrides based on the 3DCT (DO). The Monte Carlo 4D dose has been calculated on each 4DCT phase using the Linac's log file and the patient's breathing trace as a surrogate for tumor motion and dose was accumulated to the gross tumor volume (GTV) at the 50% breathing phase (end of exhale) using deformable image registration.

Results: $\Delta D_{98\%}$ and $\Delta D_{2\%}$ between 4D dose and planned dose differed largely for 3DCT-based planning and also for DO in three patients. Least dose differences between planned and recalculated dose have been found for AIP and MIP treatment planning which both tend to be superior to DO, but the results indicate a dependency on the breathing variability, tumor motion, and size. An interplay effect has not been observed in the small patient cohort.

Conclusions: We have developed a workflow which, to our best knowledge, is the first incorporation of the patient breathing trace over the course of all individual treatment fractions with the Linac's log file information and 4D Monte Carlo recalculations of the actual treated dose. Due to the small patient cohort, no clear recommendation on which CT can be used for SBRT treatment planning can be given, but the developed workflow, after adaption for clinical use, could be used to enhance a priori 4D Monte Carlo treatment planning in the future and help with the decision on which CT dataset treatment planning should be carried out. © *2019 American Association of Physicists in Medicine* [https://doi.org/10.1002/mp.13579]

1. INTRODUCTION

In radiation therapy of thoracic and abdominal tumor sites, the management of respiratory motion is still one of the great challenges even in the presence of various motion compensation approaches, especially in stereotactic body radiation therapy (SBRT).[1,2] With increased complexity of treatment techniques such as intensity-modulated radiation therapy (IMRT) or volumetric modulated arc treatment (VMAT), the interplay effect between a dynamically moving multileaf collimator (MLC) or the Linac gantry for VMAT and the intrafractionally moving tumor may become relevant.[3–5] The dosimetric impact is highly dependent on target motion and the number of fractions[6] and can cause differences between planned and actually delivered dose distributions in the whole target region and surrounding organs-at-risk (OAR) structures.[7] Using four-dimensional computed tomography (4DCT), target motion can be evaluated thoroughly.[8–11] The respiratory motion information gained from 4DCT imaging can be used in various ways: Tumor motion can be encompassed in a so-called internal target volume (ITV) structure,[12] defined by either the sum of GTVs of a 4DCT or with an average intensity projection (AIP) or a maximum intensity projection (MIP),[13] which both can be generated from the 4DCT dataset for motion information on a single CT dataset. Typically, one free-breathing (FB) 3DCT dataset is used for dose calculations with the restriction of suffering from artifacts due to breathing-induced motion of the target and OAR structures, partially due to limited availability of 4DCTs. MIP could be used for treatment planning, but may over- or underestimate the target volume, while AIP could serve as a valid CT basis for dose calculations.[14–17] Another approach to solving the problem of modeling dose to a target volume with high density tissue surrounded by low density lung tissue in SBRT treatments are density overrides in the planning target volume (PTV) and the ITV. These overrides also promise to perform well in comparison with FB and AIP-based dose calculations.[18]

Monte Carlo dose distributions can be recalculated on each single 4DCT breathing phase and merged back onto a 3DCT for evaluation.[19,20] This so-called 4D dose mapping has been performed using direct dose mapping,[21] energy transfer methods[22], and voxel warping methods.[23,24] Simplified approaches for 4D treatment planning have already been studied thoroughly. Rosu et al[25] concluded that dose differences between the calculation on multiple 4DCT phases and a calculation based on a single CT dataset which incorporates the full breathing motion range (i.e., AIP) is lower than 2% on three evaluated patients. An overview of 4D treatment planning options can be found in Rosu et al.[26]

Linear accelerator (Linac) log files (where each delivered monitor unit (MU) and the corresponding MLC, gantry, and collimator positions are recorded) allow a retrospective creation of the delivered treatment plan. These log files, in combination with Monte Carlo dose engines and the 4D target motion information, have been used to build a delivery reconstruction simulator, in order to evaluate the interplay effects in a moving phantom.[27] However, Monte Carlo calculations utilizing the actual patient breathing curve over the course of multiple fractions have not been performed yet.

In this study, first, we aim to combine the actual breathing trace of a patient cohort with the Linac's log file and Monte Carlo 4D dose recalculations for 3D-conformal radiation therapy (3D-CRT) and VMAT treatment plans individually for each treatment fraction. To the best of our knowledge, this is the first incorporation of the actual patient breathing trace for all individual treatment fractions with the Linac's log file information and 4D Monte Carlo recalculations of the actual treated dose. Second, we investigate this workflow by comparing the Monte Carlo dose calculation based on a static FB 3DCT, the AIP, the MIP, and density overrides in ITV and PTV with 4D Monte Carlo dose recalculations, in order to precisely evaluate which calculation basis can give us the most reliable results.

2. MATERIALS AND METHODS

2.A. Patients

Five patients (one female and four male, age between 49 and 79 yr, mean age 66.8 yr) treated with SBRT for lung tumors have been selected for the present study. The main selection criteria were high tumor mobility resulting in the evaluation of one lesion in the upper lung lobe and four lesions in the lower lobe, located close to the diaphragm. Tumor movement was evaluated using a 4DCT acquired with a Toshiba Aquilion LB CT scanner (Canon Medical Systems Corporation, Japan). All 4DCTs were acquired with the following parameters: slice collimation of 16 mm × 1.0 mm, helical pitch of 1.2, rotation time of 0.5 s, tube voltage of 120 kV, and tube current of 150 mA. Images were reconstructed in 3 mm slices with pixel size of 1.074 mm and a matrix of 512 × 512. A laser-based optical surface scanner (Sentinel[TM], C-RAD AB, Sweden) has been used as to measure patient breathing motion as a surrogate for 4DCT reconstruction. The position of the surrogate spot on each patient's surface has been chosen according to Heinz et al.[28], on the upper abdomen in the region of the diaphragm on the patient's right side. Here, less interferences with cardiac movement, less phase shift compared to spots on the lower abdomen, and a better signal-to-noise (SNR) due to higher amplitude than any other spot on the surface are expected. PTV was defined in accordance with clinical protocol as the sum of the GTVs (to construct an ITV structure) with a 6 mm margin added in all directions. In four of the patients, the dose to the PTV was 40.5 Gy prescribed to the 65%

isodose line and in one patient 40.5 Gy prescribed to the 80% isodose line (both with 100% equaling D_{Max}), delivered over the course of three fractions. A 3D-CRT treatment plan has been calculated based on the 3DCT dataset, according to the standards of our institution. The breathing curves of all patients were recorded at the Linac using an optical surface scanner (Catalyst[TM], C-RAD AB, Sweden) during the whole treatment session for all three fractions individually. Breathing characteristics and tumor mobility for each individual patient are summarized in Table I. The respiratory data collection was approved by the local ethics committee of the University Hospital, LMU Munich (No. 352-16 ex 09/2016) and registered at the German Clinical Trials Register (DRKS-ID: DRKS00011407). Written informed consent was obtained from all patients. All other data processing has been conducted retrospectively and has also been approved by the local ethics committee of the University Hospital, LMU Munich (No. 573-15 ex 10/2015).

The fraction of time in each breathing phase during 4DCT acquisition and throughout each fraction is depicted in Table II.

2.B. Workflow

After the clinical FB 3DCT and 4DCT acquisition (1, for all italic references, see Fig. 1), the raw 4DCT dataset has been resampled in order to reconstruct a local amplitude-sorted (LAS) 4DCT dataset[29] (5), in which all gross tumor volumes (GTVs) were delineated by an experienced radiation oncologist. Apart from the original clinical treatment plan (2), eight different treatment plans were created: 3D-CRT (7) and VMAT (8) plans with the dose calculation based on four different CT sets (3DCT, average intensity projection (AIP), maximum intensity projection (MIP, both reconstructed from all 4D phases), and 3DCT with density overwrites according to Wiant et al.[18] (mean ITV density to the ITV and the mean between ITV and lung density to PTV-ITV)). All VMAT plans were optimized using Hyperion V2.4.5 (University Tübingen, Germany, research version of Elekta MONACO 3.2)[30,31] with two full 360° arcs and a 2 mm isotropic dose grid. 3D-CRT planning was initially performed using

Oncentra Ver4.3.0.410 (Nucletron B.V., Netherlands) with 8–11 different beam angles with field opening covering at least the ITV (the full motion range). All 3D-CRT plans were afterward also recalculated with the same Monte Carlo dose engine using Hyperion V2.4.5, resulting in a 3D Monte Carlo dose comparable to the postplanning 4D Monte Carlo calculations. All eight plans were irradiated (9) on an Elekta Synergy Linac with an Agility Head (Elekta AB, Sweden) to create a Linac log file (10). The log file included elapsed time, corresponding RTPlan control point, dose rate, delivered MUs, Gantry and collimator angle, jaw positions, and all 160 MLC positions, with a time resolution of 0.04 s. The log file information combined with the breathing information gathered during the actual treatment (4) were synchronized using the "beam-on" timestamp provided directly by the Linac interconnection through the Elekta Response[TM] interface (Elekta AB, Sweden) in the recorded Catalyst[TM] breathing motion file. This allows to recalculate the dose delivery based on 4DCTs by splitting the individual plans (11), each with a distinct correspondence to a 4DCT breathing phase as the patient breathing traces were also sampled to a distinct 4DCT phase using the same LAS method as has been applied to the 4DCT reconstruction. Therefore, the breathing signal is downsampled to the log cycle resolution of 0.04 s to obtain the corresponding 4DCT phases during the whole delivery and split the original plan accordingly. All plans were recalculated on the actual 4D-phase (12) using MCverify (with dose-to-medium used for calculations), which is a scriptable submodule XVMC dose engine of Hyperion V2.4.5.[32–35] The resulting dose fragments were accumulated (14) using AVID (Analysis of Variations in Interfractional Radiotherapy, German Cancer Research Center, Heidelberg), a framework for automatic analysis of variations in dose and geometry. In AVID, the ten dose fragments calculated on each 4DCT phase were merged together by first calculating the intensity-based (using B-Splines[36]) deformable image registration (Plastimatch,[37]) to the 50% breathing phase (13). With the registration information, all ten dose fragments could be accumulated, by using the dose accumulation tool of the RTToolbox (RTToolbox[38,39]) eventually leading to a 4D Monte Carlo recalculated dose (15). The dose

TABLE I. Overview of tumor mobility and breathing motion characteristics during four-dimensional computed tomography (4DCT) acquisition and during treatment beam-on time for each fraction. Tumor motion has been measured using an in-house developed software tool with an accuracy of 3 mm in the craniocaudal direction and 1 mm in both left–right and anterior–posterior directions (resolution of the 4DCT reconstruction). Mean GTV has been measured over all GTVs delineated by a radiation oncologist in the ten different 4DCT phases. ITV is the sum of all GTVs. Abbreviations: RR = respiratory rate, bpm = breaths per minute, GTV = gross tumor volume, ITV = internal target volume, SD = standard deviation, CC = craniocaudal, AP = anterior–posterior, RL = right–left, Mag (Magnitude) = $\sqrt{CC^2 + AP^2 + RL^2}$.

					Tumor Movement (mm)			
	Mean RR (CT) (bpm)	Mean RR (Linac) (bpm)	$GTV_{mean} \pm$ SD(cm³)	ITV (cm³)	CC	AP	RL	Mag
Pat 1	18.7	17.0	1.7 ± 0.1	5.0	12	2	3	12.5
Pat 2	17.3	13.0	0.9 ± 0.1	3.2	12	3	1	12.4
Pat 3	11.2	13.1	1.2 ± 0.1	2.7	9	2	1	9.3
Pat 4	14.9	13.6	12.0 ± 0.4	20.8	6	2	3	7.0
Pat 5	15.7	11.7	6.5 ± 0.5	16.4	27	4	3	27.5

TABLE II. Fraction of time in each breathing phase for all patients during four-dimensional computed tomography (4DCT) acquisition and during each treatment fraction (mean value over all fractions with range [min–max]). EOI: end of inhale; EOE: end of exhale.

	Pat 1		Pat 2		Pat 3		Pat 4		Pat 5	
	4DCT (%)	LINAC (%) Mean [Range]	4DCT (%)	LINAC (%) Mean [Range]	4DCT (%)	LINAC (%) Mean [Range]	4DCT (%)	LINAC (%) Mean [Range]	4DCT (%)	LINAC (%) Mean [Range]
0% (EOI)	0.18	0.13 [0.12–0.14]	0.14	0.15 [0.14–0.16]	0.14	0.18 [0.12–0.29]	0.12	0.13 [0.13–0.14]	0.14	0.11 [0.10–0.12]
10%	0.05	0.07 [0.06–0.08]	0.05	0.05 [0.04–0.06]	0.06	0.06 [0.06–0.07]	0.06	0.06 [0.05–0.07]	0.05	0.05 [0.05–0.05]
20%	0.04	0.07 [0.06–0.07]	0.03	0.04 [0.03–0.04]	0.07	0.06 [0.03–0.07]	0.07	0.07 [0.06–0.07]	0.05	0.05 [0.05–0.05]
30%	0.07	0.08 [0.08–0.08]	0.13	0.05 [0.04–0.06]	0.08	0.07 [0.03–0.10]	0.08	0.10 [0.08–0.13]	0.07	0.07 [0.07–0.07]
40%	0.08	0.11 [0.10–0.11]	0.17	0.12 [0.10–0.14]	0.13	0.09 [0.06–0.11]	0.14	0.12 [0.11–0.14]	0.13	0.13 [0.13–0.13]
50% (EOE)	0.30	0.31 [0.27–0.36]	0.20	0.39 [0.35–0.44]	0.21	0.27 [0.21–0.39]	0.25	0.28 [0.26–0.30]	0.31	0.38 [0.36–0.39]
60%	0.06	0.06 [0.06–0.08]	0.17	0.06 [0.05–0.08]	0.07	0.08 [0.06–0.10]	0.10	0.08 [0.07–0.09]	0.06	0.07 [0.07–0.07]
70%	0.05	0.05 [0.05–0.06]	0.04	0.05 [0.05–0.05]	0.09	0.07 [0.03–0.09]	0.06	0.06 [0.04–0.06]	0.06	0.05 [0.05–0.06]
80%	0.10	0.06 [0.05–0.06]	0.04	0.05 [0.05–0.05]	0.07	0.06 [0.02–0.08]	0.06	0.06 [0.05–0.06]	0.06	0.05 [0.05–0.05]
90%	0.07	0.06 [0.06–0.07]	0.04	0.06 [0.05–0.06]	0.09	0.05 [0.03–0.07]	0.05	0.06 [0.04–0.07]	0.06	0.05 [0.05–0.06]

interpolation in the accumulation was performed according to the dose reconstruction scheme of Rosu et al.[21]. All three treatment fraction doses were subsequently merged into one single dose file containing the 4D accumulated dose for comparison. An overview of the workflow can be found in Fig. 1. The workflow, without incorporation of breathing motion, has been previously validated in von Münchow et al.[40]

2.C. Plan evaluation

Dose–volume histograms (DVHs) of the gross tumor volume at the 50% breathing phase ($GTV_{50\%}$, ideally maximum expiration) were created for all optimized treatment plans and for the corresponding 4D dose recalculations. The minimum dose of X% of the GTV is depicted as $D_{X\%}$. $D_{98\%}$ (the minimal absorbed dose covering 98% of the GTV as a robust measure for minimum dose), $D_{50\%}$ (the minimal absorbed dose covering 50% of the GTV), and $D_{2\%}$ (the minimal absorbed dose covering 2% of the GTV as a robust measure for maximum dose) were calculated specifically. In addition, a dose homogeneity index (HI) has been calculated according to ICRU Report 83[41] as:

$$HI = \frac{D_{2\%} - D_{98\%}}{D_{50\%}} \quad (1)$$

A HI of zero would be equivalent to an almost homogeneous absorbed-dose distribution. All DVHs and dose parameters were compared to each other as "$Dose_{optimized}$" (indicating the 3D Monte Carlo dose from the treatment planning system) and "$Dose_{recalculated}$" (indicating the 4D Monte Carlo recalculated dose), with $Dose_{recalculated}$ expected to be the closest approach to the ground truth of absorbed dose.

3. RESULTS

Table III summarizes the dose parameters as the difference between $Dose_{recalculated}$ and $Dose_{optimized}$ for all five patients,

with a negative value indicating less dose observed in the dose recalculation than with plan optimization, which would lead to a GTV underdosage. For 3DCT-based planning, $\Delta D_{98\%}$ and $\Delta D_{50\%}$ are higher on average over all patients for the 3D-CRT and VMAT treatment plans with $Mean_{\Delta D_{98\%;3D-CRT}} = 3.6 \pm 2.6$ Gy and $Mean_{\Delta D_{98\%;VMAT}} = 3.0 \pm 4.0$ Gy, while $D_{2\%}$ experiences an underdosage for 3D-CRT planning with $Mean_{\Delta D_{2\%;3D-CRT}} = -1.7 \pm 0.5$ Gy. AIP-based planning increases the low-dose ($D_{98\%}$) areas in the GTV ($Mean_{\Delta D_{98\%;3D-CRT}} = 2.2 \pm 3.4$ Gy), slightly less using VMAT ($Mean_{\Delta D_{98\%;VMAT}} = 0.8 \pm 1.8$ Gy), while high-dose areas stay within the same range for both treatment planning methods. Absorbed dose in high-dose areas is in good agreement for MIP-based planning over the patient cohort, although on average an underdosage $Mean_{\Delta D_{2\%;VMAT}} = -2.6 \pm 2.7$ Gy and $Mean_{\Delta D_{2\%;3D-CRT}} = -3.4 \pm 1.7$ Gy is calculated for all dose parameters and both treatment techniques, especially for patient 3.

$\Delta D_{98\%}$ varies in the patient cohort ranging from 4.0 Gy in patient 5 to −4.7 Gy in patient 1 (both 3D-CRT). As expected, DO-based planning leads to an underdosage in the GTV due to the higher density in ITV and PTV, for 3D and VMAT plans, especially in high-dose areas. There is a decrease in HI to be observed between 4D recalculations and the optimized planning dose for most patients, although patient 1 experiences a slight increase in homogeneity. Patient 4 with the largest tumor size (and therefore different prescription; 40.5 Gy prescribed to the 80% isodose line) shows the least differences in most dose parameters.

Figure 2 shows the calculated DVHs for two exemplary patients (Pat 2 & Pat 5) for all 3D and all VMAT plans, each with a dose calculation based on a different underlying CT (3DCT, AIP, MIP, DO). In patient 2, the highest differences in the DVHs can be seen for DO and 3DCT-based calculations. The DVHs for both AIP and MIP-based optimization follow closely the form of the DVHs for 4D recalculation. For patient 5, DVH results show larger differences in AIP-based
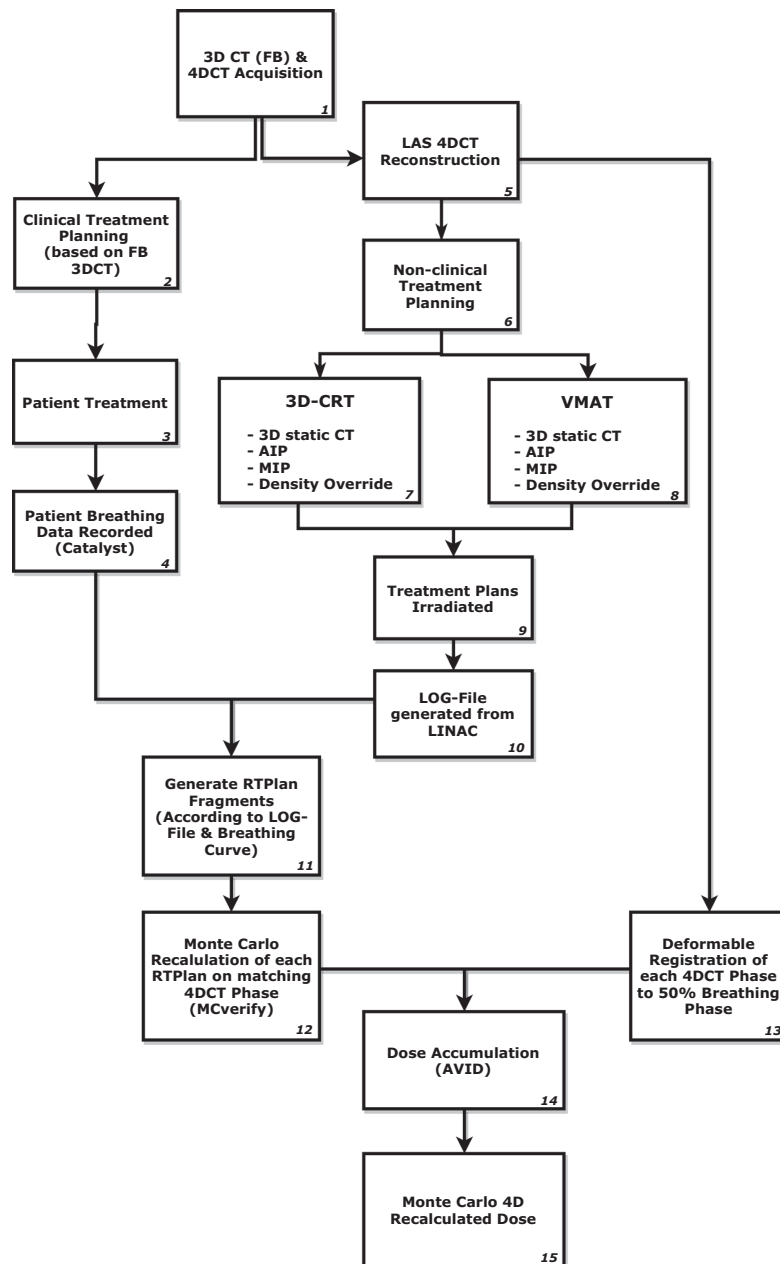
FIG. 1. Scheme of the implemented workflow.

planning and are in better agreement using density overrides.

As seen in Table II, the breathing curve of patient 3 varies the most during each fraction. In order to verify that the fraction of time in each breathing phase is accounted for in the 4D calculations, we calculated the 4D dose exemplary for this patient with the assumption that only fraction 3 has been treated three times (as most variations in the breathing curve occur in this fraction compared to the other fractions). The difference in $\Delta D_{2\%}$ between the 4D calculations for all fractions accounted for and fraction 3 only results in 0.42 Gy for 3DCT-based planning, 0.08 Gy for AIP-based planning, 0.30 Gy for MIP-based planning, and -0.05 Gy for DO-based planning (for VMAT treatment plans).

TABLE III. Dose parameters $D_{98\%}$, $D_{50\%}$, $D_{2\%}$, and the homogeneity index HI, depicted as difference between $Dose_{recalculated}$ and $Dose_{optimized}$ for both calculation methods [three-dimensional-conformal radiation therapy (3D-CRT) and volumetric arc modulated treatment (VMAT)] and all four underlying computed tomographies (CTs) [three-dimensional CT (3DCT), average intensity projection (AIP), maximum intensity projection (MIP), density overrides (DO)]. Negative values indicate an underdosage in the four-dimensional (4D) recalculation, positive values are a result of more absorbed dose in the 4D calculations than planned. SD = standard deviation.

Base CT	3D-CRT				VMAT			
	3DCT	AIP	MIP	DO	3DCT	AIP	MIP	DO
Pat 1								
$\Delta D_{98\%}$ (Gy)	−0.6	−3.5	−4.6	−6.0	−1.0	−2.5	−2.3	−4.2
$\Delta D_{50\%}$ (Gy)	0.7	0.4	−3.2	−5.1	0.1	−0.0	−1.0	−2.6
$\Delta D_{2\%}$ (Gy)	−1.6	−2.0	−4.5	−7.2	−0.7	−0.0	−2.0	−2.3
ΔHI(%)	−0.02	0.03	0.02	0.00	0.00	0.05	0.01	0.04
Pat 2								
$\Delta D_{98\%}$ (Gy)	5.7	1.9	−0.1	1.9	9.1	1.8	0.4	2.9
$\Delta D_{50\%}$ (Gy)	1.9	0.8	−0.5	−2.6	2.4	1.7	1.5	−1.4
$\Delta D_{2\%}$ (Gy)	−1.0	−1.0	−2.5	−3.9	1.4	0.8	0.6	−3.5
ΔHI(%)	−0.13	−0.05	−0.04	−0.09	−0.15	−0.02	0.00	−0.12
Pat 3								
$\Delta D_{98\%}$ (Gy)	6.8	3.3	−1.7	−5.6	6.2	3.0	−3.9	−2.6
$\Delta D_{50\%}$ (Gy)	5.8	3.8	−1.3	−6.7	6.9	4.3	−3.0	−6.2
$\Delta D_{2\%}$ (Gy)	−2.2	−0.5	−6.3	−7.8	−0.3	1.5	−4.3	−7.2
ΔHI(%)	−0.20	−0.08	−0.08	−0.01	−0.15	−0.05	0.01	−0.05
Pat 4								
$\Delta D_{98\%}$ (Gy)	2.5	2.5	1.8	0.9	0.6	1.0	1.9	−0.6
$\Delta D_{50\%}$ (Gy)	1.0	1.2	0.8	−0.2	0.9	1.1	1.0	−1.2
$\Delta D_{2\%}$ (Gy)	−2.1	−1.6	−1.6	−2.5	0.3	0.9	−0.4	−2.5
ΔHI(%)	−0.10	−0.09	−0.07	−0.07	−0.01	−0.01	−0.05	−0.04
Pat 5								
$\Delta D_{98\%}$ (Gy)	3.3	7.0	4.0	0.1	1.1	0.6	2.0	−0.6
$\Delta D_{50\%}$ (Gy)	2.4	4.4	2.1	−0.9	1.3	1.4	0.3	−1.1
$\Delta D_{2\%}$ (Gy)	−1.4	0.1	−2.2	−3.6	−0.6	−0.7	−6.9	−3.4
ΔHI(%)	−0.09	−0.14	−0.12	−0.06	−0.04	−0.03	−0.19	−0.06
Mean ± SD								
$\Delta D_{98\%}$ (Gy)	3.6 ± 2.6	2.2 ± 3.4	−0.1 ± 3.0	−1.7 ± 3.4	3.0 ± 4.0	0.8 ± 1.8	−0.4 ± 2.3	−1.0 ± 2.4
$\Delta D_{50\%}$ (Gy)	2.4 ± 1.8	2.1 ± 1.6	−0.4 ± 1.8	−3.1 ± 2.5	1.9 ± 2.7	1.7 ± 1.4	−0.2 ± 1.6	−2.5 ± 1.9
$\Delta D_{2\%}$ (Gy)	−1.7 ± 0.5	−1.0 ± 0.8	−3.4 ± 1.7	−5.0 ± 2.1	0.0 ± 0.8	0.5 ± 0.8	−2.6 ± 2.7	−3.8 ± 1.8
ΔHI(%)	−0.11 ± 0.06	−0.07 ± 0.05	−0.06 ± 0.04	−0.05 ± 0.03	−0.07 ± 0.07	−0.01 ± 0.03	−0.05 ± 0.08	−0.04 ± 0.05

4. DISCUSSION

Using different CT datasets for dose calculation influences the dose distribution in various ways. In accordance with literature,[1,15,17,42,43] our results also show that the clinical standard of using a simple 3DCT as a so-called "planning CT" does not reflect the delivered dose correctly to the GTV for tumor sites that encompass breathing-induced motion. For small tumor sizes (see patients 2 and 3 with rather small GTVs (0.9 ± 0.1 cm^3 and 1.2 ± 0.1 cm^3, respectively), positive values for $\Delta D_{98\%}$ (minimum dose), indicating less cold spots, have been calculated for 3D-CRT and VMAT treatment techniques. The VMAT optimizer and the 3D-CRT calculation algorithm do not expect tumor tissue in the ITV due to the nature of the 3DCT, where only parts of the ITV are filled with real tumor density. Therefore, the optimizer

calculates more monitor units to the parts of the ITV, where less density is present in order to achieve the prescribed dose, which obviously leads to more hot spots than originally planned in these areas. This was found in most patients except for patient 1, where a slight underdosage has been calculated. Here, the 3DCT seems to encompass tumor motion quite well and planning on the 3DCT will indeed lead to similar results in the 4D calculation and plan optimization.

Using the DO method, the absorbed dose is underestimated in all patients for high-dose areas ($D_{2\%}$). The hybrid density override method of Wiant et al. (mean ITV density to the ITV and the mean between ITV and lung density to PTV-ITV)[18] has been chosen as a result of their study. This specific override does not agree well with our results for patients 1–3. The calculated underdosage in the 4D calculations is observed throughout these patients and cannot be
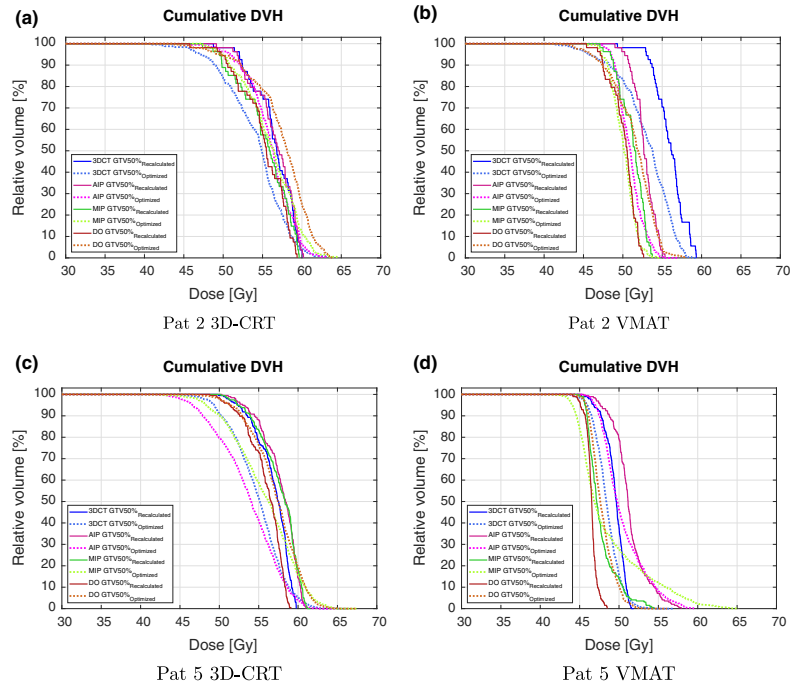
FIG. 2.   Dose–volume histograms (DVHs) for two exemplary patients (Pat 2 & Pat 5): three-dimensional computed tomography (blue), average intensity projection (magenta), maximum intensity projection (green), and density overrides (brown) for the four-dimensional recalculations (solid) and the optimized treatment plan (dashed). Subfigures (a) and (c): three-dimensional-conformal radiation therapy treatment planning; Subfigures (b) and (d): volumetric arc modulated treatment plan optimization. [Color figure can be viewed at wileyonlinelibrary.com]

recommended for SBRT treatments for patients with a small GTV size. For large tumor motion (see Pat 5 with 27.5 mm motion magnitude) and larger tumor sizes (see Pat 4 with $GTV_{mean} = 12.0 \pm 0.4$ cm^3), the density override scheme does fit best in high-dose areas for 3D-CRT and VMAT plans. It is possible that different density overrides (i.e., only overriding the ITV with a certain density) can achieve better results, but this would have to be determined in future studies.

For our small patient cohort, we observed only minor dose differences (in terms of $\Delta = Dose_{recalculated} - Dose_{optimized}$) in AIP- and MIP-based VMAT generations and 3D-CRT treatment plans. Huang et al. evaluated an underdosing (over 10%) in some PTV areas for tumors moving irregularly with a larger range when calculating the Monte Carlo 4D dose on AIP and MIP based on the 4DCT dataset.[16] The dose difference in patient 1 agrees with these results, as also an underdosage is calculated in the 4D dose. For patient 5, with the largest motion amplitude, overdosages in AIP planning are visible. In our study, we only measure the tumor motion based on the surrogate during the treatment time at the Linac, breathing irregularities could not be evaluated thoroughly. We assume that the surrogate motion signal at the patient's surface represents tumor motion, which in reality is not the case due to the nature of breathing motion, which is highly irregular and can contain abnormalities even within a short period of time. An enhancement of our study would be the

direct monitoring of the tumor itself (e.g., in MV/kV projections) and not monitoring a surrogate. Also, Rosu and Hugo note that for an ideal true 4D workflow, online predictive respiratory motion monitoring or real-time tumor tracking (using implantable radiopaque markers[44,45] or MV/kV portal images[46–48]) would be needed.[26] This could be used to create a more realistic representation of the patient compared to the 4DCT acquired days before treatment and to minimize the chances of the 4DCT being an incorrect surrogate of the anatomy at treatment day. The possibility of time-resolved errors is investigated in the exemplary calculation of patient 3 with the highest breathing variability: The potential effects of dose uncertainties due to changes in the patient breathing pattern are explicitly incorporated in our calculations, even if they are neither quantified nor disentangled. The additional complexity in our approach with the calculation based on the Linac log files would also explicitly account for possible machine-related errors and interplay effects.

We did not observe an interplay effect between dynamic MLC movement and tumor motion in this patient cohort, as the differences in dose parameters are within the same range for 3D and VMAT treatments. For SBRT treatments, the interplay effect has little to no effect in the examination of the data of the five patients here. 3D-CRT treatment plans even show higher dose differences between plan recalculations and originally generated plans for all types of underlying CTs in comparison with VMAT plan optimizations. This is due to

the fact that for SBRT VMAT treatments, the ITV structure (as the sum of all GTVs) is completely enclosed by most of the segments. Furthermore, the way that the PTV dose is prescribed could influence the calculations. In this study, we use the same dose specifications for 3D-CRT planning and VMAT inverse optimization: Prescribing the desired isodose level (65% or 80 %) to the PTV and limiting the maximum dose in the PTV to 100% (for 3D-CRT planning directly and for VMAT optimization using a quadratic overdose constraint). Rao et al. investigated the interplay effect for VMAT and IMRT treatment plans and found it to be negligible.[43] This is in accordance with our results, as an interplay effect could not be observed when comparing all VMAT with the 3D-CRT treatment plans. Only for patient 2 with very small tumor volume ($GTV_{mean} = 0.9 \pm 0.1$ cm^3), the data indicate a possible interplay effect. Contradictory to our results, Ehrbar et al. found tumor motion effects in VMAT treatments as negligible.[49] They have recommended the use of AIP with 3D dose calculations as sufficient for treatment planning. Even for this recommended AIP-based treatment planning, we have found dose differences that are not negligible, depending on the motion characteristics of the individual patient.

The evaluation of 4D dose takes time and effort, as the dose has to be calculated on multiple 4DCT breathing phases. A different approach to 4D dose calculations has been investigated by Valdes et al.[50]: They use 4D dose accumulation by deformable image registration without the need of recalculation, which might serve as a tool to accelerate calculation time and limit effort. It is a direct extension of Guckenberger et al.[42], where it was found that the dose to the GTV remains constant over all 4DCT phases. This is only true for treatment plans, where all fields (3D-CRT) or most segments (VMAT) encompass target motion (in our case: the ITV). With fields or segments large enough, one calculation and subsequent 4D deformable image registration can be sufficient. For smaller fields or segments, which do not encompass the full target motion range, the results might look different.

An evaluation of dose-limiting OAR structures would also be of high interest. But as the 4DCT scans have been only acquired within a range of 51 mm above and below the tumor (in CC direction, examined in the 3DCT prior to 4DCT imaging) due to the clinical protocol, this could not be achieved in this study and will be of high interest in future works. A dosimetric evaluation of important OAR structures such as heart, esophagus, or other was not possible within our patient cohort. OAR structures were not anywhere near the PTV and due to the high-dose gradient, OAR structures are only affected with minimal absorbed dose. Any detailed statistical evaluations (i.e., correlations between the magnitude in motion or GTV size and dose differences) could not be carried out due to the small patient cohort. Due to the high calculation effort for each patient, the patient cohort could not be extended for this work, but additional dose calculations for patients with different individual tumor sizes, motions, and breathing patterns are planned in the near future, in order to statistically validate for which type of tumor motion the

various types of CT datasets can be used best. No distinct recommendation on which CT dataset should be used for SBRT treatment planning can be made from the results of our study. As described above, current literature is also not in congruence on this specific topic. Tumor motion is always highly patient specific and the variability of our results and other studies are always highly dependent on certain factors, such as dose calculation algorithm, clinical treatment concept, creation of the PTV with different margins, having open fields/segments encompassing all target motion, but most importantly it is dependent of the patient's individual tumor motion and breathing pattern. Gauer et al. recently found an influence of interplay effects for target motion with abnormal variability (in phantom measurements),[51] which also indicates the patient-specific character of breathing-induced tumor motion.

Potential errors in the deformable registration process could induce errors in dose mapping. Using the 50% breathing phase as a reference CT for registration performs well when inspecting the registration result optically. The dose mapping itself could also lead to significant errors. The dose interpolation method of Rosu et al.[21], which has been used for the accumulation process, has limitations in regions of strong density variations where the partial volume effect is still relevant.[52] According to Rosu et al.[21], who recommended a dose grid size of 3–4 mm to adequately minimize interpolation errors, we have used a 3 mm size in our calculations. The stochastic uncertainty from the Monte Carlo dose calculation was below 1% for all plans and by using the same Monte Carlo dose engine, stochastic variations are within the same range for all 4D recalculations ($Dose_{recalculated}$) and 3D plan generations ($Dose_{optimized}$).

There is an intermediate step leading to the clinical implementation of the workflow described above: modern treatment planning systems (TPS) should at least be able to calculate dose on each phase of a 4DCT (without dose warping or any attention on interplay effects at this point). This simple step could already give an idea of the treatment plan quality for moving targets. For a future perspective, an adaption of this workflow with Monte Carlo 4D recalculations and only few assumptions could be added to modern TPS: With a full 4DCT dataset and the patient's breathing curve recorded over a longer period of time (i.e., before and during 4DCT acquisition), it can be calculated in advance how a 4D dose distribution could behave, depending on certain variability in breathing motion. The, both patient-specific, 4DCT dataset and breathing surrogate are the essential part of a simplified workflow. This could lead to an a priori awareness of the patient-specific 4D dose distribution, which has so far not been incorporated in modern TPS. A general recommendation on which CT should be used for lung SBRT cannot be provided due to the limitations of this study, but our results indicate that the risk of over- or underestimating tumor movement (as it is present for MIP-based calculations[15]) is least probable for AIP-based dose calculations.

The workflow presented in this study is, to our best knowledge, the first implementation of 4D Monte Carlo dose

recalculations using the actual breathing trace of a patient during each individual radiotherapy fraction. Using local amplitude-based 4DCT sorting and the same method for assigning the breathing waveform to the individual 4DCT phases leads to a good approximation of the actual treated dose (within the limitations stated above).

5. CONCLUSION

We have developed a workflow which is, to our best knowledge, the first 4D Monte Carlo dose recalculation using the Linac's log file and the actual patient breathing trace. An approximation of the actual absorbed dose to a 4DCT dataset can calculated for a comparison to the planned dose. This workflow allows us to evaluate if interplay effects have to be accounted for during VMAT treatment plan optimization and helps to decide which CT should be used as a basis for dose calculation and optimization. For 3DCT datasets as a calculation basis, the highest differences between optimized and recalculated dose were observed. MIP and AIP CT datasets were found to produce the least dose differences, while the risk of over- or underestimating tumor motion is higher for MIP datasets. Also, density overrides can be useful for patients with a high tumor motion range. Overall, both MIP and AIP datasets tend to be superior for accurate treatment planning with regards to moving tumors. Due to the highly patient-specific character of breathing motion, a general recommendation cannot be provided. Our workflow could, after optimizing the techniques for clinical use, help to provide a 4D dose calculation tool in modern TPS, where the effects of tumor motion have not been incorporated enough up to this point.

CONFLICTS OF INTEREST

a)Author to whom correspondence should be addressed. Electronic mail: philipp.freislederer@med.uni-muenchen.de.

REFERENCES

1. Keall PJ, Mageras GS, Balter JM, et al. The management of respiratory motion in radiation oncology report of AAPM Task Group 76. *Med Phys*. 2006;33:3874.
2. Guckenberger M, Andratschke N, Alheit H, et al. Definition of stereotactic body radiotherapy: principles and practice for the treatment of stage I non-small cell lung cancer. *Strahlenther Onkol*. 2014;190:26–33.
3. Berbeco RI, Pope CJ, Jiang SB. Measurement of the interplay effect in lung IMRT treatment using EDR2 films. *J Appl Clin Med Phys*. 2006;7:33–42.
4. Bortfeld T Jiang SB and Rietzel E. Effects of motion on the total dose distribution. *Semin Radiat Oncol*. 2004;14:41–51.
5. Bortfeld T, Jokivarsi K, Goitein M, Kung J, Jiang SB. Effects of intrafraction motion on IMRT dose delivery: statistical analysis and simulation. *Phys Med Biol*. 2002;47:2203–2220.
6. Court LE, Wagar M, Ionascu D, Berbeco R, Chin L. Management of the interplay effect when using dynamic MLC sequences to treat moving targets. *Med Phys*. 2008;35:1926–1931.
7. Hubley E, Pierce G. The influence of plan modulation on the interplay effect in VMAT liver SBRT treatments. *Phys Med*. 2017;40:115–121.
8. Ford EC, Mageras GS, Yorke E, Ling CC. Respiration-correlated spiral CT: a method of measuring respiratory-induced anatomic motion for radiation treatment planning. *Med Phys*. 2003;30:88–97.
9. Keall PJ, Starkschall G, Shukla H, et al. Acquiring 4D thoracic CT scans using a multislice helical method. *Phys Med Biol*. 2004;49:2053–2067.
10. Low DA, Nystrom M, Kalinin E, et al. A method for the reconstruction of four-dimensional synchronized CT scans acquired during free breathing. *Med Phys*. 2003;30:1254–1263.
11. Mageras GS, Pevsner A, Yorke ED, et al. Measurement of lung tumor motion using respiration-correlated CT. *Int J Radiat Oncol Biol Phys*. 2004;60:933–941.
12. ICRU. Prescribing, Recording and Reporting Photon Beam Therapy (Supplement to ICRU Report 50): ICRU Report 62, International Commission on Radiation Units and Measurements; 1999.
13. Underberg RWM, Lagerwaard FJ, Slotman BJ, Cuijpers JP, Senan S. Use of maximum intensity projections (MIP) for target volume generation in 4DCT scans for lung cancer. *Int J Radiat Oncol Biol Phys*. 2005;63:253–260.
14. Sikora M, Muzik J, Söhn M, Weinmann M, Alber M. Monte Carlo vs. pencil beam based optimization of stereotactic lung IMRT. *Radiat Oncol*. 2009;4:1–13.
15. Tian Y, Wang Z, Ge H, et al. Dosimetric comparison of treatment plans based on free breathing, maximum, and average intensity projection CTs for lung cancer SBRT. *Med Phys*. 2012;2754:2754–2760.
16. Huang L, Park K, Boike T, et al. A study on the dosimetric accuracy of treatment planning for stereotactic body radiation therapy of lung cancer using average and maximum intensity projection images. *Radiother Oncol*. 2010;96:48–54.
17. Han K, Basran PS, Cheung P. Comparison of helical and average computed tomography for stereotactic body radiation treatment planning and normal tissue contouring in lung cancer. *Clin Oncol*. 2010;22:862–867.
18. Wiant D, Vanderstraeten C, Maurer J, Pursley J, Terrell J, Sintay BJ. On the validity of density overrides for VMAT lung SBRT planning. *Med Phys*. 2014;41:081707.
19. Flampouri S, Jiang SB, Sharp GC, Wolfgang J, Patel AA, Choi NC. Estimation of the delivered patient dose in lung IMRT treatment based on deformable registration of 4D-CT data and Monte Carlo simulations. *Phys Med Biol*. 2006;51:2763–2779.
20. Huang T-C, Liang J-A, Dilling T, Wu T-H, Zhang G. Four-dimensional dosimetry validation and study in lung radiotherapy using deformable image registration and Monte Carlo techniques. *Radiat Oncol*. 2010;5:45.
21. Rosu M, Chetty IJ, Balter JM, Kessler ML, McShan DL, Ten Haken RK. Dose reconstruction in deforming lung anatomy: dose grid size effects and clinical implications. *Med Phys*. 2005;32:2487–2495.
22. Zhong H, Siebers JV. Monte Carlo dose mapping on deforming anatomy. *Phys Med Biol*. 2009;54:5815–5830.
23. Heath E, Seuntjens J. A direct voxel tracking method for four-dimensional Monte Carlo dose calculations in deforming anatomy. *Med Phys*. 2006;33:434–445.
24. Heath E, Tessier F, Kawrakow I. Investigation of voxel warping and energy mapping approaches for fast 4D Monte Carlo dose calculations in deformed geometries using VMC++. *Phys Med Biol*. 2011;56:5187–5202.
25. Rosu M, Balter JM, Chetty IJ, et al. How extensive of a 4D dataset is needed to estimate cumulative dose distribution plan evaluation metrics in conformal lung therapy? *Med Phys*. 2007;34:233–245.
26. Rosu M, Hugo G. Advances in 4D radiation therapy for managing respiration: part II - 4D treatment planning. *Z Med Phys*. 2012;22:272–280.
27. Jensen MD, Abdellatif A, Chen J, Wong E. Study of the IMRT interplay effect using a 4DCT Monte Carlo dose calculation. *Phys Med Biol*. 2012;57:N89–N99.
28. Heinz C, Reiner M, Belka C, Walter F, Söhn M. Technical evaluation of different respiratory monitoring systems used for 4D CT acquisition under free breathing. *J Appl Clin Med Phys*. 2015;16:4917.

29. Freislederer P, Heinz C, von Zimmermann H, et al. Clinical workflow optimization to improve 4DCT reconstruction for Toshiba Aquilion CT scanners, Zeitschrift für Medizinische Physik; 2018.

30. Alber M, Birkner M, Laub W, Nüsslin F. Hyperion-An integrated IMRT planning tool. The Use of Computers in Radiation Therapy; 2000:46–48.

31. Alber M. A Concept for the Optimization of Radiotherapy, PhD thesis. Tübingen: Fakultät für Physik der Eberhard-Karls-Universität zu Tübingen; 2000.

32. Fippel M. Fast Monte Carlo dose calculation for photon beams based on the VMC electron algorithm. *Med Phys*. 2014;1466:1466–1475.

33. Sikora M, Dohm O, Alber M. A virtual photon source model of an Elekta linear accelerator with integrated mini MLC for Monte Carlo based IMRT dose calculation. *Phys Med Biol*. 2007;52:4449–4463.

34. Sikora M, Alber M. A virtual source model of electron contamination of a therapeutic photon beam. *Phys Med Biol*. 2009;54:7329–7344.

35. Sikora M, Alber M, Virtual source modelling of photon beams for Monte Carlo based radiation therapy treatment planning. *Radiother Oncol*. 2012;103:S186–S187.

36. Shackleford J, Kandasamy N, Sharp G. On developing B-spline registration algorithms for multi-core processors. *Phys Med Biol*. 2010;55:6329–6351.

37. Sharp GC, Li R, Wolfgang J, et al. Plastimatch-an open source software suite for radiotherapy image processing. In: *Proceedings of the XVIth International Conference on the use of Computers in Radiotherapy (ICCR), Amsterdam, Netherlands*; 2010.

38. Software Development for Integrated Diagnostics and Therapy (SIDT). German Cancer Research Center (DKFZ), Heidelberg, Germany, RTToolboxhttps://github.com/MIC-DKFZ/RTTBAccessed: 2019-01-22.

39. Zhang L, Hub M, Mang S, et al. Software for quantitative analysis of radiotherapy: overview, requirement analysis and design solutions. *Comput Methods Programs Biomed*. 2013;110:528–537.

40. Von Münchow A, Straub K, Hofmaier J, et al. EP-1635: framework for the evaluation of interplay effects between respiratory motion and dose application. *Radiother Oncol*. 2017;123:S886–S887.

41. ICRU. Prescribing, Recording, and Reporting Photon-Beam Intensity-Modulated Radiation Therapy (IMRT): ICRU Report 83. International Commission on Radiation Units and Measurements; 2010.

42. Guckenberger M, Wilbert J, Krieger T. Four-dimensional treatment planning for stereotactic body radiotherapy. *Int J Radiat Oncol Biol Phys*. 2007;69:276–285.

43. Rao M, Wu J, Cao D, et al. Dosimetric impact of breathing motion in lung stereotactic body radiotherapy treatment using image-modulated radiotherapy and volumetric modulated arc therapy. *Int J Radiat Oncol Biol Phys*. 2012;83:e251–e256.

44. Seppenwoolde Y, Shirato H, Kitamura K, et al. Precise and real-time measurement of 3D tumor motion in lung due to breathing and heart-beat, measured during radiotherapy. *Int J Radiat Oncol*. 2002;53:822–834.

45. Shirato H, Seppenwoolde Y, Kitamura K, Onimura R, Shimizu S. Intrafractional tumor motion: lung and liver. *Semin Radiat Oncol*. 2004;14:10–18.

46. Cho B, Poulsen PR, Keall PJ. Real-time tumor tracking using sequential kV imaging combined with respiratory monitoring: a general framework applicable to commonly used IGRT systems. *Phys Med Biol*. 2010;55:3299–3316.

47. Poulsen PR, Cho B, Keall PJ. A method to estimate mean position, motion magnitude, motion correlation, and trajectory of a tumor from cone-beam CT projections for image-guided radiotherapy. *Int J Radiat Oncol Biol Phys*. 2008;72:1587–1596.

48. Cai W, Dhou S, Cifter F, et al. 4D cone beam CT-based dose assessment for SBRT lung cancer treatment. *Phys Med Biol*. 2015;61:554-568.

49. Ehrbar S, Lang S, Stieb S, et al. Three-dimensional versus four-dimensional dose calculation for volumetric modulated arc therapy of hypofractionated treatments. *Z Med Phys*. 2016;26:45–53.

50. Valdes G, Lee C, Tenn S, et al. The relative accuracy of 4D dose accumulation for lung radiotherapy using rigid dose projection versus dose recalculation on every breathing phase. *Med Phys*. 2017;44:1120–1127.

51. Gauer T, Sothmann T, Blanck O, Petersen C, Werner R. Under-reported dosimetry errors due to interplay effects during VMAT dose delivery in extreme hypofractionated stereotactic radiotherapy. *Strahlenther Onkol*. 2018;194:570–579.

52. Siebers JV, Zhong H. An energy transfer method for 4D Monte Carlo dose calculation. *Med Phys*. 2008;35:4096–4105.

Chapter 8

Paper 3: Characteristics of Gated Treatment Using an Optical Surface Imaging and Gating System on an Elekta Linac

Publication: **Characteristics of gated treatment using an optical surface imaging and gating system on an Elekta linac** [1]

RADIATION ONCOLOGY

RESEARCH   **Open Access**

Characteristics of gated treatment using an optical surface imaging and gating system on an Elekta linac

Philipp Freislederer[*], Michael Reiner, Winfried Hoischen, Anton Quanz, Christian Heinz, Franziska Walter, Claus Belka and Matthias Soehn

Abstract

Background: Knowing the technical characteristics of gated radiotherapy equipment is crucial for ensuring precise and accurate treatment when using techniques such as Deep-Inspiration Breath-Hold and gating under free breathing. With one of the first installations of the novel surface imaging system Catalyst™ (C-RAD AB, Sweden) in connection with an Elekta Synergy linear accelerator (Elekta AB, Sweden) via the Elekta Response Interface, characteristics like dose delivery accuracy and time delay were investigated prior to clinical implementation of gated treatments in our institution.

Methods: In this study a moving phantom was used to simulate respiratory motion which was registered by the Catalyst™ system. The gating level was set manually. Within this gating window a trigger signal is automatically sent to the linac initiating treatment delivery. Dose measurements of gated linac treatment beams with different gating levels were recorded with a static 2D-Diode Array (MapCheck2, Sun Nuclear Co., USA) and compared to ungated reference measurements for different field sizes. In addition, the time delay of gated treatment beams was measured using radiographic film.

Results: The difference in dose delivery between gated and ungated treatment decreases with the size of the chosen gating level. For clinically relevant gating levels of about 30%, the differences in dose delivery accuracy remain below 1%. In comparison with other system configurations in literature, the beam-on time delay shows a large deviation of 851 ms ± 100 ms.

Conclusions: When performing gated treatment, especially for free-breathing gating, factors as time delay and dose delivery have to be evaluated regularly in terms of a quality assurance process. Once these parameters are known they can be accounted and compensated for, e.g. by adjusting the pre-selected gating level or the internal target volume margins and by using prediction algorithms for breathing curves. The usage of prediction algorithms becomes inevitable with the high beam-on time delay which is reported here.

Keywords: Respiratory gating, Catalyst, Latency, Dosimetry

Background

Respiratory motion is still one of the major sources for uncertainties in thoracic and abdominal treatment sites in radiation therapy. The accuracy of dose delivery can be increased by respiratory-adapted gating or breathing control [1]. Accounting for intrafraction motion solely by increasing the treatment margins will increase the volume of normal tissue being irradiated with high doses

[2]. Therefore techniques to minimize treatment margins are highly desirable. With the introduction of gated treatments, in which the beam is only activated during specific motion phases (the so-called gating window), [3,4] the increased organ-at-risk (OAR) dose can potentially be reduced to a minimum. Gated treatment has the potential to reduce lung dose for the radiotherapy of thoracic esophageal carcinoma using Deep-Inspiration Breath-Hold (DIBH) techniques [5] and it is considered reliable and effective for patients with high tumor movements in stereotactic body radiotherapy (SBRT) [6].

* Correspondence: Philipp.Freislederer@med.uni-muenchen.de
Department of Radiation Oncology, LMU University Hospital, D-81377 Munich, Germany

In order to ensure precise and accurate treatment several gating characteristics, including dose delivery accuracy, overall latency, and temporal accuracy of the applied system have to be known in advance [7]. Gating is initiated with different respiratory monitoring systems at the moment and various studies have been performed in order to assess the differences between them [8-11]. Several others additionally investigated the question whether or not a linac is able to being gated, [3] or the linac's performance under gated treatment [12-14].

So far the novel surface imaging system Catalyst™ (C-RAD AB, Uppsala, Sweden) in connection with an Elekta Synergy linear accelerator (linac) with Agility Head (Elekta AB, Stockholm, Sweden) and connectivity between those two systems via the Response™ gating interface (Elekta AB, Stockholm, Sweden) has only been examined by calculating theoretical time delays for this system configuration [15]. Dose delivery and time delay have already been measured for other vendors. However, the characteristics of this specific system setup are not known yet. Technically, the gated delivery is being performed by the Response™ interface, which interrupts the RF source during the beam-off period [16]. Our main focus in this study is therefore not only the time delay of the optical surface scanner for the treatment initiation, but the overall system latency, which includes all parts that could possibly delay beam initiation.

Methods

In this study, the gating signal used for the linac is delivered by a surface imaging system. A Dynamic Thorax Phantom (CIRS Inc., Norfolk, VA, USA) was used to simulate a breathing waveform, which is then measured by the Catalyst™ system. One of the first steps of integrating a system based on optical surface measurements was to extend our movement phantom (Figure 1, left). There was a need to construct a surface which can be detected by the surface scanner and reproduces breathing patterns imitating natural physiology. Thermoplastic mask material was mounted to the vertical motion platform of the phantom to mimic a human thorax and to create a surface visible for the scanner.

After defining a measurement point on the phantom surface, the vertical movement is recorded by the commercially available Catalyst™ software. The gating level, which in contrast to other commercially available monitoring systems is a spatial gating window in a specific millimeter range, is set manually. Whenever the point of measurement is detected within the gating level a trigger signal is sent automatically to the linac, initiating treatment delivery.

Dose measurements

In order to measure possible dose differences induced by gated treatment a 2D-Diode Array (MapCheck2, Sun Nuclear Co., Melbourne, FL, USA) was set up stationary. Ungated dose delivery was defined as reference and the absolute dose of the delivery using several gating levels was compared against this reference dose. The array was placed isocentric in SSD = 100 cm and gating levels were chosen as 50%, 40%, 30%, 20%, and 10% of a modulated sine wave simulated by the moving phantom and a total of 300 monitor units (MU) per measurement were
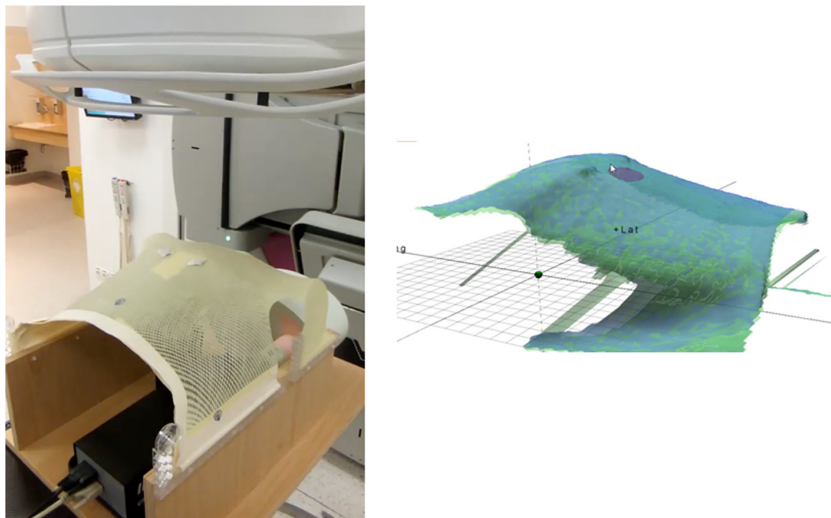
Figure 1 Left: Image of the build-up for the dynamic moving phantom. The surface is reconstructed using mask material. Right: The phantom as it is perceived by the Catalyst™ software.

applied. Measurements were repeated three times for each gating level for two different field sizes (10×10 cm^2 and 20×20 cm^2).

Time delay measurements

An extension to the existing phantom for the application of radiographic films (Gafchromic® EBT, International Specialty Products, Wayne, NJ, USA) was built in order to move the film horizontally through the gated beam (Figure 2). As the film moves through a rectangular field with 2 cm × 2 cm field size with 6 cm peak-to-peak amplitude (sinusoidal motion trajectory), blackening of the film due to irradiation is expected in a 2 cm by 5 cm rectangle (2 cm in width and height due to the field size and an additional 3 cm in height due to the gating window of 50% of the film movement) in an ideal case of no time delay in the overall system. The gating level was set to 50% (see Figure 3) for sinusoidal film movements, as at this level the film is moving with minimal acceleration and constant velocity. With a blackening of the film exceeding the ideal ("no time delay") blackening with a certain length (ΔL) for beam off time delay ($\Delta t_{BEAM-OFF}$) and vice versa for beam on time delay ($\Delta t_{BEAM-ON}$), these two measures can by calculated for the known velocity (v) of the film at this level by $\Delta t = \Delta L \ / \ v$. Figure 3 shows the schematic measurement principle. For a more detailed description of principle of the methods see Smith & Becker [8]. The overall time delay is calculated as a mean value from in total 6 measurements for each beam-on and beam-off time delay. The blackening of the film and consequently the length L was chosen as the part where it has reached its maximum intensity, which is equivalent to the linac reaching its maximum dose rate.
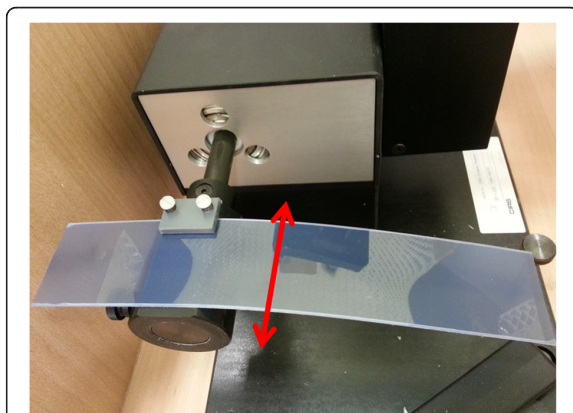
Figure 2 The custom-built extension for the film measurements. Here the extension is placed on the moving rod of the phantom and is moved only in the horizontal direction (red arrow).

Results
Dose measurements

Measured differences in dose delivery between gated and ungated treatment averaged over the whole field size can be seen in Table 1. The total delivered dose decreases with the size of the gating window. With a gating window of only 10% of the breathing cycle in a 10×10 cm^2 field, a dose reduction of $2.15 \pm 0.05\%$ can be observed. In addition, the treatment time for such a gating window as narrow as 10% would be increased by a factor 10 in comparison with ungated treatment. For a larger field size of 20×20 cm^2 a dose reduction of $1.62 \pm 0.05\%$ is measured in contrast to ungated treatment. The absolute number of start-up processes of the linac are naturally dramatically increased when reducing the gating window while maintaining the same amount of MUs. The relationship between dose uncertainties and the number of start-up processes (in our case about 70–90 using a 10% gating window and about 5–7 with a 50% gating window) becomes obvious. For larger (and therefore temporally longer) gating windows which are window sizes with more practical and clinical relevance, the differences in dose delivery accuracy decrease below 1%.

Time delay measurements

We found a value of $\Delta t_{BEAM-OFF} = 215 \pm 69$ ms for the system latency for beam off. For the latency of the beam-on time, however, a value of $\Delta t_{BEAM-ON} = 851 \pm 100$ ms has been measured, which is in contrast to current literature, in which delays smaller than 300 ms have been reported [16]. With the current setup for film measurements, the relatively high standard deviation of 100 ms is explainable through measurement uncertainties due to the resolution of the film, the scanning procedure, and the determination of the starting point of ΔL. It is crucial to define the timepoint (or point on the film respectively), that allows for a clear blackening of the film which occurs when the linac has reached its maximum dose rate. The dose rate varies uncontrollably during each start-up procedure of the linac due to its transient response, which can be seen as a reason for the high time delay.

Discussion

The dose delivery accuracy is comparable to current literature. Evans et al. reported dosimetric differences below 1% for beam-on times higher than 0.5 s with a comparable linac from the same manufacturer [16]. In our case, this beam-on-period would be comparable to a gating window of about 30% where the difference in dose has also been measured below 1%. Even when regarding different linac vendors, dosimetric differences stay constant at around the same level, although only larger gating windows have been evaluated [3]. A direct

Figure 3 Left: Ideal case with the absence of time delay. The blackening of the film on the bottom has the exact length of the desired irradiation. **Right: Real case with system latency**: There is a difference in exposure length between the BEAM-ON signal and the actual exposure of the film ($\Delta L_{BEAM-ON}$) and a difference between the termination signal of the linac and the actual termination of the beam ($\Delta L_{BEAM-OFF}$). Both of these can be measured and with a given velocity, the time delay of the system ($\Delta t_{BEAM-ON}$ and $\Delta t_{BEAM-OFF}$) can therefore be calculated. The schematic blackening of the film on the bottom of each subfigure is a transposition of the film onto the time axis, as ΔL behaves linear proportional to the time delay Δt for given velocities.

comparison of respiratory monitoring systems is not possible, since most of these have been evaluated with Varian linacs, [9,11] or for proton treatment sites [4]. However the data found in literature is not comparable to the findings in this study as Varian uses a different gating approach. For example, the BrainLAB ExacTrac gating system (BrainLAB, Feldkirchen, Germany) in combination with the Varian real-time position management (RPM) gating system (Varian Medical Systems, Palo Alto, CA, USA) were found to have a tracking time delay for the monitoring system only of 200 ± 30 ms and 90 ± 10 ms time delay for beam-on and beam-off times respectively, but there is no mention about the start-up process of the linac afterwards and the subsequent dose delivery to the patient [10].

The method for measuring the system latency has been adapted from Smith & Becker [8]. This particular method proves to be efficient and accurate enough in order to measure the overall time delay. Another method has recently been proposed by Cui et al., [15]

Table 1 Results of the dose measurements for two different field sizes: for both field sizes, there is a decrease in dose relative to ungated treatment when reducing the gating level and therefore increasing the number of start-up processes and delivery time

Gating level	Relative dose (10 x 10 cm^2 field)	Relative dose (20 x 20 cm^2 field)
50%	99.41 ± 0.07%	99.59 ± 0.05%
40%	99.43 ± 0.04%	99.53 ± 0.04%
30%	99.45 ± 0.52%	99.46 ± 0.04%
20%	98.81 ± 0.05%	99.09 ± 0.05%
10%	97.85 ± 0.04%	98.28 ± 0.05%

which, however, does not measure the time delay for each start-up process, does not incorporate the beam-off delay, and the variable dose rate cannot be distinguished in their measurements. In our measurement setup, the time when dose rate variations occur during each start-up process are not considered as beam-on. However the investigators propose options for the optimization of this issue by changing certain parameters of the linac, such as the gun hold-on time (GHT), which is by default at a level of 1.38 s. Increasing this parameter causes the electron gun to stay in an active state rather than switching to standby mode. Once the electron gun reaches this standby mode, it consequently takes longer to be in a stabilized active mode again [15]. This is an interesting point which is to be determined in the future at our site, as also further dosimetric measurements have to be performed. However, increasing the GHT could result in a lower life time of the electron gun and is a setup which has to be measured in a different way. Up to this point only DIBH techniques are implemented at our site, hence the lower GHT is to be considered as the regular system setup.

Besides others, two main effects contribute to the overall system latency, composed by the time delay of the surrogate system (in our case the optical surface scanner) and the time delay of the linac itself. The rather high beam-on time delay of about 850 ms reported here is expected to have its source primarily in the time delay of the linac. According to Lund University [priv. comm.], the mean time delay of the surrogate alone has been measured with about 162 ms for beam-on time and 262 ms for beam-off time using a pneumatic piston in order to generate the breathing pattern. They have measured the time between the output of a trigger signal

and the change in piston position digitally, which could not be performed in our site, but would be a valid way of determining the latency of the surrogate system alone. The beam-off delay of 262 ms for the surrogate system alone is higher than the beam-off delay for the whole treatment chain measured here as we were able to perform our measurements with a newer software version of the surrogate system.

The difference in dose and the time delay for beam-on are due to the fact, that every start-up process of the linac is accompanied by a particular uncertainty because of the linac's transient response. The choice of the duty cycle is crucial: With a decrease in dose of about 2% at the 10% duty cycle and an increased treatment time, awareness is needed when deciding on how far margins should be reduced through gated treatment: There will always be a trade-off between choosing a smaller gating window to reduce margins as far as possible, which reduces residual geometric errors against having this smaller gating window enhance possible dosimetric errors.

Predictive algorithms for respiratory motion implemented in the software of the optical surface scanner could potentially compensate for errors caused by time delays. Up to this point, such algorithms can predict respiratory motion up to 1000 ms [17]. Of course, the quality of these prediction methods is still limited up to a certain extent and larger time delays, as they have been measured here, will also be harder to compensate for, even with a prediction of respiratory motion. A detailed overview of different prediction models and approaches can be found in [18]. As interfractionally both the tumor position and the gating window can change throughout the course of the entire treatment, [19] a periodical update for these will also be required.

Once parameters like time delay and dose distribution are known, they have to be accounted for and compensated by for example adjusting the pre-selected gating level or the internal target volume (or also the clinical target volume, CTV) margins.

Conclusions

When performing gated treatments, especially free-breathing gating, it is crucial that factors such as time delay and dose delivery accuracy have to be determined in advance. In addition regularly QA-measurements as proposed by the AAPM Task Group 76 [2] need to be performed in order to assure stability over time. Our data also indicates the need for the usage of predictive algorithms describing the breathing curves whenever the curves are finally used for gated treatments.

The examined system setup can and is being used for techniques such as DIBH, where a high time delay of about 850 ms is automatically compensated up to a certain extend due to longer gating cycles with less start-up processes of the linac. When it comes to free-breathing gating, certainly some parameter changes (such as the GHT) in the linac and the proposed prediction methods are essential.

Authors' contributions
PF designed the study, acquired the data, built the phantom extension and the extension of the film measurements, analyzed and interpreted the data, and drafted the manuscript. MR helped design the study, has been involved in drafting the manuscript and in revision. WH built the phantom extension and the extension for film measurements and helped with the implementation of the film measurements. AQ built the phantom extension and the extension for film measurements. CH has been involved in drafting the manuscript, interpretation of the data and in revision. FW has been involved in drafting the manuscript and in revision. CB has been involved in drafting the manuscript and in revision. MS has been involved in drafting the manuscript, design of the study, interpretation and analysis of the data and in revision. All authors read and approved the final manuscript.

References
1. Wang W, Li J B, Hu HG, Li FX, Xu M, Sun T, et al. Correlation between target motion and the dosimetric variance of breast and organ at risk during whole breast radiotherapy using 4DCT. Radiat Oncol. 2013;8:111.
2. Keall PJ, Mageras GS, Balter JM, Emery RS, Forster KM, Jiang SB, et al. The management of respiratory motion in radiation oncology report of AAPM Task Group 76. Med Phys. 2006;33:3874.
3. Kubo HD, Hill BC. Respiration gated radiotherapy treatment: a technical study. Phys Med Biol. 1996;41:83–91.
4. Minohara S, Kanai T, Endo M. Respiratory gated irradiation system for heavy-ion radiotherapy. Int J Radiat Oncol Biol Phys. 2000;47:1097–103.
5. Gong G, Wang R, Guo Y, Zhai D, Liu T, Lu J, et al. Reduced lung dose during radiotherapy for thoracic esophageal carcinoma: VMAT combined with active breathing control for moderate DIBH. Radiat Oncol. 2013;8:291.
6. Inoue T, Katoh N, Onimaru R, Shimizu S, Tsuchiya K, Suzuki R, et al. Stereotactic body radiotherapy using gated radiotherapy with real-time tumor-tracking for stage I non-small cell lung cancer. Radiat Oncol. 2013;8:69.
7. Klein EE, Hanley J, Bayouth J, Yin F-F, Simon W, Dresser S, et al. Task Group 142 report: quality assurance of medical accelerators. Med Phys. 2009;36:4197.
8. Smith WL, Becker N. Time delays and margins in gated radiotherapy. J Appl Clin Med Phys. 2009;10:140–54.
9. Jin JJ-Y, Yin FF-F. Time delay measurement for linac based treatment delivery in synchronized respiratory gating radiotherapy. Med Phys. 2005;32:1293.
10. Chang Z, Liu T, Cai J, Chen Q, Wang Z, Yin F-F. Evaluation of integrated respiratory gating systems on a Novalis Tx system. J Appl Clin Med Phys. 2011;12:3495.
11. Smith RL, Lechleiter K, Malinowski K, Shepard DM, Housley DJ, Afghan M, et al. Evaluation of linear accelerator gating with real-time electromagnetic tracking. Int J Radiat Oncol Biol Phys. 2009;74:920–7.
12. Kriminski S, Li AN, Solberg TD. Dosimetric characteristics of a new linear accelerator under gated operation. J Appl Clin Med Phys. 2006;7:65–76.
13. Li XA, Stepaniak C, Gore E. Technical and dosimetric aspects of respiratory gating using a pressure-sensor motion monitoring system. Med Phys. 2006;33:145.
14. Kubo HD, Wang L. Compatibility of Varian 2100C gated operations with enhanced dynamic wedge and IMRT dose delivery. Med Phys. 2000;27:1732.
15. Cui G, Housley DJ, Chen F, Mehta VK, Shepard DM. Delivery efficiency of an Elekta linac under gated operation. J Appl Clin Med Phys. 2014;15:2–11.
16. Evans PM, Symonds-Tayler JRN, Colgan R, Hugo D, Letts N, Sandin C, et al. Gating characteristics of an Elekta radiotherapy treatment unit measured with three types of detector. Phys Med Biol. 2010;55:N201–10.

17. Riaz N, Shanker P, Wiersma R, Gudmundsson O, Mao W, Widrow B, et al.
     Predicting respiratory tumor motion with multi-dimensional adaptive filters
     and support vector regression. Phys Med Biol. 2009;54:5735–48.
18. Lee SJ, Motai Y. Prediction and classification of respiratory motion, vol. 525.
     Berlin, Heidelberg: Springer; 2014 [Studies in Computational Intelligence].
19. Wang JZ, Bin LJ, Wang W, Qi HP, Ma ZF, Zhang YJ, et al. Detection of
     interfraction displacement and volume variance during radiotherapy of
     primary thoracic esophageal cancer based on repeated four-dimensional CT
     scans. Radiat Oncol. 2013;8:224.

Chapter 9

Conclusion

As SBRT of lung tumors suffers from uncertainties due to the patient-specific respiratory breathing motion, every step in the "chain of radiotherapy" has to be performed with special attention for precise and accurate treatment. In this thesis, three specific optimization strategies for improvement of SBRT have been discussed: Investigation of different 4DCT reconstruction methods for reliable tumor delineation during treatment planning, 4D Monte Carlo dose calculation on different CT datasets for optimization of the SBRT treatment planning process, and validation of respiratory gating in a clinical setup.

9.1   4DCT Reconstruction

Treatment planning for lung SBRT requires accurate motion compensation during the course of the treatment planning process. In the presence of artefacts induced by the 4DCT reconstruction method, errors in the subsequent delineation process can lead to substantial dose deviations. As the clinical workflow prior to the work of this thesis using cycle-based sorting (CBS) without maximum inspiration detection (and therefore no clear starting point for the individual breathing cycles) for 4DCT acquisition and reconstruction could over- or underestimate the full tumor motion range, two additional reconstruction methods have been implemented and optimized. An improved version of the CBS with correct maximum inspiration detection and additionally a novel local amplitude-based sorting (LAS) algorithm have been implemented. Both binning algorithms proved capable to reduce the effect of tumor mis-representation compared to the previously used CBS approach in a patient and a phantom study. But as the LAS method was impractical for clinical use due to restrictions from the manufacturers and various manual intermediate steps, the improved CBS method has been implemented clinically. This approach with accurate maximum inspiration detection is used in the Department of Radiation Oncology of the LMU University hospital clinically ever since the first implementation, as it requires minimal extra workload while offering improved 4DCT image quality.

9.2   Four-dimensional Treatment Planning

A 4D Monte Carlo dose recalculation workflow using the LINAC's log file and the actual patient breathing has been implemented in a research platform. The question on which CT should be used as a basis for dose calculation could not been finally answered due to the limited patient number, but one can conclude that the patient-specific respiratory breathing character remains a considerable source of uncertainty in the SBRT treatment planning process, if not accounted for properly. In addition, dose calculations merely on 3D CT datasets were found to yield the highest differences between the planned and the 4D recalculated dose. The findings of this study emphasize the need for a 4D Monte Carlo dose calculation tool, which incorporates the effects of tumor motion (which has not been implemented so far in modern TPS).

9.3   Respiratory Gating

The capabilities and characteristics of a medical LINAC for respiratory gating have to be determined before clinical implementation. Once certain parameters, such as beam-on and beam-off time delay and dose delivery accuracy are known, they have to be accounted for and compensated. The compensation can either be performed by increasing the PTV margins, which would contradict the whole idea of respiratory gating, or with the adjustment of the gating window, which is not a trivial task in the presence of non-stationary intrafractional motion. A trade-off between a decrease in gating window size to reduce margins and therefore residual geometric errors and the possibility of increased dosimetrical errors due to smaller gating windows remains a major challenge. In the setup used at the Department of Radiation Oncology of the LMU University hospital, dose delivery accuracy was found to be in the same range for gated and non-gated treatments, while a substantial time delay has been measured. This emphasizes the need of predictive algorithms for respiratory motion to compensate for the LINAC time delay. In the absence of these algorithms for clinical use, respiratory gating can only be performed where the time delay is not of importance (for example using the DIBH technique with stable breath-hold conditions). With regard to the measured LINAC characteristics, gated treatment based on the patient's duty cycle should only be performed, if a predictive motion model, which is able to provide a periodical update of tumor position and gating window to account for both intra- and interfractional respiratory motion uncertainties, is present.

9.4   Final Remarks

The management of the highly patient-specific respiratory motion in lung SBRT will remain a research field with many current and future issues to be addressed. The findings of this thesis have contributed substantially to improving the clinical workflow at the Department of Radiation Oncology of the LMU University hospital. Nevertheless, much effort has to be made additionally to enhance the possibilities of lung SBRT. The safe further reduction

of treatment margins for an increased sparing of organs-at-risk (OARs) at equal tumor coverage is one of the main goals in the future of SBRT. 4D treatment planning with 4DCT image acquisition and 4D treatment delivery with real time tumor monitoring and an online respiratory prediction model could serve as the one ideal workflow for lung (and other) SBRT treatment sites. Implementation of such advanced workflows will require a close collaboration between researchers and manufacturers, with constant attention to the end goal of clinical application.

Bibliography

[1] World cancer report 2014. *International Agency for Research on Cancer, WHO*, 2014.

[2] Report 90. *Journal of the International Commission on Radiation Units and Measurements*, 14(1):NP–NP, 10 2016. ISSN 1473-6691. doi: 10.1093/jicru/ndw043.

[3] A. F. Abdelnour, S. A. Nehmeh, T. Pan, J. L. Humm, P. Vernon, H. Schöder, K. E. Rosenzweig, G. S. Mageras, E. Yorke, S. M. Larson, and Y. E. Erdi. Phase and amplitude binning for 4D-CT imaging. *Physics in medicine and biology*, 52(12):3515–3529, 2007. ISSN 00942405. doi: 10.1118/1.2240236.

[4] J. R. Adler Jr, S. D. Chang, M. J. Murphy, J. Doty, P. Geis, and S. L. Hancock. The Cyberknife: a frameless robotic system for radiosurgery. *Stereotactic and functional neurosurgery*, 69(1-4):124–128, 1997.

[5] A. Ahnesjö. Collapsed cone convolution of radiant energy for photon dose calculation in heterogeneous media. *Medical physics*, 16(4):577–592, 1989.

[6] A. Ahnesjö and M. M. Aspradakis. Dose calculations for external photon beams in radiotherapy. *Physics in Medicine & Biology*, 44(11):R99, 1999.

[7] A. Ahnesjö, P. Andreo, and A. Brahme. Calculation and application of point spread functions for treatment planning with high energy photon beams. *Acta Oncologica*, 26(1):49–56, 1987.

[8] C. Bert, K. G. Metheany, K. Doppke, and G. T. Y. Chen. A phantom evaluation of a stereo-vision surface imaging system for radiotherapy patient setup. *Medical Physics*, 32(9):2753–2762, 2005. doi: 10.1118/1.1984263.

[9] M. Brada, A. Pope, and M. Baumann. SABR in NSCLC – The beginning of the end or the end of the beginning? *Radiotherapy and Oncology*, 114(2):135–137, feb 2015. ISSN 01678140. doi: 10.1016/j.radonc.2015.01.012.

[10] L. W. Brady, H. Heilmann, and M. Molls. *New technologies in radiation oncology.* Springer, 2006.

[11] F. Bray, J. Ferlay, I. Soerjomataram, R. L. Siegel, L. A. Torre, and A. Jemal. Global cancer statistics 2018: GLOBOCAN estimates of incidence and mortality worldwide for 36 cancers in 185 countries. *CA: A Cancer Journal for Clinicians*, 68(6):394–424, 2018. doi: 10.3322/caac.21492.

[12] G. Carl, D. Reitz, S. Schönecker, M. Pazos, P. Freislederer, M. Reiner, F. Alongi, M. Niyazi, U. Ganswindt, C. Belka, et al. Optical Surface Scanning for Patient Positioning in Radiation Therapy: A Prospective Analysis of 1902 Fractions. *Technology in cancer research & treatment*, 17:1533033818806002, 2018.

[13] S. Corradini, H. Ballhausen, H. Weingandt, P. Freislederer, S. Schönecker, M. Niyazi, C. Simonetto, M. Eidemüller, U. Ganswindt, and C. Belka. Left-sided breast cancer and risks of secondary lung cancer and ischemic heart disease: Effects of modern radiotherapy techniques. *Strahlentherapie und Onkologie*, 194(3), 2018. ISSN 1439099X. doi: 10.1007/s00066-017-1213-y.

[14] W. R. Crum, T. Hartkens, and D. Hill. Non-rigid image registration: theory and practice. *The British journal of radiology*, 77(suppl_2):S140–S153, 2004.

[15] V. Despeignes. Observation concernant un cas de cancer de l'estomac traite par les rayons Rontgen. *Lyon méd.*, 82:428–430, 1896.

[16] Elekta. Elekta Agility ᵀᴹ -Intelligent beam shaping. URL `https://www.elekta.com/dam/jcr:06a48d0e-0971-426e-b804-c03b06c4e839/Agility%E2%84%A2%20brochure%20_Intelligent%20beam%20shaping_.pdf`.

[17] Elekta. Versa HDᵀᴹ - Ultimate power and versatility, 2017. URL `https://www.elekta.com/dam/jcr:14cae385-9b40-4f9b-a805-79a0ecff249e/LPCIYE170601_VHD_FLG_A4ls_f_revised_7.19.17.pdf`.

[18] E. C. Ford, G. S. Mageras, E. Yorke, and C. C. Ling. Respiration-correlated spiral CT: A method of measuring respiratory-induced anatomic motion for radiation treatment planning. *Medical Physics*, 30(1):88, 2003. ISSN 00942405. doi: 10.1118/1.1531177.

[19] C. K. Glide-Hurst, G. D. Hugo, J. Liang, and D. Yan. A simplified method of four-dimensional dose accumulation using the mean patient density representation. *Medical physics*, 35(12):5269–5277, 2008.

[20] D. Greene and P. C. Williams. *Linear accelerators for radiation therapy*. CRC Press, 1997.

[21] M. Guckenberger. Image-guided Radiotherapy Based on Kilovoltage Cone-beam Computed Tomography–A Review of Technology and Clinical Outcome. *Eur Oncol Haematol*, 72(2):121e124, 2011.

[22] M. Guckenberger, M. Weininger, J. Wilbert, A. Richter, K. Baier, T. Krieger, B. Polat, and M. Flentje. Influence of retrospective sorting on image quality in respiratory correlated computed tomography. *Radiotherapy and oncology : journal of the European Society for Therapeutic Radiology and Oncology*, 85(2):223–31, Nov. 2007. ISSN 0167-8140. doi: 10.1016/j.radonc.2007.08.002.

[23] M. Guckenberger, N. Andratschke, H. Alheit, R. Holy, C. Moustakis, U. Nestle, and O. Sauer. Definition of stereotactic body radiotherapy: Principles and practice for the treatment of stage I non-small cell lung cancer. *Strahlentherapie und Onkologie*, 190 (1):26–33, 2014. ISSN 01797158. doi: 10.1007/s00066-013-0450-y.

[24] ICRU. ICRU Report 50—Prescribing, Recording and Reporting Photon Beam Therapy. *International Commission on Radiation Units and Measurements*, 1993.

[25] ICRU. Prescribing, Recording and Reporting Photon Beam Therapy (Supplement to ICRU Report 50): ICRU Report 62. *International Commission on Radiation Units and Measurements*, 1999.

[26] D. Jaffray and J. Siewerdsen. Cone-beam computed tomography with a flat-panel imager: initial performance characterization. *Medical physics*, 27(6):1311–1323, 2000.

[27] D. A. Jaffray. Image-guided radiotherapy: from current concept to future perspectives. *Nature Reviews Clinical Oncology*, 9(12):688, 2012.

[28] C. Karzmark, C. S. Nunan, and E. Tanabe. *Medical electron accelerators*. McGraw-Hill, 1993.

[29] P. Keall, V. Kini, S. Vedam, and R. Mohan. Motion adaptive x-ray therapy: a feasibility study. *Physics in Medicine & Biology*, 46(1):1, 2001.

[30] P. J. Keall, G. Starkschall, H. Shukla, K. M. Forster, V. Ortiz, C. W. Stevens, S. S. Vedam, R. George, T. Guerrero, and R. Mohan. Acquiring 4D thoracic CT scans using a multislice helical method. *Physics in medicine and biology*, 49(10):2053–2067, 2004. ISSN 0031-9155. doi: 10.1088/0031-9155/49/10/015.

[31] P. J. Keall, G. S. Mageras, J. M. Balter, R. S. Emery, K. M. Forster, S. B. Jiang, J. M. Kapatoes, D. a. Low, M. J. Murphy, B. R. Murray, C. R. Ramsey, M. B. Van Herk, S. S. Vedam, J. W. Wong, and E. Yorke. The management of respiratory motion in radiation oncology report of AAPM Task Group 76. *Medical Physics*, 33(10):3874, Oct. 2006. ISSN 0094-2405. doi: 10.1118/1.2349696.

[32] F. M. Khan and J. P. Gibbons. *Khan's the physics of radiation therapy*. Lippincott Williams & Wilkins, 2014.

[33] H. Krieger. *Grundlagen der Strahlungsphysik und des Strahlenschutzes*. 2012. ISBN 978-3-8348-1815-7. doi: 10.1007/978-3-8348-2238-3.

[34] H. D. Kubo and B. C. Hill. Respiration gated radiotherapy treatment: a technical study. *Phys Med Biol*, 41, 1996. doi: 10.1088/0031-9155/41/1/007.

[35] H. Li, C. Noel, J. Garcia-Ramirez, D. Low, J. Bradley, C. Robinson, S. Mutic, and P. Parikh. Clinical evaluations of an amplitude-based binning algorithm for 4DCT reconstruction in radiation therapy. *Medical Physics*, 39(2):922, 2012. ISSN 00942405. doi: 10.1118/1.3679015.

[36] D. A. Low, M. Nystrom, E. Kalinin, P. Parikh, J. F. Dempsey, J. D. Bradley, S. Mutic, S. H. Wahab, T. Islam, G. Christensen, D. G. Politte, and B. R. Whiting. A method for the reconstruction of four-dimensional synchronized CT scans acquired during free breathing. *Medical Physics*, 30(6):1254, 2003. ISSN 00942405. doi: 10.1118/1.1576230.

[37] W. Lu, P. J. Parikh, J. P. Hubenschmidt, J. D. Bradley, and D. A. Low. A comparison between amplitude sorting and phase-angle sorting using external respiratory measurement for 4D CT. *Medical Physics*, 33(8):2964–2974, 2006. ISSN 00942405. doi: 10.1118/1.2219772.

[38] C.-M. Ma and J. Li. Dose specification for radiation therapy: dose to water or dose to medium? *Physics in Medicine and Biology*, 56(10):3073–3089, apr 2011. doi: 10.1088/0031-9155/56/10/012.

[39] G. S. Mageras, A. Pevsner, E. D. Yorke, K. E. Rosenzweig, E. C. Ford, A. Hertanto, S. M. Larson, D. M. Lovelock, Y. E. Erdi, S. a. Nehmeh, J. L. Humm, and C. C. Ling. Measurement of lung tumor motion using respiration-correlated CT. *International journal of radiation oncology, biology, physics*, 60(3):933–41, nov 2004. ISSN 0360-3016. doi: 10.1016/j.ijrobp.2004.06.021.

[40] G. S. Mageras, A. Pevsner, E. D. Yorke, K. E. Rosenzweig, E. C. Ford, A. Hertanto, S. M. Larson, D. M. Lovelock, Y. E. Erdi, S. A. Nehmeh, J. L. Humm, and C. C. Ling. Measurement of lung tumor motion using respiration-correlated CT. *International Journal of Radiation Oncology* Biology* Physics*, 60(3):933–941, 2004.

[41] J. R. McClelland, D. J. Hawkes, T. Schaeffter, and a. P. King. Respiratory motion models: a review. *Medical image analysis*, 17(1):19–42, jan 2013. ISSN 1361-8423. doi: 10.1016/j.media.2012.09.005.

[42] S. Minohara, T. Kanai, and M. Endo. Respiratory gated irradiation system for heavy-ion radiotherapy. *Int J Radiat Oncol Biol Phys*, 47, 2000. doi: 10.1016/S0360-3016(00)00524-1.

[43] R. Mohan, C. Chui, and L. Lidofsky. Differential pencil beam dose computation model for photons. *Medical Physics*, 13(1):64–73, 1986.

[44] Y. Negoro, Y. Nagata, T. Aoki, T. Mizowaki, N. Araki, K. Takayama, M. Kokubo, S. Yano, S. Koga, K. Sasai, et al. The effectiveness of an immobilization device in

conformal radiotherapy for lung tumor: reduction of respiratory tumor movement and evaluation of the daily setup accuracy. *International Journal of Radiation Oncology* Biology* Physics*, 50(4):889–898, 2001.

[45] J. Nuyttens, J.-B. Prevost, J. Praag, M. Hoogeman, R. Van Klaveren, P. Levendag, and P. Pattynama. Lung tumor tracking during stereotactic radiotherapy treatment with the CyberKnife: Marker placement and early results. *Acta Oncologica*, 45(7): 961–965, 2006.

[46] B. Ohnesorge, T. Flohr, C. Becker, A. F. Kopp, U. J. Schoepf, U. Baum, A. Knez, K. Klingenbeck-Regn, and M. F. Reiser. Cardiac imaging by means of electrocardiographically gated multisection spiral CT: initial experience. *Radiology*, 217(2): 564–571, 2000.

[47] L. Padilla, H. Kang, M. Washington, Y. Hasan, S. J. Chmura, and H. Al-Hallaq. Assessment of interfractional variation of the breast surface following conventional patient positioning for whole-breast radiotherapy. *Journal of applied clinical medical physics*, 15(5):177–189, 2014.

[48] T. Pan. Comparison of helical and cine acquisitions for 4D-CT imaging with multislice CT. *Medical physics*, 32(2):627–634, 2005. ISSN 00942405. doi: 10.1118/1.1855013.

[49] E. B. Podgorsak and K. Kainz. Radiation Oncology Physics: A Handbook for Teachers and Students. *Medical Physics*, 33(6):1920, 2006. ISSN 00942405. doi: 10.1118/1. 2201870.

[50] J.-B. Prévost, M. S. Hoogeman, J. Praag, B. van der Holt, P. C. Levendag, R. J. van Klaveren, P. Pattynama, J. J. Nuyttens, et al. Stereotactic radiotherapy with real-time tumor tracking for non-small cell lung cancer: clinical outcome. *Radiotherapy and Oncology*, 91(3):296–300, 2009.

[51] D. Reitz, G. Carl, S. Schönecker, M. Pazos, P. Freislederer, M. Niyazi, U. Ganswindt, F. Alongi, M. Reiner, C. Belka, and S. Corradini. Real-time intra-fraction motion management in breast cancer radiotherapy: Analysis of 2028 treatment sessions. *Radiation Oncology*, 13(1):1–9, 2018. ISSN 1748717X. doi: 10.1186/s13014-018-1072-4.

[52] W. Röntgen. Über eine neue Art von Strahlen: vorläufige Mitteilung. *Sitzungsber. Phys. Med. Gesell.*, 1895.

[53] M. Rosu and G. Hugo. Advances in 4D radiation therapy for managing respiration: Part II - 4D treatment planning. *Zeitschrift für Medizinische Physik*, 22(4):272–280, 2012. ISSN 09393889 18764436. doi: 10.1016/j.zemedi.2012.06.011.

[54] F. Salvat and J. M. Fernández-Varea. Overview of physical interaction models for photon and electron transport used in Monte Carlo codes. *Metrologia*, 46(2), 2009. ISSN 16817575. doi: 10.1088/0026-1394/46/2/S08.

[55] W. Schlegel and A. Mahr. 3D Conformal Radiation Therapy: A multimedia introduction to methods and techniques, CD-ROM, 2001.

[56] W. Schlegel, C. P. Karger, and O. Jäkel, editors. *Medizinische Physik*. Springer Berlin Heidelberg, Berlin, Heidelberg, 2018. ISBN 978-3-662-54800-4. doi: 10.1007/978-3-662-54801-1.

[57] U. Schneider, E. Pedroni, and A. Lomax. The calibration of CT Hounsfield units for radiotherapy treatment planning. *Physics in Medicine and Biology*, 41(1):111–124, jan 1996. doi: 10.1088/0031-9155/41/1/009.

[58] S. Schönecker, F. Walter, P. Freislederer, C. Marisch, H. Scheithauer, N. Harbeck, S. Corradini, and C. Belka. Treatment planning and evaluation of gated radiotherapy in left-sided breast cancer patients using the CatalystTM/SentinelTM system for deep inspiration breath-hold (DIBH). *Radiation Oncology*, 11(1):143, 2016. ISSN 1748-717X. doi: 10.1186/s13014-016-0716-5.

[59] S. M. Seltzer. Calculation of Photon Mass Energy-Transfer and Mass Energy-Absorption Coefficients. *Radiation Research*, 136(2):147, 1993. ISSN 00337587. doi: 10.2307/3578607.

[60] Y. Seppenwoolde, H. Shirato, K. Kitamura, S. Shimizu, M. Van Herk, J. V. Lebesque, and K. Miyasaka. Precise and real-time measurement of 3D tumor motion in lung due to breathing and heartbeat, measured during radiotherapy. *International Journal of Radiation Oncology* Biology* Physics*, 53(4):822–834, 2002.

[61] Y. Seppenwoolde, R. I. Berbeco, S. Nishioka, H. Shirato, and B. Heijmen. Accuracy of tumor motion compensation algorithm from a robotic respiratory tracking system: a simulation study. *Medical physics*, 34(7):2774–2784, 2007.

[62] H. Shirato, Y. Seppenwoolde, K. Kitamura, R. Onimura, and S. Shimizu. Intrafractional tumor motion: lung and liver. In *Seminars in radiation oncology*, volume 14, pages 10–18. Elsevier, 2004.

[63] J. C. Stroom and B. J. Heijmen. Geometrical uncertainties, radiotherapy planning margins, and the ICRU-62 report. *Radiotherapy and oncology*, 64(1):75–83, 2002.

[64] R. W. M. Underberg, F. J. Lagerwaard, B. J. Slotman, J. P. Cuijpers, and S. Senan. Use of maximum intensity projections (MIP) for target volume generation in 4DCT scans for lung cancer. *International Journal of Radiation Oncology Biology Physics*, 63(1):253–260, 2005. ISSN 03603016. doi: 10.1016/j.ijrobp.2005.05.045.

[65] M. Van Herk. Errors and margins in radiotherapy. In *Seminars in radiation oncology*, volume 14, pages 52–64. Elsevier, 2004.

[66] B. Vanderstraeten, N. Reynaert, L. Paelinck, I. Madani, C. De Wagter, W. De Gersem, W. De Neve, and H. Thierens. Accuracy of patient dose calculation for lung IMRT: A comparison of Monte Carlo, convolution/superposition, and pencil beam computations. *Medical physics*, 33(9):3149–3158, 2006.

[67] S. S. Vedam, P. J. Keall, V. R. Kini, H. Mostafavi, H. P. Shukla, and R. Mohan. Acquiring a four-dimensional computed tomography dataset using an external respiratory signal. *Physics in Medicine and Biology*, 48(1):45–62, dec 2002. doi: 10.1088/0031-9155/48/1/304.

[68] D. Verellen, M. De Ridder, and G. Storme. A (short) history of image-guided radiotherapy. *Radiotherapy and Oncology*, 86(1):4–13, 2008.

[69] W. Wang, J. B. Li, H. G. Hu, F. X. Li, M. Xu, T. Sun, and J. Lu. Correlation between target motion and the dosimetric variance of breast and organ at risk during whole breast radiotherapy using 4DCT. *Radiation oncology*, 8:111, 2013.

[70] T. R. Willoughby, P. A. Kupelian, J. Pouliot, K. Shinohara, M. Aubin, M. Roach III, L. L. Skrumeda, J. M. Balter, D. W. Litzenberg, S. W. Hadley, J. T. Wei, and H. D. Sandler. Target localization and real-time tracking using the Calypso 4D localization system in patients with localized prostate cancer. *International Journal of Radiation Oncology* Biology* Physics*, 65(2):528–534, 2006.

[71] N. M. Wink, C. Panknin, and T. D. Solberg. Phase versus amplitude sorting of 4D-CT data. *Journal of Applied Clinical Medical Physics*, 7(1):77–85, 2006. ISSN 15269914. doi: 10.1120/jacmp.2027.25373.

[72] J. W. Wolthaus, C. Schneider, J.-J. Sonke, M. van Herk, J. S. Belderbos, M. M. Rossi, J. V. Lebesque, and E. M. Damen. Mid-ventilation CT scan construction from four-dimensional respiration-correlated CT scans for radiotherapy planning of lung cancer patients. *International Journal of Radiation Oncology* Biology* Physics*, 65 (5):1560–1571, 2006.

[73] T. C. Zhu and K. K.-H. Wang. *Linear Accelerators (LINAC)*, pages 437–450. Springer Berlin Heidelberg, Berlin, Heidelberg, 2013. ISBN 978-3-540-85516-3. doi: 10.1007/978-3-540-85516-3_37.